University of California
Santa Barbara

Dynamic Nuclear Polarization Methods Development for Achieving High Nuclear Magnetic Resonance Signal Sensitivity

A dissertation submitted in partial satisfaction
of the requirements for the degree

Doctor of Philosophy
in
Chemistry

by

Yuanxin Li

Committee in charge:

Professor Songi Han, Chair
Professor Frederick Dahlquist
Professor Bernard Kirtman
Professor Bradley Chmelka

September 2021

The Dissertation of Yuanxin Li is approved.

Professor Frederick Dahlquist

Professor Bernard Kirtman

Professor Bradley Chmelka

Professor Songi Han, Committee Chair

August 2021

Dynamic Nuclear Polarization Methods Development for Achieving High Nuclear Magnetic Resonance Signal Sensitivity

by

Yuanxin Li

Acknowledgements

PhD is one of the most valuable experiences in my life and I felt so lucky to be able to study at UCSB not only because of the nice weather but also because of all the people I met during this journey. First of all, I would like to thank my advisor, Prof. Songi Han. She is an amazing advisor and has taught me skills that are critical for my future career development, such as critical thinking, effective presentations and communications, project management, time management, etc. In addition to the professional help, she also gave me great emotional supports during my journey of PhD. Without her guidance, I will not be the same person as I am right now.

I would like to thank all my colleagues in the Han Lab for providing such a enjoyable working environment. Especially, I would like to thank Dr. Sheetal Jain (now Prof. Sheetal Jain) and Dr. Asif Equbal, whom I had shared office with for 3-4 years. They offered me enormous help in the fundamental understanding of DNP and NMR theory as well as the advanced experimental applications. We have become good personal friends and I really appreciate all the parties I was invited and the tasty Indian food I tried. I would like to thank Kan Tagami, Dr. Alisa Leavesley, Dr. Ilia Kaminker and Dr. Alicia Lund for the help in the operation of the 7 T static dual pulsed DNP-EPR and the 7 T MAS pulsed DNP spectrometers. I would like to thank Tarnuma Tabassum, Karen Tsay, Dr. Timothy Keller and Dr. Thomas Casey for the help in setting up pulsed EPR experiments under Q-band and X-band fields. I would like to thank Raj Chaklashiya, Dr. Hiroki Takahashi from JEOL RESONANCE Inc., Japan and others from JEOL USA Inc. for the successful installation of the 14.1 T JEOL NMR instrument with a closed-cycle helium MAS system. I would like to thank Dr. Jerry Hu and Jaya Nolt for the help in the operation of the 400 MHz Bruker DNP as well as other solid-state

NMR spectrometers in the UCSB Materials Research Laboratory. I would like to thank Michael Vigers for the help in obtaining high quality TEM images for tau fibrils and Dr. Yann Fichou for the valuable discussions on the tau projects. I would like to thank Dr. Chungta Han for providing isotope labeled Proteorhodopsin proteins for DNP studies. I would like to thank Dr. Till Überrück and Prof. Bernhard Blümich at Aachen University of Technology (RWTH), Germany for hosting my visit and teaching me the instrumentation of NMR-MOUSE during the summer of 2018. In addition, I would like to thank my collaborators Prof. Andrzej Rajca and Prof. Yangping Liu for providing interesting DNP radicals, Prof. Kaustubh R. Mote and Prof. P. K. Madhu for synthesizing isotope labeled tau peptides, Prof. Madhur Srivastava for the collaboration on the DNP denoising projects.

I would like to thank my committee members for the help during my PhD. I would like to thank Prof. Bernard Kirtman for teaching me quantum mechanics and help me understand fundamentals of NMR theory. I would like to thank Prof. Bradley Chmelka for the discussions in the state-of-the-art NMR applications. I would like to thank Prof. Frederick Dahlquist for the help in the protein NMR studies.

Last but not the least, I would like to give my special thanks to my family and friends for all the emotional supports and fun time. Throughout my life, my parents have been teaching me so many life lessons and giving me unconditional supports in all the decisions I made. I would like to thank all my friends who have given me great companions during my PhD (listed no specific order): Marco, Li, Kate, Jiren, Beihang, Lumari, Marcus, Sheng-Ping, Michael, Kavita, Shruti and many others. In the end, I would like to thank my two cats Pingo and Cinnamon for the irreplaceable companionship.

Curriculum Vitæ

Yuanxin Li

Education

09/2016-08/2021	Ph.D., Physical Chemistry, University of California, Santa Barbara (expected).
09/2012-07/2016	B.S., Chemistry, Zhejiang University, Hangzhou, Zhejiang, China

Research Experience

Method Development of Dynamic Nuclear Polarization

Developed new NMR sensitivity enhancement methods based on quantum mechanical simulations and electron/nuclear spin dynamics measurements at variable temperatures (3.3 K to room temperature) under different magnetic fields (0.35 to 14 Tesla).

- Led projects on investigating spin dynamics of systems at variable temperatures using NMR, EPR, DNP and other cutting edge techniques.
- Revealed the physical meaning behind the spin dynamics measurements with quantum mechanical simulations.
- Selected optimum spin systems for signal acquisition considering the temperature requirement, cost, time and instrumentation availability.

Solid-state NMR Application

Performed state-of-the-art NMR experiments for a large range of nuclear spins (^{1}H, ^{13}C, ^{15}N, ^{19}F, ^{29}Si) on commercial Bruker 9.4 T , 11.7 T and 18.8 T solid-state NMR spectrometers under fast sample rotation (4-75 kHz) conditions.

- Revealed the minor -$Si(OH)_3$ species in silica nano-particles
- Conducted multi-dimensional and multi-nuclear solid-state NMR experiments to find the correlation among ^{1}H, ^{13}C and ^{15}N in proteins.
- Carried out multi-quantum experiments for deciphering hetero-nuclear and homo-nuclear correlations.
- Modeled experimental results with quantum mechanical simulations to extract ^{13}C-^{15}N distances with an accuracy of $\pm$ 0.1 $\mathring{A}$.
- Pulse sequence programming and troubleshooting on both topspin (Bruker) and Delta (JEOL).
- Quantified atomic level structural and dynamics information of materials (such as polymers, silica and proteins) at variable temperatures. This includes optimizing sample preparation methods for different materials.

Instrumentation Maintenance & Development

Operated and maintained NMR spectrometers utilizing engineering, trouble-shooting, programming, problem-solving, management and communication skills.

- Operated Bruker AV-III 800, Bruker AV 500 wide bore solid state NMR, equipped with 7 mm, 4 mm, 3.2 mm, 2.5 mm, 1.3 mm MAS probes.
- Installed ECZ600RWB JEOL NMR with Helium circulation system equipped with 3.2 mm DNP probe and 1 mm fast MAS probe in assistance with engineers. This includes hardware and software installation, trouble-shooting, training users, creating operation manuals and lab management.
- Set up variable temperature experiments with FTS chiller on Bruker AV-III 800 and AV 500 solid state as well as the JEOL ECZ600RWB NMR spectrometers.
- Utilized Bruker 400 DNP spectrometer equipped with 3.2 mm DNP MAS probe.
- Maintained the operation of the the home-built 300 MHz dual EPR/DNP spectrometer at cryogenic temperatures. This included trouble-shooting both RF and microwave components, helium circulation systems' upkeep, vendor coordination of liquid nitrogen, helium and other necessities.
- Handled Varian VNMRS 600 MHz, Bruker AV 500 solution state NMR.
- Operated Bruker Elexsys x-band pulse EPR, Q-band EPR and CW EPR spectrometers at variable temperatures from 4 K to room temperature.
- Automated data analysis with user-friendly interfaces, including data-pulling, processing and fitting utilizing python and MATLAB.
- Customized tools and established protocols for preparing different samples, such as proteins, polymers, silica nano-particles and inorganic crystals.

Instrumental development of low field magnetic resonance spectrometer for remote sensing

Constructed a single-sided, low-field, portable DNP-MOUSE (MObile Universal Surface Explorer) which allows remote sensing of many NMR active nuclei in well logging, rubber materials and paints at an affordable price as well as at non-cryogenics temperatures.
Advisor: Bernhard Blümich, RWTH Aachen University, Germany

- Designed the precise geometry of a 0.2 T single-sided NMR-MOUSE using COMSOL Multiphysics software.
- Constructed the NMR-MOUSE with 1.45 T permanent magnets as well as the radio-frequency pick-up coil for the target field.

Publications

1. **Li, Y.**, Chaklashiya, R., Takahashi, H., Kawahara, Y., Tagami, K., and Han, S. (2021) Solid-State MAS NMR at Ultra Low Temperature of Hydrated Bio-solids Doped with DNP Radicals. *J. Magn. Reson.*, Submitted.
2. Equbal, A., Jain, S., **Li, Y.**, Tagami, K., Wang, X., & Han, S. (2021).Role of Electron Spin Dynamics and Coupling Network in Designing Dynamic Nuclear Polarization. *Prog. Nucl. Mag. Res. Sp.*.
3. **Li, Y.**, Equbal, A., and Han, S. (2020). ^{1}H Thermal Mixing Dynamic Nuclear Polarization with BDPA as Polarizing Agents. *J. Phy. Chem. Lett.*, 11(21), 9195-9202.
4. Equbal, A., **Li, Y.**, Tabassum, T., and Han, S. (2020). Crossover from a Solid Effect to Thermal Mixing ^{1}H Dynamic Nuclear Polarization with Trityl-OX063. *J. Phy. Chem. Lett.*,11(9),3718-3723.
5. **Li, Y.**, Equbal, A., Tagami, K., & Han, S. (2019). Electron Spin Density Matching for Cross-Effect Dynamic Nuclear Polarization. *Chem. Comm.*, 55, 7591-7594. (**Selected as the front cover for the Journal of Chemical Communications issue 53**)
6. Equbal, A., **Li, Y.***, Leavesley, A., Huang, S., Rajca, S., Rajca, A., & Han, S. (2018). Truncated Cross Effect Dynamic Nuclear Polarization: An Overhauser Effect Doppelgänger. *J. Phy. Chem. Lett.*, 9(9), 2175-2180.***Co-first author**
7. Schrader, A. M., Monroe, J. I., Sheil, R., Dobbs, H. A., Keller, T. J., **Li, Y.**, ... & Han, S. (2018). Surface Chemical Heterogeneity Modulates Silica Surface Hydration. *Proc. Natl. Acad. Sci*, 115(12), 2890-2895.

Posters and Talks

1. March 2021, Hydrated Bio-solid MAS DNP NMR at Ultra Low Temperature, 62nd Experimental Nuclear Magnetic Resonance Conference, virtual
2. April 2019, Mixed-Radical Matching for Highly Efficient Cross-Effect DNP, 60th Experimental Nuclear Magnetic Resonance Conference, Pacific Grove, USA
3. August 2018, Truncated Cross Effect DNP: An Overhauser Effect Doppelgänger, Invited speaker, Radboud University, Nijmegen, Netherlands

Abstract

Dynamic Nuclear Polarization Methods Development for Achieving High Nuclear Magnetic Resonance Signal Sensitivity

by

Yuanxin Li

Solid-state nuclear magnetic resonance (NMR) is an essential tool for the study of biological solids, catalysts, and other functional materials. However, NMR has intrinsically low signal sensitivity and dynamic nuclear polarization (DNP) is one of the most effective approaches to enhance NMR sensitivity. DNP enhances NMR signal sensitivity through transferring the high polarization of electron spins to nuclear spins using microwave (μw) irradiation as a perturbation via different DNP mechanisms. As current DNP efficiency is still far from the theoretical limit (660 for ^{1}H NMR), a major focus in DNP research is to develop methods that can maximize DNP enhancements at conditions germane to solid-state NMR, at high magnetic fields, with fast magic angle spinning (MAS), and under variable temperatures. There are many aspects involved in DNP methods development, including the DNP mechanisms clarification and improvement, instrumentation development, better samples preparation methods, and new data processing techniques.

DNP mechanisms development is one of the most important aspects in the DNP methods development area. Current diagnostics of DNP mostly rely on the analysis of the nuclear spin dynamics as a function of μw irradiation parameters which provides incomplete (sometimes even misleading) insights into the mechanism diagnosis process. With the help of continuous wave and pulsed electron paramagnetic resonance (EPR) spectrometers at various fields (from 0.35 to 7 Tesla) as well as quantum mechanical simu-

lations, I have developed and standardized a workflow to diagnose DNP mechanisms and improve their efficiencies. Using the developed workflow, I have improved the existing Cross Effect (CE) DNP efficiency significantly by rationally tuning the the EPR spectral density of mixed broad (TEMPO) and narrow (Trityl)-line radicals, suggesting a novel polarizing agent design of one Trityl tethered to at least two TEMPO moieties. With the help of this novel workflow, a new truncated CE DNP mechanisms was discovered that has the apparent features of an Overhauser Effect. This discovery not only expanded the scope of the theoretical understanding of DNP mechanisms but also provided a technique to probe paramagnetic materials with very fast electron spin lattice relaxation rates. Furthermore, I have discovered an unexpected ^{1}H Thermal Mixing (TM) DNP mechanism with narrow line radicals Trityl and BDPA, providing a new direction of future DNP radical design utilizing the TM DNP mechanism.

Instrumentation development is another key aspect in the DNP methods development. In this aspect, being able to operate at ultra low temperature (ULT, $\ll$ 100 K) is one of the major challenges. In collaboration with JEOL RESONANCE Inc., Japan and JEOL USA Inc, we have successfully installed the first commercial 14.1 Tesla NMR spectrometer equipped with a closed-cycle helium ULT-MAS system. To demonstrate the feasibility of doing DNP/NMR at ULT using the newly installed system, I conducted a comprehensive NMR characterization of a hydrated [U-^{13}C]alanine standard sample at variable temperatures (25 – 100 K) and different spinning speeds (1.5 – 100 kHz). I confirmed that the ^{13}C CP-MAS NMR of [U-^{13}C]alanine obtained a large sensitivity gain at ULT resulting from the Boltzmann factor, radio frequency circuitry quality factor improvement and the suppression of its methyl group rotation. I further observed that the addition of organic biradicals widely used for CE DNP significantly shortened the ^{1}H T_1 spin lattice relaxation time at ULT via the two-electron-one-nucleus triple

flip transition, without further broadening the ^{13}C spectral linewidth. My experimental observations suggest that the prospects of DNP/NMR under ULT conditions established with a closed-cycle helium MAS system are bright.

With the DNP mechanisms improvements and instrumentation advancements, I have further applied DNP enhanced NMR to study biological samples as well as inorganic silica nano-particles, where tens to hundreds of DNP enhancements have been achieved in all the tested samples. Preliminary DNP study has already provided unprecedented information of the presence of a minor $–Si(OH)_3$ species in the hydrated natural abundant silica nano-particle materials. However, the applications of DNP in bio-solid materials need more than sensitivity enhancement, where NMR spectral resolution is another critical factor. To eventually apply DNP in bio-solids, better sample preparation methods to obtain homogeneous Tau amyloid protein fibrils and better data processing using wavelet denoising techniques are underdevelopment.

Contents

Chapter 1

Introduction

1.1 Motivation

Solid-state Nuclear Magnetic Resonance (NMR) spectroscopy is a powerful characterization technique with a broad application scope ranging from structural biology, biochemistry, molecular design, and catalysis to materials chemistry. NMR is a non-invasive technique that offers atomically detailed structural and dynamical information of crystalline and non-crystalline materials that may harbor significant disorder and/or heterogeneity. In spite of these merits, the intrinsically low sensitivity remains the bottleneck for expanding the utility of solid-state NMR for the characterization of surfaces and the detection and characterization of minor species, including low natural abundance isotopes or low population species. Dynamic Nuclear Polarization (DNP) is a rapidly evolving tech-

nique that can improve solid-state NMR sensitivity by several orders of magnitude using highly polarized electron spins (e) of a paramagnetic polarizing agent (PA).[1] DNP-NMR has provided unique access to chemical systems that are out of reach for conventional NMR characterization, including time-resolved structural studies of amyloid fibrils in their formation process, determination of the molecular structure of the reaction center in membrane proteins,[2, 3, 4, 5, 6] and multi-dimensional NMR of low-abundant NMR active nuclei such as ^{29}Si and ^{17}O in functional inorganic materials.[7, 8, 9, 10, 11, 12]

However, there are inherent challenges in harnessing the full potential of DNP for solid- state NMR characterization. In particular, bio-molecular NMR cannot fully exploit the benefit of DNP given that the DNP efficiency is lower at high magnetic fields and under fast magic-angle spinning (MAS), both of which are important conditions for achieving high spectral resolution. Moreover, the requirement to use vitrified samples for DNP lowers the NMR spectral resolution, in part because of the properties of the vitrified sample itself, and in part because cryogenic operation $\sim$100 K relies on liquid nitrogen which limits reaching high MAS frequencies. DNP requires ^{1}H rich solvents for the diffusion of the polarization from the electron spins to the target sites. Hence, there are challenges in the utilization of DNP for materials not embedded in, impregnated with, or dissolved in ^{1}H-containing solvents. The characterization of solvent-less materials demands innovation around the current DNP approaches that tend to be optimized for the polarization of abundant NMR active nuclei. In fact, even for archetypal ^{1}H rich systems that offer robust DNP performance, there still remains significant scope for increasing the DNP efficiency towards its theoretical limit.[1]

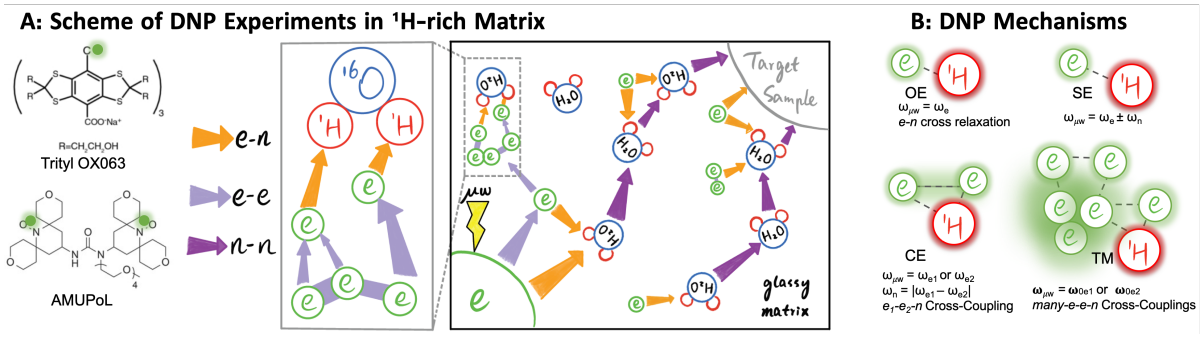

Figure 1.1: **A**: Schematic of polarization pathways for DNP of ^{1}H-rich solvent. The electron spin, ^{1}H of water, ^{16}O of water and target sample are represented as green, red, blue and grey circles, respectively. The *e*-*n* hyperfine couplings, *e*-*e* couplings and *n*-*n* couplings are displayed with differently colored arrows as indicated. **B**: Model system for four general DNP mechanisms: SE (e,n), OE (e,n), CE ($2e$,n) and TM (multi-e,n) with corresponding μw irradiation conditions.

1.2 DNP of a ^{1}H-rich matrix

The most common experimental approach to DNP is the selective saturation of the electron paramagnetic resonance (EPR) of the PA by μw irradiation, resulting in polarization transfer from e to n spins. A scheme of DNP experiments is illustrated in figure 1.1A. Currently, the majority of DNP applications rely on nitroxide- or carbon-based PAs. The structures of the most commonly used PAs are included in figure 1.1A, where the free electrons are marked with green circles. These PAs are dissolved in solvent mixtures such as water-glycerol, water-DMSO or tetrachloroethylene (TCE) that form a glassy matrix upon vitrification and provide a ^{1}H spin-diffusion network. The NMR sample of interest is either dissolved in the PA-containing glass-forming matrix or is impregnated with it. DNP enhancement of NMR of samples impregnated with the PA-containing glass-forming matrix has proven to be a highly beneficial approach for surface characterization of materials, and is popularly referred to as DNP-Surface Enhanced NMR Spectroscopy (DNP-SENS).[12, 13, 14, 15, 16]

The polarization enhancement of the target sites in a glassy matrix relies on three major steps. First, the selective saturation of the EPR signals of PAs induces polarization transfer from the PA to nearby ^{1}H spins (orange arrows, figure 1.1A). In the second step, the enhanced polarization is distributed among the ^{1}H spins of the glassy matrix via nuclear spin diffusion that allows the polarization to travel over distances of up to hundreds of nanometers (purple arrows, figure 1.1A). The efficiency of spin diffusion is sensitive to the ^{1}H concentration in the solvent, which dictates the ^{1}H-^{1}H distance distribution, as well as to $T_1(^1\text{H})$ (proton spin-lattice relaxation). Finally, cross-polarization (CP) using radio frequency (RF) pulses transfers the polarization from the abundant ^{1}H spins to the target lower γ (relatively insensitive) nuclei. As the polarization propagates through the solvent ^{1}H spins, sites inaccessible to the PAs can still be enhanced by this approach, while the undesired paramagnetic relaxation effects of the PAs on the target nuclear spin sites are minimized.[17, 18]

1.3 DNP Mechanisms

DNP mechanisms can be broadly classified based on the number of coupled electron spins participating in the polarization transfer process (figure 1.1B). These mechanisms can be further divided into coherent and incoherent processes depending on the relative strengths of the terms in the Hamiltonian of the system and their contributions to the spin relaxation rates. In a coherent mechanism, μw pulses are used to drive a particular transition in the e-n system, such that the corresponding polarization oscillates between e and n spins. However, exploiting such coherent mechanisms requires further advances in μw technology (high power and pulse phase control) to be implemented at high B_0 field. Incoherent DNP is achieved by saturation of selected EPR transitions of the PA to

achieve a steady-state nuclear spin polarization that is higher than at thermal equilibrium.

In this section, we will discuss pertinent DNP mechanisms within the incoherent regime. The earliest known mechanism is the Overhauser Effect (OE) that involves saturation of the allowed single quantum electron spin transition in a coupled e-n spin system followed by e-n cross-relaxation (figure 1.1B).[19] Although very popular in liquids and conducting solids, OE has not been frequently observed in insulating solids under cryogenic conditions and high field due to the requirement of efficient e-n cross relaxation under cryogenic conditions. Another mechanism for enhancing nuclear spin polarization is the solid effect (SE) that relies on driving an e-n (forbidden) double quantum (DQ) or zero quantum (ZQ) transition, as illustrated in figure 1.1B, and is applicable to many different types of solids.[20] However, these forbidden DQ and ZQ transitions become less probable at higher B_0, rendering SE inefficient.

Alternatively, the Cross Effect (CE)[21] and Thermal Mixing (TM)[22, 23] mechanisms rely on (strong) e-e couplings (tens to hundreds of MHz) to induce simultaneous flip-flop-flip (triple-flip) transitions between two coupled e spins and a hyperfine coupled n (figure 1.1B). For a triple-flip to occur, the difference of the EPR frequencies ($\Delta\omega_e$) of the two coupled e spins must match the nuclear Larmor frequency (ω_{0n}). Usually, if the EPR line is broadened by the g-anisotropies of the two coupled electron spins, CE occurs predominantly. On the other hand, if the dipolar (D) or exchange (J) coupling between electron spins broadens and shifts the EPR line by values greater than ω_{0n}, then TM typically becomes the dominant DNP mechanism.[22] In either mechanism, a large (Zeeman including g-anisotropy) polarization gradient ΔP_e across the EPR spectrum must build up under steady state upon μw irradiation to generate a net nuclear Zeeman polarization enhancement by the triple-flip. The magnitude and the rate of the e-n

polarization transfer is determined by the integrated gradient ΔP_e and the e-e coupling strength (ω_{ee}), respectively. More in-depth discussion of the four DNP mechanisms can be found in the relevant chapters.

To date, the search for PAs (especially for CE DNP) has been driven by optimizing parameters that have been empirically shown to improve DNP, including longer T_{1e} (electron spin-lattice relaxation times) to improve the ΔP_e,[24] mixed radical systems to maximize the triple-flip matching probability ($\Delta\omega_e = \omega_n$),[25, 26, 27] and stronger ω_{ee}.[28, 29] Some of these developments have led to breakthroughs in DNP enhancement at high ($\geq$ 18.8 T) fields with PAs consisting of concentrated BDPA, HyTek, AsymPol and TinyPols.[30, 26, 28, 31, 32] Recent studies have shown that directly diagnosing and optimizing the topology of the e-e coupling network in a real sample (also including their relaxation rates, mutual e-n couplings, and EPR frequencies) provides a more complete approach for optimizing high field CE DNP.[28, 33] EPR detection and quantum mechanical simulations are important tools in this pursuit.

Chapter 2

Role of Electron Spin Dynamics and Coupling Network in Designing DNP

Reprinted with permission from Equbal, A., Jain, S., Li, Y., Tagami, K., Wang, X., & Han, S. (2021). Role of electron spin dynamics and coupling network in designing dynamic nuclear polarization. *Progress in Nuclear Magnetic Resonance Spectroscopy*, 126–127, 1-16.

2.1 Overview

The efficiency and viability of DNP mechanisms rely heavily on the electron spin properties of the polarizing agent (PA). Hence characterization of electron spin parameters is critical to understanding and improving the triple-flip DNP mechanism. Current diagnostics of DNP mostly rely on the analysis of the nuclear spin dynamics (measurements of NMR signal enhancement) as a function of μw irradiation parameters, such

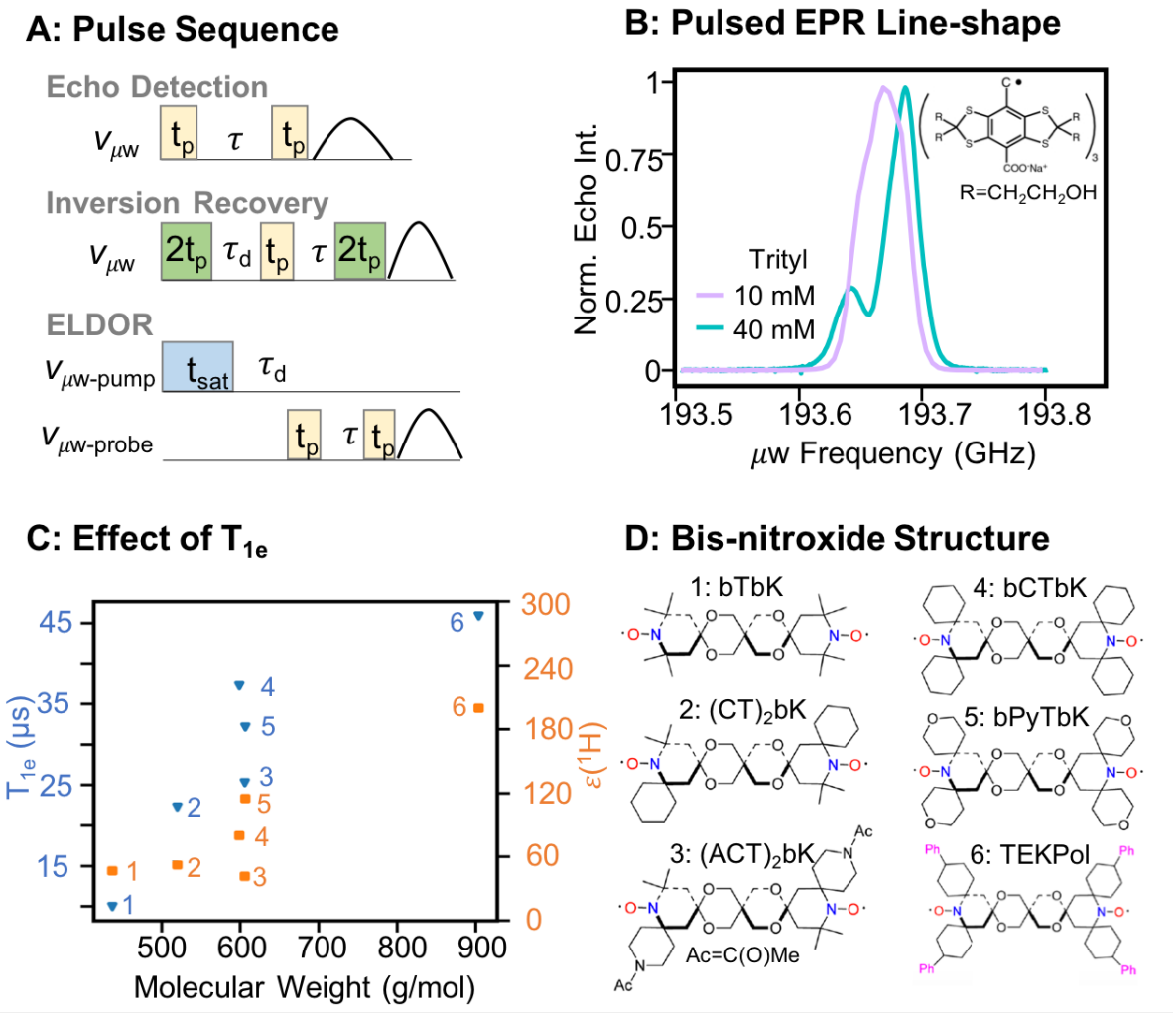

Figure 2.1: **A**: Pulse schematics for EPR experiments. **B**: Echo detected EPR spectra of Trityl-OX063 at 7 T.[34] **C**: T_{1e} (measured at W-band, marked with blue symbols) increases with the molecular weight of a radical (tested up to 905 amu) which results in higher DNP enhancement (measured at 9.4 T, orange symbols).[24] **D**: Structures of bis-nitroxide radicals in **C**. Panels B, C and D are reproduced and modified with permission with modifications from references [34] and [24] respectively.

as resonance frequency, power and irradiation time. Although the e-e-n transfer can be modified by effects of nuclear spin diffusion involving the bulk solvent ^{1}H nuclear spins, NMR signal enhancements provide incomplete insight into the e-e-n transfer process. Clearly, insight into the spin dynamics of both the electron (the source of polarization) and the nucleus (the recipient of polarization) is needed for a comprehensive understanding of processes underlying DNP. Recent studies showed that the direct characterization of EPR spin dynamical properties of PAs under DNP conditions can exhibit surprising or even counter-intuitive features that will foster deeper insight and further developments.[35, 36, 37, 38, 34] Here, we demonstrate three different kinds of EPR data that aid in DNP studies: the continuous wave (CW) and echo-detected EPR line-shape (i.e., the detectable electron spin population vs. resonance frequency/field), the electron spin relaxation rates and the electron spin polarization profiles under μw irradiation obtained by pump-probe experiments. These experiments are vital to gain insight into the e-e coupling network and its effects on the DNP mechanisms. We will present archetypal studies that showcase this point.

2.2 EPR line-shape Analysis

CW EPR line-shape analysis combined with pulsed EPR techniques (figure 2.1A) and DFT (Density Functional Theory) calculations can be used to obtain the g-anisotropy, intra- molecular e-e dipolar and J coupling, e-n hyperfine coupling, as well as the zero field splitting parameters of many-electron spin PAs. Several studies relied on solution-state CW EPR line-shape analysis at X-band (0.35 T) to quantify the e-e J couplings in various biradical PAs.[39, 40, 41] Surprisingly, it was found that different enantiomers of a mixed trityl-nitroxide radical can have highly different J couplings ($\sim$196 and $\sim$6 MHz) that

resulted in dramatically different DNP enhancements (7 and 40, respectively at 18 T).[42]

The CW EPR line-shape is not weighted by relaxation effects. Therefore, CW EPR does not provide direct insights into DNP-active (that can be saturated by μw irradiation) versus DNP-passive (that cannot be saturated) electron spin populations. In contrast, an echo-detected line-shape is modulated by electron spin relaxation times (T_{1e} and T_m), such that the spectrum is dominated by the slow relaxing electron spins that can likely be saturated by μw irradiation. Therefore, an echo-detected EPR spectrum provides a representation of spin packets that can contribute to DNP experiments. In a recent study, echo-detected pulsed EPR experiments aided in the discovery of ^{1}H TM DNP with Trityl-OX063 (between 10-120 K) by revealing an asymmetric EPR line-shape that betrays the presence of heterogeneous spin populations – a condition required for TM, as theoretically predicted by Karabanov *et al*. [43, 34] The asymmetry was a result of an intrinsic tendency of Trityl-OX063 to cluster at radical concentrations exceeding tens of millimoles/liter in a water-glycerol or DMSO solvent (figure 2.1B).

2.3 Role of Electron Spin Relaxation Dynamics

In DNP, there is a tug of war between μw saturation and electron spin relaxation. Specifically, the selective saturation of an inhomogeneous EPR spectrum can give rise to a large electron spin polarization differential, ΔP_e, while T_{1e} relaxation pushes the polarization back towards its thermal equilibrium, thus reducing ΔP_e. Short T_{1e} rapidly reduces the polarization gradient and can lead to low DNP efficiency. This has been the key argument of a study by Ouari, Emsley and co-workers who developed a series of bis-nitroxide radials of the family of bTbk and TEKPOL exhibiting long T_{1e} that correlated

with higher DNP enhancements (figure 2.1C).[24, 44] The strategy was to increase the bulkiness or the molecular weight of nitroxide-based PAs, and in turn slow down their motional dynamics to yield longer T_{1e} with a more rigid molecular framework near the radical center (figure 2.1D). The T_{1e} values of the PA varied from 10 to 45 μs ($\sim$ 15 mM PA concentration, at 100 K and 3.5 T). The DNP enhancements measured at 100 K, 9.4 T and 15 kHz MAS, showed a direct correlation between T_{1e} and enhancement. Increasing T_{1e} increased the observed DNP enhancement. However, long T_{1e} can also induce the detrimental effect of nuclear depolarization under MAS. We hence assume that there is an optimum regime for T_{1e} that should be long enough to maintain saturation, but short enough to replenish electron spin polarization after each rotor event, to avoid the undesirable nuclear depolarization effect under MAS.[45]

It is worth noting that T_{1e} can be highly field dependent, underscoring the importance of measuring T_{1e} under DNP operating conditions.[38] Additionally, T_{1e} may vary significantly across a heterogeneously broadened EPR-line.[46] Identifying the spectral heterogeneity of T_{1e} is especially relevant for DNP if two distinct spin populations are strongly overlapping, or if one of them is spectroscopically invisible due to fast relaxation, while its presence still influences the DNP mechanisms. The comparison of CW and pulsed EPR spectra can reveal the presence of fast relaxing electron spin populations. One such example was demonstrated with the *truncated* Cross Effect (tCE) DNP generated between a slow relaxing (narrow-line) Trityl radical and a fast relaxing radical cluster whose spectrum was severely broadened.[38] The discovery of tCE that had a similar appearance as Overhauser Effect DNP according to the NMR-measured DNP profile alone reinforces the importance of the measurement of electron spin dynamics in deciphering underlying DNP mechanisms.

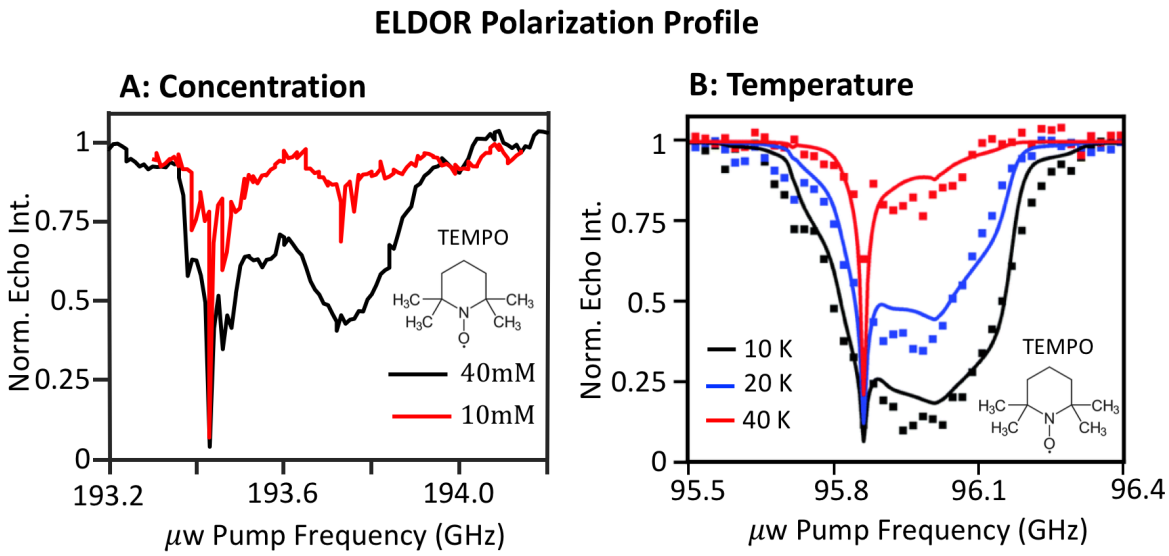

Figure 2.2: **A**: Concentration dependent ELDOR spectra of 10 mM and 40 mM TEMPO acquired at 4 K and 6.9 T with a probe frequency set to 193.45 GHz. A larger width of saturation at higher concentration implies larger electron spectral diffusion (eSD) driven by the stronger *e*-*e* couplings. **B**: Temperature dependent ELDOR spectra of 40 mM TEMPO acquired at 3.3 T and at variable temperatures: 10, 20 and 40 K. Larger width of saturation (or larger eSD) at lower temperatures is a manifestation of longer T_{1e} at lower temperatures. Panels A and B are reproduced and modified from references [47] and [48] respectively with permission.

2.4 Characterizing the *e*-*e* Coupling Network

DNP mechanisms and their efficiency strongly depend on the topology of the *e*-*e* coupling network and on the number of coupled electron spins participating, as illustrated in figure 1.1B. The *e*-*e* coupling in a dilute (sub mM) bi- or tri-radical can be obtained using a combination of EPR measurements and DFT calculations. However, determining the topology of the coupling network in a concentrated radical system is not straightforward, especially because in a typical DNP experiment the PA molecules (used at concentrations of 10-50 mM) cannot be treated as systems of isolated electron spins. Additionally, the inter-radical couplings between electron spins can adopt uneven spatial distributions throughout a vitrified sample depending on radical-solvent and radical-radical (chemical and physical) interactions. To uncover properties of the *e*-*e* coupling network, we turn

to two-dimensional pump-probe pulsed EPR measurements. The idea is to perturb the electron spins by mimicking the effect of microwave irradiation under DNP conditions, and then detect the resulting electron spin polarization that is dictated by the e-e spectral diffusion across the EPR line.

In a pioneering study, Hovav, Feintuch, Vega and Goldfarb introduced multi-frequency pump-probe Electron-Electron Double Resonance (ELDOR) measurements as a means of studying the e-e coupling network under DNP conditions.[49] The pump channel saturates the electron spin polarization to emulate the μw irradiation condition used in DNP experiments. The probe channel measures the polarization of electron spins at the selected probe frequency. This measurement reveals the role of electron spectral diffusion (eSD), which results in the spread of saturation across a wide frequency range that exceeds the bandwidth of the μw pulse. The saturation of spins via eSD is governed by the combined effect of the e-e coupling strengths (that determine the e-e flip-flop transition rate) and electron spin relaxation. Figure 2.2A shows ELDOR polarization profiles measured at 4 K and 6.9 T for a fixed probe frequency (193.45 GHz), while the μw pump frequency is varied through the complete EPR spectrum, for 10 and 40 mM TEMPO dissolved in water-glycerol. The eSD becomes dominant when inter-radical coupling is large (at 40 mM), demonstrating that eSD is a qualitative indicator of the e-e coupling network. The extent and width of electron spin saturation also increases with T_{1e}, e.g. at lower temperatures. Figure 2.2B shows ELDOR polarization profiles of 40 mM TEMPO at a fixed probe frequency (95.86 GHz), acquired at three different temperatures, 10, 20 and 40 K, in a 3.3 T field. Clearly, eSD is more prominent at 10 K as revealed by the wider saturation dip compared to higher temperatures.

A complete two-dimensional electron spin polarization profile can be generated by

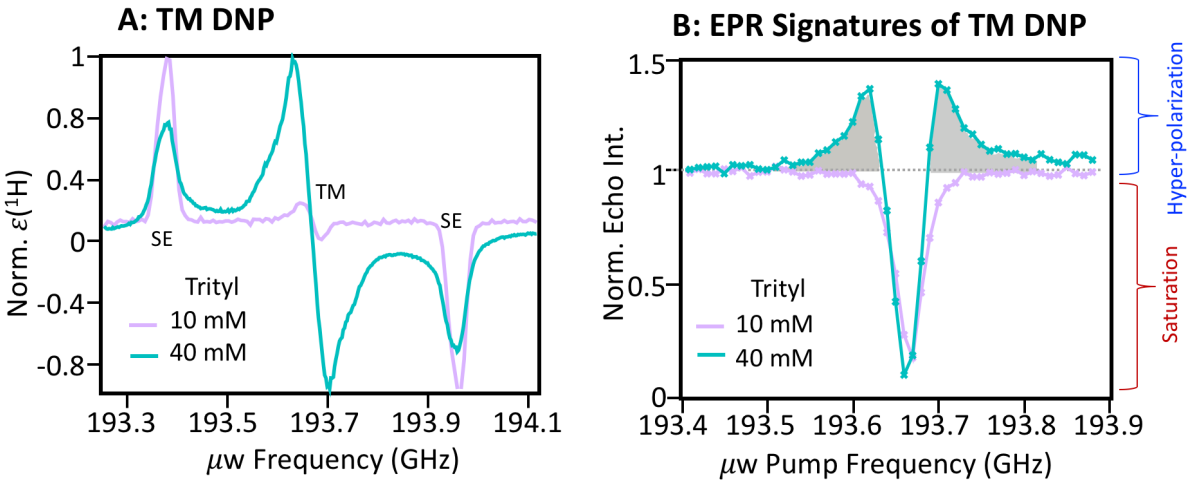

Figure 2.3: **A**: DNP frequency profiles of 10 mM (violet) and 40 mM (mint) Trityl-OX063 at 20 K and 6.9 T. The prominent ^{1}H DNP mechanism undergoes a crossover from SE to TM at the higher concentration of Trityl. **B**: The ELDOR profiles measured for the two concentrations near the Trityl-OX063 center frequency. Hyperpolarization at 40 mM (shaded in gray) reveal the EPR signatures of TM DNP. The figures are reproduced and modified from reference [34] with permission.

measuring ELDOR profiles at different probe frequencies and by deconvoluting the relative contributions of different DNP mechanisms. Hovav et. al. developed a numerical model to use the two-dimensional ELDOR polarization profile to reconstruct the DNP frequency/field profile.[48] The model provided critical insights in distinguishing the direct CE (where ΔP_e is achieved by direct μw irradiation of one the two electrons inducing CE) and the indirect CE (where ΔP_e between the two electrons is generated as a result of eSD and not via direct irradiation). It was revealed that indirect CE is the major mechanism responsible for bulk DNP at all three temperatures.

Recently, we observed ^{1}H TM DNP using a narrow-line (i.e., with a g-anisotropy smaller than ω_{0n}) water-soluble Trityl-OX063 radical at 7 T. Surprisingly, the DNP mechanism crosses over from SE to TM with increasing concentration of Trityl-OX063 between 10 and 40 mM (figure 2.3A). ELDOR measurement served as a powerful diagnostic tool

to unambiguously identify a TM signature in a strongly coupled spin system, as had been numerically predicted by Vega and co-workers.[50] Their key prediction was the generation of the hyperpolarization (or cooling) of selected electron spin resonances under the effect of TM DNP, when the μw pump frequencies is set at some distance from the probe frequency.[34] Figure 2.3B shows overlaid ELDOR polarization profiles (normalized with respect to the Boltzmann polarization) for two different Trityl-OX063 concentrations. Clearly, in the sample containing 40 mM of the PA, TM is the dominant DNP mechanism. An increase in the polarization of electron spins above the thermal Boltzmann distribution is observed when the μw pump frequency is set at an offset with respect to the probe frequency. The hyperpolarized electron signal is highlighted in gray. When μw pump and probe frequencies are close, only saturation of the EPR signal (shown as a dip in intensity in the ELDOR profile) is observed for both PA concentrations.

2.5 Quantum Mechanical Modeling of Spin Physics

The DNP pathways and their efficiencies depend on a multitude of different intertwined parameters. Quantum mechanical (numerical) simulations offer a unique handle to selectively monitor the effect of different spin dynamics parameters and to dissect and understand DNP at a microscopic level. [51, 52, 53, 27, 33] Figure 2.4 illustrates the model of a PA (bis- nitroxide for CE DNP) with parameters including the relative g-tensor orientation, the *e*-*e* dipolar coupling between two coupled electron spins, as well as T_{1e}. The calculation of the proton enhancement $\epsilon(^1\text{H})$ for a typical bis-nitroxide under MAS predicts that: (i) a sufficiently long T_{1e} (i.e., above a threshold) is critical for efficient DNP, but an excessively long T_{1e} becomes deleterious, (ii) there are preferable relative g-tensor orientations between two coupled electron spins that maximize CE DNP,

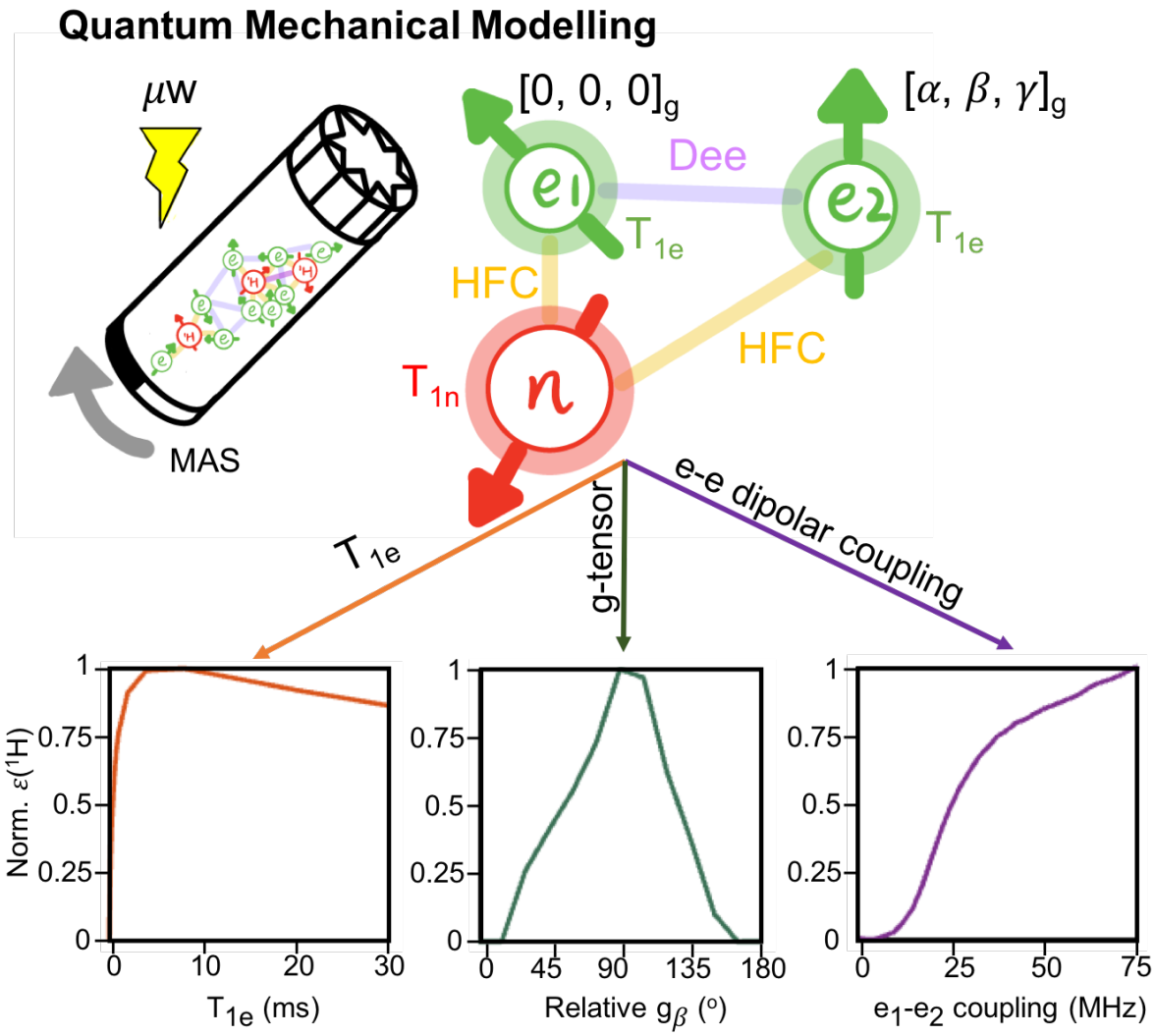

Figure 2.4: Quantum mechanical modeling of T_{1e}, relative g-tensor orientations and dipolar coupling in bis-nitroxide radicals under 25 kHz spinning in a field of 18.8 T using 0.5 MHz μw nutation frequency.

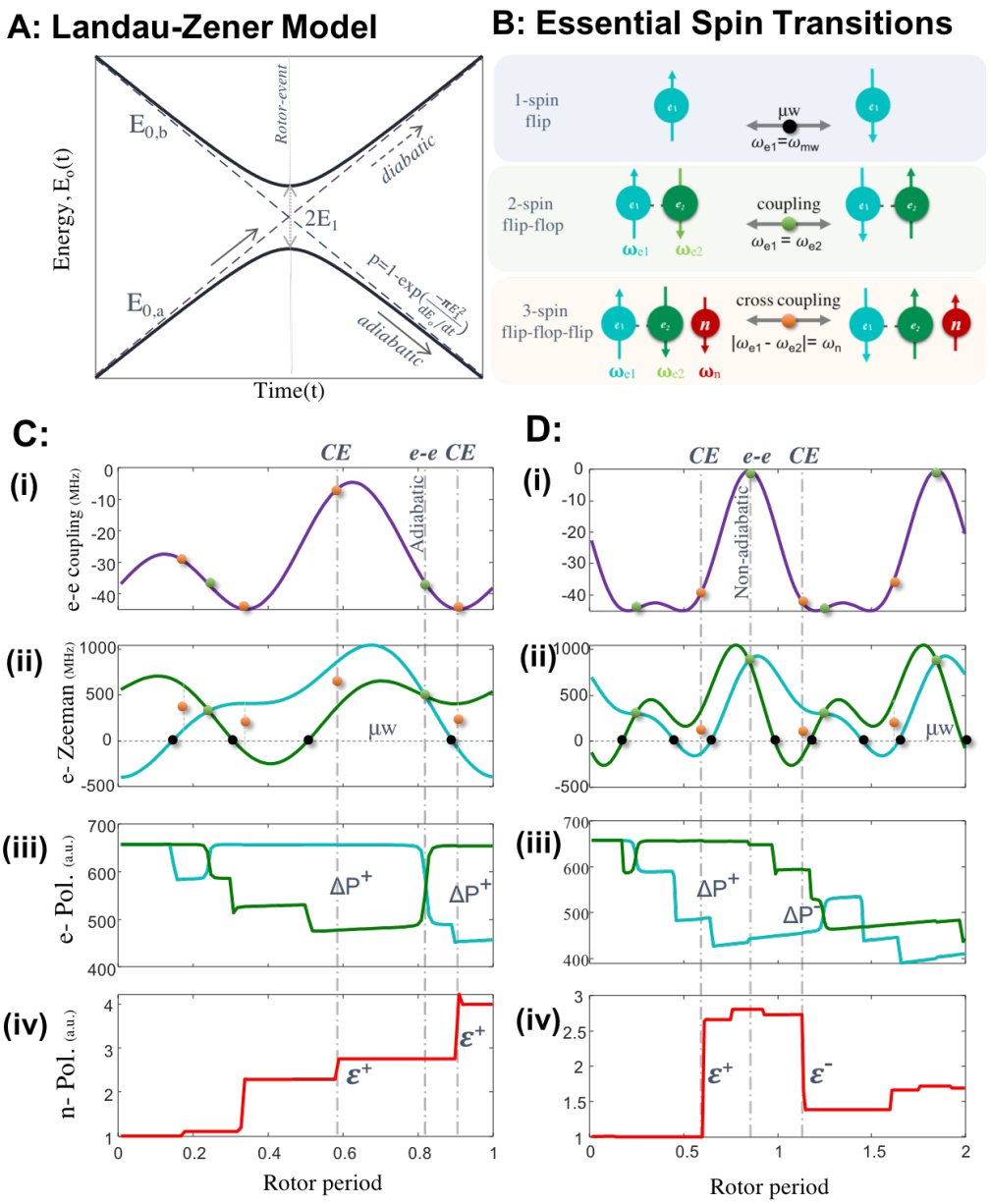

Figure 2.5: **A**. Landau-Zener population transition model used to rationalize spin dynamics under MAS. **B**. Schematic representation of essential spin transitions involved in CE DNP. **C**. Plot of *e*-*e* coupling (panel *i*) and *e*-Zeeman energies in rotating frame (panel *ii*), the electron and nuclear spin polarizations (panels *iii* and *iv*, respectively). The rotor events μw, *e*-*e* and CE are marked with black, green and orange symbols. The *e*-*e* couplings at the green *e*-*e* rotor events are large and therefore corresponding transitions are adiabatic. **D**. Similar to **C** but for a different crystallite orientation that leads to inefficient DNP. A non-adiabatic *e*-*e* event impedes the net DNP enhancement. The energies and polarizations were calculated using SpinEvolution package.

and (iii) generally, stronger *e*-*e* dipolar couplings enhance the DNP performance (up to a threshold value), largely validating experimental observations. These profiles were calculated by varying a selected parameter (shown along the x-axis) while keeping all other parameters constant (typical for bis-nitroxides).[53, 28, 41] Notably, EPR measurements of spectral (J coupling, g-tensor) and relaxation (T_{1e}, T_{2e}) properties offers critical input to accurately carry out the relevant DNP simulations.

In this section, we will focus on how quantum mechanical analysis can enhance our understanding of the role of the DNP parameters. We will focus on CE DNP, which is the most accessible mechanism for MAS DNP. Notably, the widely used average Hamiltonian theory or Floquet theory cannot be straightforwardly applied to study time-dependent interactions involving electron spins under MAS, as the strength of these interactions are much larger than the MAS frequency itself.[54]

2.5.1 Landau-Zener Model

A major development in the (quantum mechanical) understanding of the CE DNP mechanism under MAS came from the description of dynamic electron spin transitions using the Landau-Zener (LZ) model, as delineated by Tycko and Thurber,[55] and subsequently by Mentik-Vigier *et al.*[56] Their studies contributed to unraveling the distinctions between of MAS DNP and static DNP. Under MAS the essential spin transitions leading to μw excitation and other spin flip-flop events are separated in time (unlike under static conditions) because of energy modulation in time owing to anisotropic interactions of the electron spins (i.e., the g tensor anisotropy and dipolar *e*-*e* couplings). The energy modulation causes a series of time-dependent and periodic resonance conditions

(a.k.a. rotor events) where spins may transition from one state to another. The changes of spin populations between energy states at a rotor event where a resonance condition is met can be analyzed by the LZ model. According to this model, the probability for population exchange (p) at each rotor event depends on the rate of change of the energy of the states ($\frac{dE_0}{dt}$) and the magnitude of the perturbation (E_1) at the rotor event according to the following equation:

$$p = 1 - exp(-\pi * E_1^2/(\frac{dE_0}{dt})). \tag{2.1}$$

Figure 2.5A represents a level anti-crossing (rotor event) in a two energy-level system. The dashed lines represent the energies of the diabatic states (diagonal terms of the Hamiltonian, E_{0a} and E_{0b} not including the perturbation term). The solid lines represent the energies of the adiabatic states of the Hamiltonian (eigenvalues of the full Hamiltonian, including the perturbation term). The rotor event is said to be diabatic if there is negligible exchange of the spin populations between the energy states, while an adiabatic transition refers to a complete exchange of the spin populations between the states (see figure 2.5A). These concepts are pedagogically explained in a recent review article by Ivanov and coworkers.[57] As mentioned above, CE involves two essential transitions: (i) μw event: selective saturation of one of the electron spin polarizations in resonance with the irradiating μw frequency (i.e. $\omega_{e_i} = \omega_{\mu w}$), and (ii) CE event: simultaneous triple-spin flip of e-e-n at the CE resonance condition (i.e. $\omega_{e_1} - \omega_{e_2} = \pm\, \omega_n$). There is another very critical transition, the e-e event that occurs when the two electron spins become degenerate ($\omega_{e_1} = \omega_{e_2}$), leading to the partial or complete exchange of polarization between e_1 and e_2 spins. These transitions or the rotor events are illustrated in figure 2.5B.

Using the basic understanding of the LZ model, we now address an important ques-

tion: what determines the DNP efficiency of a polarizing agent? The DNP enhancement is highly orientation dependent, and encoded in the energy trajectories of the energies of the states which determine the sequence of the rotor events. Additionally, the relaxation time constant T_{1e} relative to the rotor period (τ_r) determines whether the effect of the different rotor events can add up constructively or not. Very short T_{1e}/τ_r will relax the system back to thermal equilibrium in between the rotor events.

We illustrate these nuances using two selected orientations, one leading to efficient DNP and the other to inefficient DNP. Figure 2.5C-D maps the *e*-*e* coupling energies (panel *i*) and Zeeman energies in the rotating frame (panel *ii*) of two electron spins (e-*e*-*n* with $n = {}^1$H spin system) in the μw rotating frame for an *e*-*e*-*n* crystallite orientation that leads to high (figure 2.5C) and low (figure 2.5D) DNP enhancements. The modulation in panel (*i*) results from the dipolar anisotropy of the *e*-*e* coupling. The coupling energy spans the range $[\frac{-D}{2} + J, D + J]$. The modulation in panel (*ii*) results from the g-anisotropy of the electron spins. Panels (*iii*) and (*iv*) map the polarization profiles of the two electrons and the nucleus, respectively.

The rotor events, involving one (μw event), two (*e*-*e* events) and three spins (CE event), are marked by black, green and orange symbols, as their resonance conditions are satisfied at different time points within a rotor period. Essentially, a μw event (time point where the Zeeman energy of one of the electrons becomes zero, (marked by horizontal dotted lines) in the μw rotating frame generates a polarization difference between the two electron spins (panel *ii*). The change in the polarization of the two electron spins can be monitored in panel (*iii*) of figure 2.5C-D.

$$\text{perturbation strength of CE transition} \approx \frac{\omega_{e_i e_j}(\omega_{e_i n} - \omega_{e_j n})}{\omega_{0n}} \tag{2.2}$$

The nuclear polarization enhancement occurs with the triple *e*-*e*-*n* spin flip transition, here referred to as the CE rotor event, in a step-function by an amount that is proportional to ΔP_e accumulated prior to this event (also illustrated in figure 2.5). These transitions are marked with orange symbols, where the difference of electron spin energies matches the nuclear Larmor frequency, i.e. 300 MHz for ^{1}H at 7 T (panel *ii*). The transition probability can be calculated using the LZ equation, where the perturbation E_1 depends on the product of the *e*-*e* coupling and the relative *e*-*n* coupling as shown in equation 2.2. The corresponding step-wise buildup of nuclear spin polarization of the selected orientation under MAS is shown in panel (*iv*) of figure 2.5C-D.

Maintaining high adiabaticity, especially for all *e*-*e* events in a rotor period, is key to achieving high CE DNP under MAS. A favorable *e*-*e* event leads to an exchange of electron spin polarization, provided that the instantaneous *e*-*e* coupling is large enough at the event.[55, 56] This is important to maintain the electron spin polarization gradient, as well as to maintain the same sign of the polarization difference $\Delta P_e = P_{e_1} - P_{e_2}$ and the frequency difference $\Delta\omega_{0e} = \omega_{e_1} - \omega_{e_2}$. To understand this nuance, let us focus on the *e*-*e* event, which is interleaved between two CE events (figure 2.5C, panel $ii - iii$) as highlighted with dashed vertical lines. Prior to the *e*-*e* event, the polarization difference ΔP_e between the two electrons with respect to their frequency difference $\Delta\omega_{0e}$ and the corresponding DNP enhancement is positive, ϵ^+ (figure 2.5C panel *iv*). After the *e*-*e* event, the electron frequency difference changes the sign (i.e., the green symbol is higher and the cyan symbol is lower in energy). For the CE DNP to constructively add up, the polarization of the two electron spins should swap, so to maintain the polarization

difference, and maintain its sign with respect to the frequency difference. This requires that the e-e event is adiabatic (i.e. $p \sim 1$ in equation 2.1), contributed by a large e-e coupling at the event, as seen in figure 2.5C. Then, a large DNP enhancement is achieved. In contrast, if the e-e event (highlighted with dashed line) is diabatic or non-adiabatic, as illustrated in figure 2.5D panels $i - iv$, and the relative sign of ΔP_e and $\Delta\omega_{0e}$ is not maintained at the two different CE events (before and after the e-e event as highlighted), this can lead to self-cancellation effects for DNP. Also, the large ΔP_e is not maintained at steady state. Notably, even a single non-adiabatic e-e event can lead to poor DNP enhancement for the select orientation (figure 2.5D, panel iv). In a nutshell, the sequence of the rotor events, the adiabaticity of these transitions and the relative T_{1e}/τ_r all contribute to the CE DNP efficiency of a given crystallite or molecular orientation. An ideal PA will be one with maximum adiabatic transition probabilities for all e-e events in a rotor period, and is fulfilled for a large number of orientations in a powder ensemble.

2.5.2 Design of New Polarizing Agents

A major research topic in MAS DNP has been the design and synthesis of biradicals that are more efficient at high B_0 and fast MAS frequency. In particular, the search for a bi-radical with optimum e-e coupling has been an important research focus. Initially, the optimization of the biradicals was based on the optimization of the dipolar coupling and g-anisotropy through variation of the chemical linker connecting the radical centers. The aim was to optimize (i) the length of the linker and thereby the dipolar coupling and (ii) the rigidity of the linker to ensure an optimum relative orientation of the g-tensors of the two radical centers in the bi-radical. This design approach is further being refined by considering the role of exchange or J coupling.[28, 41, 26]

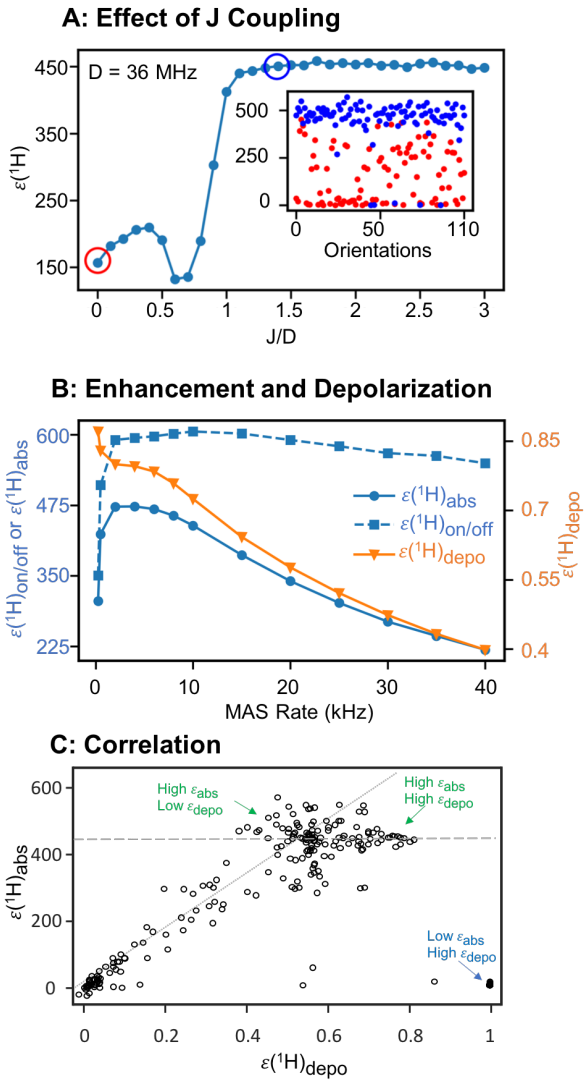

Figure 2.6: **A**. ^{1}H DNP vs. J/D in bis-nitroxide exhibiting the requirement of an optimal J/D for maximum enhancement. Non-optimal J/D of ∼0.7 results in strong interference in bis-nitroxides with perpendicular g-tensors. **B**. Measured ^{1}H DNP enhancement $\epsilon_{on/off}$ on left y-axis, and nuclear depolarization (ϵ_{depo}) on right y-axis for a powder sample. The more meaningful ϵ_{abs} is defined as $\epsilon_{on/off}$*$\epsilon_{on/off}$. This shows that the factor $\epsilon_{on/off}$ overestimates the actual DNP enhancement. **C**. Numerically simulated correlation between enhancement and depolarization for 230 different crystallite orientations mimicking AMUPol spin parameters at 12.5 kHz MAS and 18.8 T field. Figure A is adapted from reference [33] with permission. Figure B was simulated numerically using SpinEvolution under 25 kHz spinning and 18.8 T field using 0.5 MHz μw nutation frequency.

Sigurdsson, De Paëpe and coworkers have designed an asymmetric bis-nitroxide radical, AsympolPOK, to maximize the CE DNP efficiency while minimizing the depolarization effect; it is reportedly the best performing bis-nitroxide radical at 18 T to date.[28]

Recently, we discovered the importance of balancing the relative magnitude of J and D in a biradical for maximizing the enhancement in a powder sample.[33] This is illustrated in figure 2.6A that shows simulated ^{1}H DNP enhancements as a function of the relative J/D values in bis-nitroxide radicals. We discovered that not only the sum J+D, but also the ratio of J/D needs to be balanced (specifically in the range $1 < J/D < 2.5$) to achieve robust enhancement for all radical orientations.[33] The recently developed TinyPol PA is a very appropriate example to highlight the necessity of balancing J and D coupling. Compared to AMUPol, the TinyPol radical has a smaller linker, and therefore much enhanced dipolar coupling ($\sim$ 40 MHz). However, the J coupling ($\sim$ 22 MHz calculated using DFT) of a large number of conformers falls in a non-optimum regime ($J/D \sim 0.55$), hence rendering its performance far below that than initially expected. In fact, the key strategy to boost DNP efficiency at high B_0 and fast MAS is to enhance the ratio of the isotropic J coupling and the anisotropic D coupling between the CE-inducing electrons spins. This strategy minimizes the interference effects between the two interactions and maximizes the effective *e*-*e* couplings at all radical orientations, thus ensuring large adiabaticity for the *e*-*e* and CE rotor events. In all transitions, again, maintaining high adiabaticity is the key for achieving efficient DNP. The adiabaticity of CE rotor-events is the smallest in magnitude (relative to other two rotor-events) as it is a second order perturbation term77 that is proportional to the product of *e*-*e* and the difference between two *e*-*n* couplings and is scaled down by the nuclear Larmor frequency (equation 2.2).

Therefore, the adiabatic transition probability of the CE event becomes smaller with increasing magnetic field. The loss of adiabaticity of the CE event at higher field can be compensated for with an increase in the e-e coupling, as reflected in equation 2.2.

2.5.3 Depolarization Effect under MAS

DNP enhancement is generally evaluated by comparing the NMR signal intensities under μw-on and -off conditions, i.e. ($\epsilon_{on/off}$). However, when evaluating the DNP efficiency, it is important to consider the effect of nuclear depolarization (ϵ_{depo} = Signal under MAS/Signal under static) under MAS too, i.e., the loss of nuclear polarization to electrons via the same CE mechanism under MAS and μw-off condition (figure 2.6B).[58] The effect is a manifestation of non-adiabaticity of some e-e rotor events. Under such conditions, ΔP_e decreases and can lead to nuclear depolarization via reverse nucleus-to-electron CE transfer. The effect becomes severely pronounced as the ratio T_{1e}/τ_r increases, i.e. when a low ΔP_e ($\leq P_n$) is maintained throughout the rotor period.[58, 59, 45] Since both effects are manifestations of the triple-flip mechanism, we mapped their correlation for 230 different orientations of a e-e-n spin system that is designed to mimic the e-e coupling strength of the AMUPol radical.[39, 33] Similar to the observation made by Mentink-Vigier *et al*. for TOTAPOL radicals,[59] we find a linear correlation between ϵ_{depo} and the realistic enhancement factor, $\epsilon_{abs} = \epsilon_{on/off}{}^{*}\epsilon_{depo}$ (marked by the dotted line in figure 2.6C). Specific orientations can be beneficial or detrimental in minimizing depolarization and maximizing DNP enhancement. Interestingly, there are some orientations that deviate from the statistical correlation of enhancement vs. depolarization in the powder ensemble, although the sequence of CE and e-e rotor events are identical in both

enhancement and depolarization processes. This is due to μw events. The time-sequence of the μw events with respect to the other two events determines the DNP enhancement actually accrued. Consequentially, a given orientation can lead to significant depolarization but also have a very high DNP enhancement, as highlighted with the horizontal line in Figure 2.6C. Interestingly, this suggests that the presence of moderate depolarization ($0.6 < \epsilon_{depo} < 0.8$) can be an indicator of efficient CE DNP activities of bis-nitroxide PAs that have long T_{1e} and optimum relative g-orientations.

2.5.4 MAS rate Dependence of CE DNP

The insights provided by the LZ model explain the complex behavior of the DNP enhancement as a function of the MAS frequency (ν_r). The effective DNP enhancement is an interplay of the number of rotor events per unit time (which increases with ν_r) and their adiabaticity (which decreases with ν_r). As a result, the CE DNP enhancement for the common AMUPol radical (ϵ_{abs}) sharply increases with ν_r compared to static conditions. The enhancement reaches an optimum, then levels out, and subsequently deteriorates at very fast MAS (figure 2.6B). The exact position of this optimum depends on the e-e coupling strengths, as they determine the adiabaticity of the events. The CE DNP benefits from the effect of MAS that incorporates a large number of orientations to fulfill the CE polarization transfer condition – an effect dubbed as "self-chirping".[55]

2.5.5 Design of New μw Irradiation Scheme

The LZ theory has played a key role for the development of new μw pulse irradiation schemes to achieve efficient DNP with fast $1/T_{1e}$ rates. The microscopic insights of μw

and CE rotor-events under MAS that are separated in time inspired the idea to execute fast and broadband irradiation to maintain a gradient ΔP_e throughout all CE events that occur during sample rotation and result in a larger DNP enhancement.[60] So far, we demonstrated the importance of numerical simulations to understand and develop DNP. Next, we highlight the available packages to perform these simulations.

2.5.6 DNP Numerical Simulation Packages

SpinEvolution (C based) and Spinach (MATLAB based) are two simulation packages that are available for general users to carry out quantum mechanical simulations of DNP effects that incorporate all relevant experimental parameters (including relaxation rates).[61, 62] Spinach is a freeware developed by Kuprov and coworkers.[62, 63] SpinEvolution was developed by Veshtort *et al.*[61] and has been commercialized, but is significantly more rapid for DNP simulations compared to Spinach. For example, a typical CE DNP profile (e.g. as shown in figure 2.3A) can be computed in a few minutes using SpinEvolution, but may take several hours by Spinach. Of course, the exact simulation duration depends on the magnitude of the different terms in the relevant Hamiltonian describing the spin system, especially of the off-diagonal or the perturbation terms. We used SpinEvolution to carry out numerical simulations in all of our recent studies after the program's functionality was extended to include the capability to simulate DNP phenomena. We found this tool indispensable for simulating and understating effects of the truncated CE and TM DNP mechanism that we observed experimentally, and predicting the characteristics of new bis-nitroxide and mixed radical systems as PAs.[64, 38, 34, 33, 41, 27, 65]

Just as with numerical simulations of other types of NMR experiments, DNP simu-

lations are performed by the numerical integration of the time-dependent Liouville-von Neumann equation of motion. The Hamiltonian (equation. 2.3) has the following form in this case:

$$\hat{\mathcal{H}} = \hat{\mathcal{H}}_{\text{Zeeman}} + \hat{\mathcal{H}}_{e-e} + \hat{\mathcal{H}}_{\text{hyperfine}} + \hat{\mathcal{H}}_{\mu w} \tag{2.3}$$

This includes the pseudo-secular ($I_x S_z + I_y S_z$) parts of the hyperfine coupling terms and uses the lab frame for the nuclei I, while a rotating frame is used for the electron spins S. The electron spin relaxation terms are assumed to be of the form generated by fast random fluctuations of the single-spin operators, having phenomenological relaxation time-constants (T_1 and T_2). The $\mathcal{H}_{\mu w}$ term may have an arbitrary time-dependent frequency and amplitude. Paramagnetic spin systems with effective spin quantum number $S > 1/2$ are allowed in addition to spin 1/2 electrons. Calculations of MAS DNP are particularly challenging because the integration of spin dynamics must be performed in very small-time steps (typically on the order of 10 ns). The situation is further complicated by the incorporation of relaxation in the equation of motion, necessitating calculations in Liouville space, which makes such calculations very expensive compared with conventional MAS ssNMR simulations where pseudo secular terms are ignored and spin interactions are much smaller in magnitude so that their numerical diagonalization is easier. To alleviate this problem SpinEvolution uses a set of algorithms that integrate the equation of motion in such systems much more efficiently than the straightforward methods used by other authors.[55, 56] The method set includes the Liouville space, reduced Liouville space and Hilbert space algorithms. The latter methods (although not exact) are useful for dealing with very large spin systems, where calculations in Liouville space become exponentially time consuming. In particular, the method used by Thurber and Tycko[55] is a special case of the SpinEvolution's Hilbert space algorithm. Most recently, Perras

and co-worker incorporated the LZ formalism with locally restricted low-level correlations using the Liouville space method that can allow for simulations of systems containing thousands of spins.[66] The method is not exact and truncates the spin interactions to the nearest neighbor, yet it can be very helpful for understanding bulk phenomena such as nuclear spin diffusion in presence of electrons.

Chapter 3

Electron Spin Density Matching for Cross Effect DNP

Reprinted with permission from Li, Y., Equbal, A., Tagami, K., & Han, S. (2019). Electron spin density matching for cross-effect dynamic nuclear polarization. *Chemical Communications*, 55(53), 7591-7594.

3.1 Introduction

DNP normally requires exogenous polarizing agent (PA), to transfer polarization from its unpaired electron spins to coupled nearby nuclei, which is subsequently relayed to the bulk nuclei through the nuclear spin-diffusion mechanism. While many interesting applications of DNP-NMR have been demonstrated already, a prime research objective for DNP is to enhance its performance under the desired experimental conditions, including at high B_0, fast magic angle spinning (MAS) and/or at higher temperatures, while minimizing the microwave (μw) power requirement.

Among the different DNP mechanisms in insulating solids, the Cross Effect (CE)[67] is the most promising mechanism at high B_0 and with the currently available state of the art μw instrumentation.[68] The CE relies on three-spin dynamics (two coupled electron spins, e, differently coupled to a nuclear spin, n), and is induced by two essential spin transitions: (i) the quantum mechanically allowed μw transition that depolarizes the ensemble of one of the two e spins involved in the CE transfer, thereby creating a large polarization difference between the two e spins relative to the n spin polarization, and (ii) the simultaneous flip-flop-flip of all three spins induced by second-order cross-terms between the e-e and $e-n$ couplings. This is achieved when the CE resonance condition, $|\omega_{e1} - \omega_{e2}| = |\omega_n|$, is satisfied.[55, 56] Maximizing the CE transfer therefore requires maximizing the transition probabilities of these two processes.

The first break-through in CE radical design was accomplished by Hu *et al.* who introduced bis-nitroxide radicals.[69] Thereafter, efforts have been devoted to optimize the electron spin relaxation rates, linker size, molecular geometry, and solubility.[69, 70, 71, 72] However, bis-nitroxide radicals loses efficacy at high B_0 field and under fast MAS, conditions under which the relevant adiabatic CE transition probabilities decrease.[56]

A promising solution to this dilemma emerged from the discovery of Hu *et al.*,[73] showing that mixed Trityl (narrow line) and TEMPO (broad line) radicals display favorable g-tensor difference that can effectively increase the CE e_1-e_2 spin pairs for ^{1}H DNP. This mixture improved the CE DNP enhancement by a factor of 3 compared to an equivalent amount of TEMPO at 90 K, 5 T, 5 kHz MAS, when using high-power (10 W) μw irradiation. Taking advantage of this favorable condition, significant efforts have been invested into synthesizing a PA archetype of a broad nitroxide radical tethered with a narrow Trityl or a BDPA radical, while preserving their anisotropic g-tensor

features [74, 75] for efficient DNP, as first successfully demonstrated by Mathies *et al.* for TEMPO-Trityl, [76] and recently by Wisser *et al.* for TEMPO-BDPA.[75]

In this study, we add a new perspective for further enhancing the CE DNP of mixed radical-based PAs by matching the electron spin density for the broad and narrow line radicals. The conceptual underpinning for testing ratios other than 1:1 (conventional) between the broad and narrow radical is that the two radicals have very different EPR linewidths and relaxation properties.[38] This raises an obvious question- Is 1:1 ratio of the radicals the optimum composition? The question we address is whether a significant boost in the DNP enhancement can be achieved under static and MAS conditions by matching the electron spin density for Cross Effect DNP. The outcome of this study will offer a key design principle for the type and composition of mixed-radicals that maximize their DNP performance.

An ideal testing system would be a narrow line radical tethered to more than one broad line radicals. However, the synthesis of such radical system, and searching for the adequate length and geometry of the chemical linker is synthetically challenging, especially when a Trityl or a BDPA radical is involved. Before proposing with the design and synthesis of such systems, the viability of this concept must be tested first. To this end, we carried out the initial test by increasing the relative portion of the broad line radical in the physical mixture of Trityl and TEMPO. In this study we chose not to focus on the physical mixture of TEMPO and BDPA, another commercially available narrow line radical, given the low solubility of BDPA in toluene which significantly impairs the CE probability between the two radicals. The here reported DNP experiments were performed under static, as well as MAS conditions, at 6.9 T powered by a tunable solid-state microwave source.[77, 78, 79] Two factors will be closely investigated: the change

in DNP enhancement factor and the DNP buildup rate, as these factors constitute the DNP enhancement per unit time.

3.2 Experimental Methods

Static DNP/EPR Sample 4-Amino TEMPO, denoted as TEMPO, (Sigma-Aldrich) and Trityl-OX063, denoted as Trityl in this chapter, (GE Healthcare AC) with a total radical concentration of 30-53.2 mM were dissolved in DNP Juice, d_8-glycerol (Cambridge Isotopes):D_2O (Cambridge Isotopes):H_2O (UCSB Lab) = 6:3:1, $vol\%$. 40 μL mixed radical solution was deposited into a cylindrical Teflon sample holder. Further description of the sample holder and 6.9 T static pulsed DNP/EPR instruments can be found in the appendix.

3.3 Results and Discussion

3.3.1 Electron Spin Relaxation Measurements

The T_{1e} relaxation time was measured for Trityl and TEMPO at DNP conditions using saturation recovery experiment. The pulse scheme is shown in figure 3.1(a). 100 ms, $P_{\mu w}$ = 120 mW μw pulse was used to saturate the electron spins at the probe frequency, ν_{probe}. The EPR signal intensity was recorded at the same frequency using solid-echo detection, following a variable recovery delay, τ_D. T_{1e} was measured for three different radical mixtures, (a) TEMPO:Trityl = 1:1 (C_{total} = 30 mM, blue), (b) 2:1 (C_{total} = 30 mM, red). Two-component exponential fitting, using the equation, $I = I_0(1\text{-}A*(\exp(-\tau_D/T_{1e-slow}))\text{-}B*(\exp(-\tau_D/T_{1e-fast})))$, was used to extract the T_{1e} values recorded for

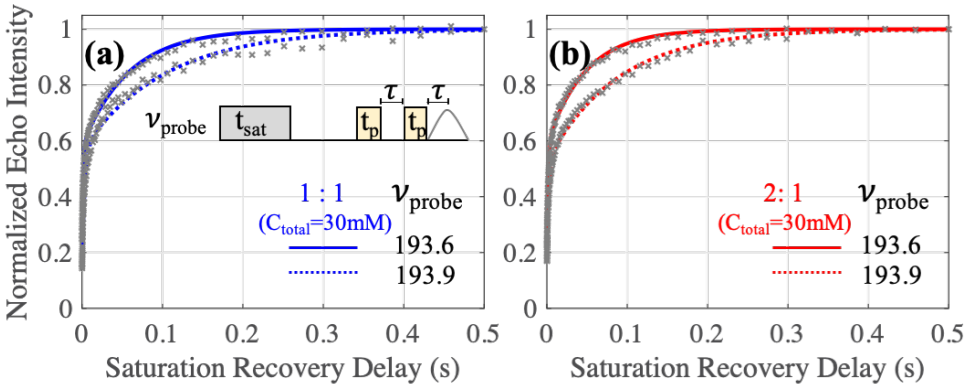

Figure 3.1: Saturation recovery T_{1e} measurement at 4 K for two different radical-mixtures: (a) TEMPO:Trityl = 1:1 (C_{total} = 30 mM, blue), (b) 2:1 (C_{total} = 30 mM, red). The grey crosses are normalized electron echo intensities as a function of τ_D, and the solid and dotted lines are the two-component fitting curve for ν_{probe} set at Trityl (193.6 GHz) and TEMPO (193.9 GHz) center frequencies, respectively.

ν_{probe} set to the center frequencies of the Trityl (figure 3.1 solid lines) and TEMPO (figure 3.1 dotted lines) radicals. We make two major observations: (i) with the same total spin concentration, T_{1e} measured at Trityl and TEMPO frequencies barely changed with the radical compositions; (ii) T_{1e} of Trityl was significantly shorter than that of TEMPO for both ratios. In the 1:1 ratio, the average T_{1e} values were 32.7±3.6 ms and 54.8±9.2 ms for Trityl and TEMPO, respectively. This is unexpected, and suggests that the benefit for DNP of mixing Trityl with TEMPO does not come from more facile saturability of the Trityl resonance under these condition. Fitted T_{1e} are recorded in table 3.1, where T_{1e} are calculated as (A*$T_{1e-slow}$+B*$T_{1e-fast}$)/(A+B).

Table 3.1: Simulated T_{1e}

TEMPO:Trityl (C_{total} mM)	ν_{probe} (GHz)	$T_{1e-slow}$ (ms)	A	$T_{1e-fast}$ (ms)	B	T_{1e} (ms)
1:1 (30)	193.6	58.0±3.4	0.418±0.01	1.4±0.1	0.339±0.01	32.7±3.6
1:1 (30)	193.9	103.3±8.8	0.432±0.02	3.4±0.4	0.407±0.01	54.8±9.2
2:1 (30)	193.6	48.0±2.4	0.411±0.01	1.8±0.1	0.374±0.01	26.0±2.6
2:1 (30)	193.9	87.8±5.3	0.476±0.01	2.5±0.3	0.345±0.01	52.0±5.6

3.3.2 Pump-probe ELDOR Experiment

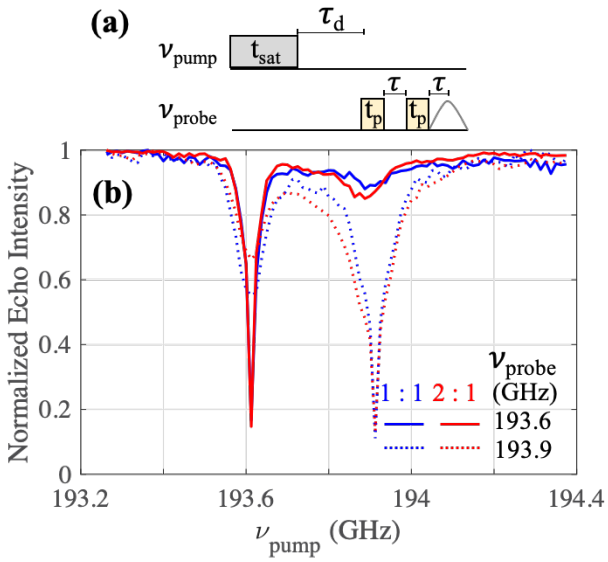

Figure 3.2: ELDOR experiments with a pulse scheme (a) were recorded at 4 K for mixed-radical systems (b) TEMPO:Trityl = 1:1 (blue) and 2:1 (red) with a total concentration of 30 mM. Solid and dotted lines correspond to ν_{probe} = 193.6 and 193.9 GHz, respectively. The amplitude for the 100 ms ν_{pump} is 120 mW.

Electron-electron double resonance (ELDOR) experiments delineate how e spin saturation at one frequency (ν_{pump}) is transferred to another frequency (ν_{probe}) across the EPR line. ELDOR profiles are shown in figure 3.2 for the 1:1 (blue) and 2:1 (red) ratios, where the solid and dotted lines correspond to ν_{probe} = 193.6 and 193.9 GHz, respectively. The ELDOR spectra of the two mixtures at ν_{probe} = 193.6 GHz display comparable eSD around the Trityl, indicating similar e spin dipolar coupling from clustering of Trityl in DNP Juice.[80] When ν_{probe} is set to 193.9 GHz, the ELDOR profile of the 2:1 sample exhibits greater eSD around the TEMPO ν_{pump} frequency than in the 1:1 sample, indicating the eSD among TEMPO has increased. Meanwhile, for ν_{probe} = 193.9 GHz, smaller eSD is observed in the 2:1 mixture when the ν_{pump} is set around the Trityl frequency, which can be explained by the relatively lower spin density of Trityl. Taken together, the ELDOR data analysis suggests that the benefit of the 2:1 mixture mainly comes

from a higher number density of CE-fulfilling spins, as properties of spin dynamics and saturation appear rather comparable for the two ratios.

3.3.3 Static ^{1}H DNP Experiments

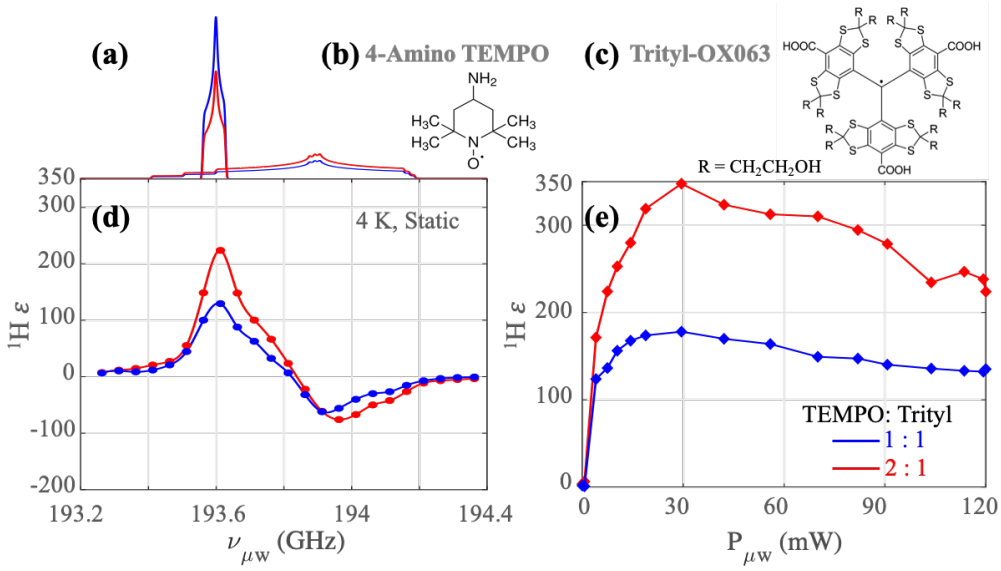

Figure 3.3: Mixed-radical with a total concentration C_{total} = 30 mM, TEMPO:Trityl = 1:1 (blue) and 2:1 (red). (a) Simulated EPR spectra at 6.9 T. Chemical structures of (b) 4-Amino TEMPO and (c) Trityl-OX063. (d) Experimental ^{1}Hε vs. $\nu_{\mu w}$ at static condition, 4 K measured with solid-echo detected ^{1}H signal in DNP Juice and $P_{\mu w}$ = 120 mW, $t_{buildup}$ = 60 s. (e) ^{1}Hε vs $P_{\mu w}$ obtained at optimum $\nu_{\mu w}$ = 193.6 GHz.

Mixtures with 1:1 and 2:1 TEMPO:Trityl ratios, respectively, with a total concentration of 30 mM in DNP Juice (60/30/10 vol% d_8-glycerol/D_2O/H_2O) were chosen to commence the study. The simulated EPR spectra of the two mixtures are shown in figure 3.3(a). The Trityl and TEMPO center frequencies are separated by roughly the ^{1}H Larmor frequency, while the electron spin density is concentrated at the Trityl resonance. However, whether or not the DNP enhancement (ε) will be boosted by electron spin density matching of the mixed radicals cannot be inferred from the EPR spectra,

given the role of electron spin relaxation, electron-electron coupling and electron spectral diffusion (eSD) in modulating DNP. Here, we empirically examined the effect of electron spin density matching using our DNP setup.

The DNP frequency profiles ($^1H\varepsilon$ vs. $\nu_{\mu w}$) of the radical mixtures with 1:1 and 2:1 ratio for TEMPO:Trityl, with a total e spin concentration (C_{total}) fixed to 30 mM, were recorded at 4 K from the ratio of the integrated solid-echo ^{1}H NMR signal at μw-on and μw-off, as displayed in figure 3.3(d). The positive maximum enhancement, ε^+, is obtained at $\nu_{\mu w}$ = 193.6 GHz for both mixtures, and the negative maximum enhancement, ε^-, at 193.9 and 194 GHz for 1:1 and 2:1, respectively. The absolute value for ε^- is significantly lower than ε^+ in both cases. The overlaid profiles show that the 2:1 mixture yields 72% greater enhancements, with ε^+ = 224 for the 2:1 mixture compared to ε^+ = 130 for the 1:1 mixture with 120 mW μw power ($P_{\mu w}$) irradiation for 60 s. To investigate the $P_{\mu w}$ dependence on DNP, $^1H\varepsilon^+$ values were obtained as a function of $P_{\mu w}$ at the optimum frequency of $\nu_{\mu w}$ = 193.6 GHz. The power profiles showed (figure 3.3(e)) an increase, followed by a decrease in ε with increasing $P_{\mu w}$ beyond an optimum threshold value. This is attributed to *oversaturation*, an effect originating from beyond optimum e spin depolarization caused by eSD.[54] Notice that under the applied DNP conditions, we readily reach the maximum ε with a low $P_{\mu w}$ of ∼30 mW, making the mixed-radical system particularly beneficial for DNP under μw power-limited conditions. At the optimum $\nu_{\mu w}$ and $P_{\mu w}$, the 2:1 mixture yields greater ε of 347, which is 95% larger than that of the 1:1 mixture. The electron spin dynamics, probed using T_{1e} (figure 3.1) and ELDOR measurement (figure 3.2) at the DNP conditions, suggests that the benefit of the 2:1 mixture mainly comes from a higher number density of CE-fulfilling spins overall, as properties of spin dynamics and saturation appear rather comparable for the two ratios under static conditions. EPR measurement also revealed that the T_{1e} at the

Trityl resonance is shorter compared to that at the TEMPO resonance, perhaps due to the clustering of Trityl in DNP Juice. This shows that the increased DNP efficiency of mixed radical radical can not attributed to slow relaxation of Trityl, but rather to its narrower line.

The vital question is whether the benefit of the 2:1 over the 1:1 mixture will be maintained under MAS, where the CE mechanism is principally different from static conditions due to energy oscillations of the relevant spin states.[55, 56] The energy oscillations, mainly originating from the large g-anisotropy, typically increase the combinations of spin pairs fulfilling the CE conditions. Since the g-anisotropy of Trityl is very small compared to TEMPO, the effective number of CE resonances per rotor period (τ_r) is not limited by Trityl but by TEMPO, and depends heavily on TEMPO's g-tensor orientation. Thus, the multi-spin effect under MAS is considerably more complex, and optimizing the mixed-radical composition is critical to maximize its CE DNP.

3.3.4 MAS ^{1}H DNP experiments

The investigation of mixed-radicals under MAS were carried out at 6.9 T, using a custom MAS probe (Revolution NMR, LLC.)[45] operational at 25 K and powered by a 350 mW μw source. The DNP frequency profiles, as obtained by ^{1}H-^{13}C Cross Polarization (CP) under 3 kHz MAS measured with 2-^{13}C glycine (to avoid background signal from the MAS system), are shown in figure 3.4(a). The $\varepsilon_{on/off}$ enhancements are determined from the ratio of the integrated μw-on and μw-off NMR signal. Overall, the frequency profiles under MAS were found to be similar in appearance to those obtained under static condition. The MAS DNP profile of AMUPol in DNP Juice, acquired under

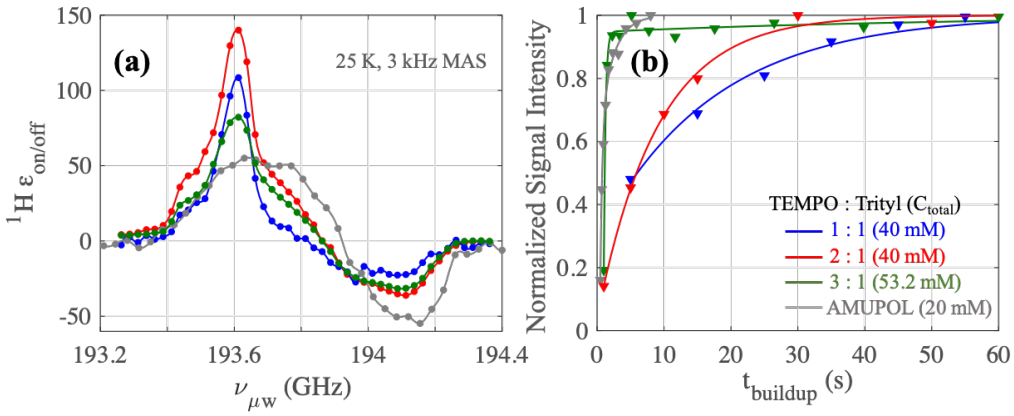

Figure 3.4: (a) Experimental ^{1}Hε vs. $\nu_{\mu w}$ at 3 kHz MAS, 25 K for TEMPO:Trityl = 1:1 (C_{total} = 40 mM, blue), 2:1 (C_{total} = 40 mM, red), and 3:1 (C_{total} = 53.2 mM, green), and C_{total} = 20 mM AMUPol in DNP Juice, measured using 2-^{13}C glycine through ^{1}H-^{13}C CP experiment. $P_{\mu w}$ = 350 mW and t$_{buildup}$ = 60 s. (b) DNP buildup at optimum $\nu_{\mu w}$.

the same conditions, is overlaid in grey, for comparison. At the optimum $\nu_{\mu w}$, the 2:1 mixture leads to a 28% greater $\varepsilon_{on/off}$ than the 1:1 mixture at the same C_{total} = 40 mM. The $\varepsilon^+_{on/off}$ observed for 1:1 and 2:1 are 109 and 140, respectively. This is a phenomenal result, considering the relatively low $P_{\mu w}$ = 350 mW at the source output available for our DNP setup. We also tested the 3:1 mixture with C_{total} = 53.2 mM. This resulted in a decreased $\varepsilon^+_{on/off}$ = 82, which may be due to faster T$_{1e}$ relaxation with increased spin concentration. Impressively, $\varepsilon^+_{on/off}$ of the 1:1, 2:1 and 3:1 mixtures were all higher than of AMUPol at an optimum C_{total} = 20 mM ($\varepsilon^+_{on/off}$ = 55).[72, 76] The lower $\varepsilon^+_{on/off}$ observed with AMUPol is due to high μw power requirement for bis-nitroxides.[1, 76] The mixed TEMPO-Trityl radical has also been shown to exhibit minimal ^{1}H depolarization [58, 81] under MAS in contrast to AMUPol.[45] Hence, the absolute ^{1}H enhancement for AMUPol will be even lower if its large depolarization factor at MAS exceeding 1.5 kHz is considered, as reported in the literature. [45]

The steady state DNP buildup time (T$_{buildup}$) shows a marked decrease as the TEMPO:

Trityl ratio is increased in the mixture (figure 3.4(b)). In fact, $T_{buildup}$ (5 s) for untethered 3:1 mixture is slightly shorter than that of AMUPol (8 s), where the two e spins are strongly coupled within the tethered biradical. It is anticipated that chemically tethering two or three nitroxide moieties to Trityl will significantly boost ε and shorten the $T_{buildup}$ time.

3.4 Numerical Simulation

However, unlike tethered mixed radical systems, the physical mixtures cannot maintain a radical distribution where one Trityl radical is strongly coupled to one/two tethered TEMPO radicals. To further examine if increasing the TEMPO composition as well as tethering can be beneficial, quantum mechanical simulations of DNP-NMR were performed using the Spin Evolution package.[82] The Spin-Evolution package allows DNP simulation for solid samples with powder averaging in Liouville space, and therefore can also incorporate relaxation into account. The simulations were performed for $e_1 - e_2 - {}^1\mathrm{H}$ and $e_1 - e_2 - e_3 - {}^1\mathrm{H}$ spin system, with e_1 representing a narrow-line Trityl radical, and e_2 and e_3 representing broad-line TEMPO radicals. The principal axis components of the g-tensors of the electron spins were taken the same as in table 3.2. The g-tensor of e_2 and e_3 were related to e_1 by the Euler angles sets, (30,10,0) and (50,70,0), respectively. The relative e_1-e_2 and e_1-e_3 dipolar tensor orientation were given by the angles (20,60,30) and (50,90,60), respectively. The orientation of the dominant $e_1 - {}^1\mathrm{H}$ hyperfine coupling was chosen to be (40,10,0). The relaxation rates, ^{1}H T_1, T_{1e_1}, and $T_{1e_{2/3}}$, are set to 4 s, 4 ms, and 3 ms respectively, unless mentioned otherwise.

We simulated CE DNP at 6.9 T, under 10 kHz MAS and a μw B_1 of 0.2 MHz for a

Table 3.2: g and A anisotropy

Radical	g_x	g_y	g_z	A_x MHz	A_y MHz	A_z MHz
TEMPO	2.009	2.006	2.0021	16	15	95
Trityl	2.0034	2.0031	2.0027	0	0	0

1:1 ($e_1 - e_2 - {}^1$H) and 2:1 ($e_1 - e_2 - e_3 - {}^1$H) type radical system, with e_1 representing a Trityl and e_2 and e_3 representing TEMPO moieties. In both cases, we fixed the e_1-e_2 and e_1-^{1}H dipolar couplings to 6 and 2 MHz, respectively. Only the e_1-e_3 dipolar couplings were varied, while keeping its relative orientations fixed. All the other dipolar couplings were turned off for simplicity, including the e_2-e_3 dipolar coupling from TEMPO-TEMPO interaction.

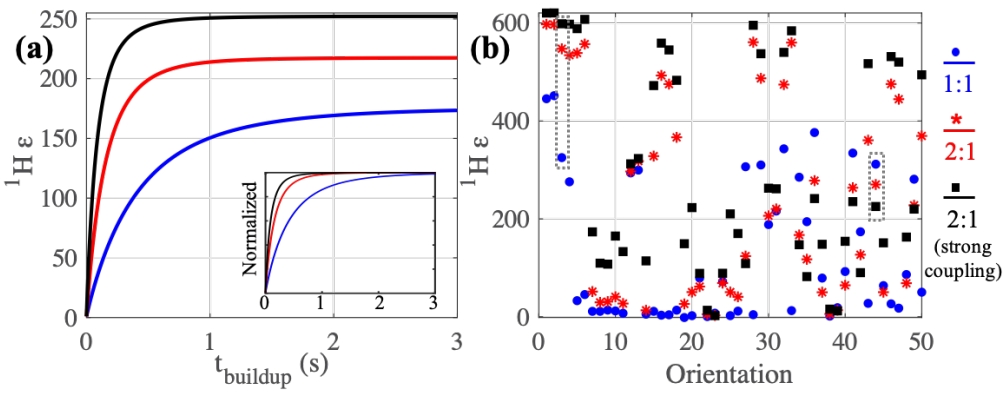

Figure 3.5: (a)Simulated ^{1}Hε for $e_1 - e_2 - {}^1$H (blue) and $e_1 - e_2 - e_3 - {}^1$H (red and black) spin systems for 232 powder orientations, at 6.9 T, 10 kHz MAS and 0.2 MHz $P_{\mu w}$. e_1 mimics Trityl, and e_2 and e_3 mimic TEMPO. $e_1 - e_3$ dipolar coupling is set to 6 and 12 MHz, in red and black curve, respectively. $T_{1}{}_H$ and T_{1e} were set to 4 s and 3 ms, respectively. Inset shows normalized ^{1}Hε. (b) ^{1}Hε mapped for 50 different orientations.

The aim of the simulation was to ask: (i) can the CE between Trityl and TEMPO radicals be increased by increasing the relative number density of the TEMPO, and (ii) will increased e-e coupling by chemical tethering further improve CE for the 2:1 mixture? The simulated ^{1}Hε as a function of μw irradiation time ($T_{buildup}$) with $\nu_{\mu w}$ fixed to the

Trityl center frequency is shown in figure 3.5(a). Remarkably, the net $^1H\varepsilon$ increased by $\sim$26% by merely changing the radical type from 1:1 (blue line, $^1H\varepsilon = 173$) to 2:1 (red line, $^1H\varepsilon = 217$) with $t_{buildup} = 3$ s (steady state), corroborating the experimental observations of the physical mixture. The $^1H\varepsilon$ and the buildup rates could be further augmented by increasing the coupling strength, as observed when e_1-e_3 coupling is increased from 6 MHz (20Å) in red to 12 MHz (16Å) in black. This observation confirms that the increased proportionality of TEMPO with respect to Trityl will be even more advantageous when these radicals are chemically tethered. This is because optimally increasing the e-e coupling strength increases the CE transition probability, while also maintaining a large steady state polarization difference between the e spins as a result of adiabatic e-e polarization exchange, resulting in higher CE enhancement. Here, we want to assert that the design principle introduced here may not work for oligomeric nitroxide-radical due to its more stringent orientation dependence or selectivity. For instance, for the same simulation parameters, replacing the narrower e_1 (Trityl) with a broad line (TEMPO) radical abates the DNP enhancement for $e_1 - e_2 - e_3 - ^1H$ compared to $e_1 - e_2 - ^1H$.

In figure 3.5(b), we show steady state $^1H\varepsilon$ for 50 different orientations in powder for the same parameters as used in figure 3.5(a). We observe that $^1H\varepsilon$ increased statistically for most orientations at 2:1 ratio (red and black) and with stronger coupling (black). In other words, for the majority of e spin pairs, the CE between e_1-e_2 and e_1-e_3 constructively adds up, shifting the net enhancement and buildup rate to much higher values. This result makes sense as the CE resonance conditions between the broad and narrow radical are determined/limited by the orientation of the broad line radical. Therefore, increasing the broad line proportionality increases the net effective CE frequency per τ_r. We can conclude that the gain in both $^1H\varepsilon$ and buildup rates are due to increased probability for CE between Trityl and the TEMPO radicals. Note that in the simulation, the

mechanistic prerequisites for TEMPO-TEMPO CE are turned off (no e_2-e_3 coupling). In other words, for low-power μw source, the benefit from the 2:1 ratio is not primarily due to indirect effects coming from increased TEMPO-TEMPO couplings, while such effects are certainly present additionally under experimental conditions. The SE mechanism is also eliminated since ^{1}H is hyperfine coupled only to the narrow line e_1 spin and the μw irradiation is on-resonance with e_1. Turning on more couplings, such as between e_2-e_3, e_2-^{1}H and e_3-^{1}H can further increase the net DNP enhancement.

3.5 Conclusion

Taken together, we demonstrated that tuning the e spin density by simply altering the ratio of mixed broad and narrow line radical dramatically enhanced the CE DNP performance, under both static and MAS conditions. Surprisingly, even a simple physical mixture between TEMPO and Trityl, when the e spin density is matched without chemical tethering, can outperform the broadly used AMUPol biradical when relying on low-power μw solid-state diode sources that is becoming increasingly popular owing to its low cost and μw versatility, as well as pulsing capability.[78, 79] A very recent joint venture by Bruker Biospin and Virginia diodes has shown that a 250 mW solid-state source with optimized μw transmittance can lead to an impressive enhancement of $\sim$61 at 9.4 T, 100 K and 8 kHz spinning.[83]

In summary, this study reveals a new design principle for next generation PAs targeting greater CE DNP enhancement factors and DNP buildup rates. Quantum mechanical simulations elucidated that a single narrow line radical can constructively perform CE polarization transfer with multiple coupled broad line radical partners under MAS. While

our present study was carried out with a physical mixture, we expect tethered TEMPO-Trityl systems with a higher than 1:1 TEMPO:Trityl ratio to further and dramatically enhance CE DNP under static and MAS conditions.

Chapter 4

Truncated Cross Effect DNP: An Overhauser Effect Doppelgänger

Reprinted with permission from Equbal, A., Li, Y., Leavesley, A., Huang, S., Rajca, S., Rajca, A., & Han, S. (2018). Truncated cross effect dynamic nuclear polarization: an overhauser effect doppelganger. *The journal of physical chemistry letters*, 9(9), 2175-2180.

4.1 Introduction

An important focus in DNP has been on optimizing the paramagnetic polarizing agent (PA) and solvent to yield maximum DNP enhancements under different mechanisms.[84, 85, **?**, 86, 87, 25, 44, 88, 30] However, a rational understanding of the effect of the radical or radicals mixture, solvent, temperature, and magnetic fields on the DNP efficiency and mechanism is still elusive. The Solid Effect (SE) and Cross Effect (CE) are the most prominent DNP mechanisms in non-conducting solid-state samples. In contrast, the Overhauser Effect (OE) mechanism has been thought to be relevant only in

conducting-solids or liquids, where electron spin-diffusion and molecular-tumbling motion can provide rapidly fluctuating hyperfine-couplings, causing efficient $e - n$ Zero Quantum (ZQ) or Double Quantum (DQ) cross-relaxation.[89, 90] However, contrary to expectations, Can *et al.* [91] recently reported on an unexpected observation of OE with the non-conducting, narrow-line, polarizing-agent, 1,3-bisdiphenylene-2-phenylallyl (BDPA) [92] dispersed in polystyrene and with sulfonated-BDPA (SA-BDPA) [93] in a glassy d_8-glycerol/D_2O/H_2O (6:3:1, v/v/v) matrix termed DNP Juice, at ∼100K and at magnetic fields between 5 and 18.8 T. This discovery of OE in insulating-solids is considered pivotal for the prospect of DNP in high magnetic fields, owing to the low μw-power requirement of OE and the potential field-independent DNP efficiency. However, the underlying relaxation mechanism in insulating solids is unknown, and therefore the mechanistic basis for the OE in insulating solids is inconclusive. This makes the discovery of OE in insulating-solids by Can *et al.* unexpected and exciting. Even more curiously, reports of OE-DNP mechanism in non-conducting SA-BDPA have been made by Bodenhausen and coworkers at temperatures as low as 1.2 K under static conditions and at 6.7 T, [94] while there is no obvious physical basis for the occurrence of fast $e - n$ fluctuations near the electron Larmor frequency under these experimental conditions. Recent work by Pylaeva *et al.* [95] discusses possible mechanisms for the observed OE in BDPA on the basis of molecular dynamics and spin dynamics simulations, but a rigorous experimental proof does not exist to date.

Counter to the proposed theory [95] and our own expectations, we observed very similar strong OE features with Trityl-OX063 (OX063) when doped with equivalent amounts of tetracarboxylat*e*-*e*ster-pyrroline (TCP) nitroxide radicals[**?**], a nitroxide radical that possesses electron withdrawing, gem-dicarboxylate ester substitutes, across a wide range of temperatures in DNP Juice. This intriguing discovery further showed that varying

the solvent from DNP Juice to DMSO changed not only the DNP efficiency, but also the apparent DNP mechanism from OE to CE in hitherto unknown ways.

This chapter reports on a series of experiments and quantum mechanical calculations of the DNP mechanism that yield a rationale basis for the apparent OE observed with OX063-TCP mixtures in DNP Juice. It is important to note here that we do not intend to experimentally validate the mechanistic basis of OE in BDPA in this chapter since its reported experimental conditions[91, 94, 96] are very different from ours.

4.2 Experimental Methods

4.2.1 Pulse Sequence

The pulse schematic for acquisition of the ^{1}H NMR signal under μw -on and -off conditions is shown in figure 4.1(a). The relaxation rates of electrons were measured by calculating the electron signal recovery rate after saturation, using the pulse schematic shown in figure 4.1(b). Electron-electron double resonance (ELDOR) measurements were acquired using two separate μw channels: (i) pump/saturation of electrons at one frequency and (ii) probe/detection of electrons at another frequency, as shown in figure 4.1(c). In the ELDOR experiments, the pump frequency was scanned while the probe frequency was held constant.

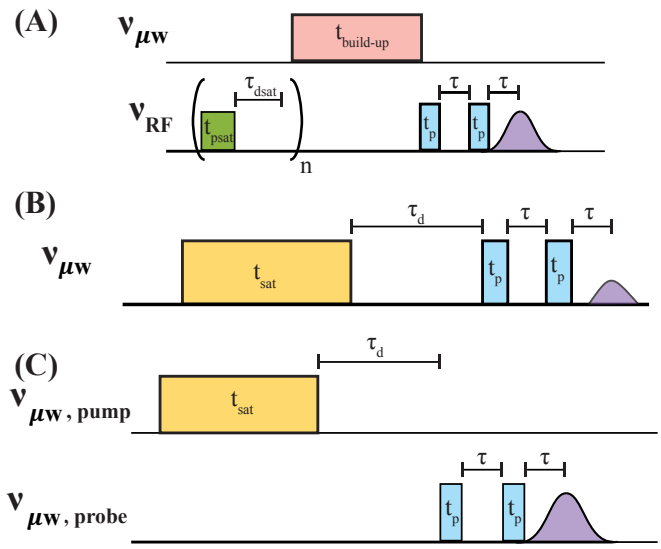

Figure 4.1: (a) Solid-echo experiment with pre-saturation pulses used for NMR experiments. Here, $t_{build-up}$ block shows μw irradiation and the two short pulses (t_p) represent solid-echo pulses. (b) Saturation-recovery scheme to measure electron relaxation rate. The yellow block represents the electron saturation pulse and the short t_p represent echo pulses for EPR detection. The recovery time, τ_d is changed here. (c) Two channels ELDOR pulse schematic. The $\nu_{\mu w,pump}$ channel is to pump or saturate an electron with pulse duration (t_{sat}), shown in yellow block. The $\nu_{\mu w,probe}$ channel is to probe or detect electron using sold echo pulses, shown in blue.

4.2.2 Sample

The nitroxide radicals studied here possess gem-dicarboxylate ester substituents within the prollyl ring structure, referred to as tetracarboxylate prollyl (having two forms, TCP1 and TCP2) nitroxides (figure 4.2(a)).[97] 50 μL of these radical solutions were used for each measurement. TCP molecules were synthesized in search of a new spin label for DEER experiments. Here, the methyl groups are designed to be far away from N-O· (nitroxide). This leads to slower relaxation (especially, T_m) at higher temperatures, above 70 K. TCP1 and TCP2 showed similar EPR and DNP features (will discuss in the following sections), and so for this reason all experimental comparisons presented here were conducted using TCP2. The electrochemistry of these exotic radicals has been explored recently in acetonitrile solvent, showing relatively low (less negative) reduction

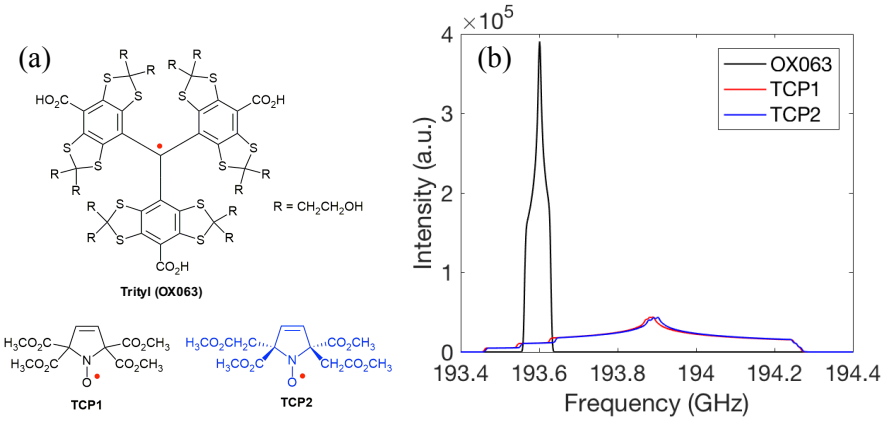

Figure 4.2: (a) Chemical structures of Trityl-OX063, TCP1, and TCP2. (b) Simulated EPR spectra of OX063, TCP1 and TCP2, where the g-tensors of the electrons were taken as: OX063 g_x=2.0034, g_y=2.0031, g_z=2.0027; TCP1 g_x=2.0099, g_y=2.0060, g_z=2.0025; and TCP2 g_x=2.0099, g_y=2.0061, g_z=2.0026. EasySpin has been used for simulation.

potentials.[98] However, our focus here was to exploit the DNP capability of this radical in the most commonly used solvents: DMSO/water and glycerol/water. Different concentrations of tetracarboxylate ester pyrroline nitroxides (TCP2) radicals were added to 15 mM Trityl-OX063 (GE Healthcare AC) in two standard glassing solvents: (a) DMSO which was d_6-DMSO (Cambridge Isotopes), D_2O (Cambridge Isotopes), and H_2O in the ratio 78:14:8, by % *weight*, and (b) DNP Juice which was d_8-glycerol (Cambridge Isotopes), D_2O, H_2O mixture in the ratio 6:3:1, by % *volume*. The total proton concentration in DMSO and DNP Juice were kept constant to ensure similar spin diffusion rates in the two different glassing agents. Notably, TCP2 showed high solubility ($\sim$ 30 mM) in DMSO, but its solubility in DNP Juice was poor ($<<$ 5 mM). However, in the presence of OX063, TCP2's solubility increased significantly ($\sim$ 60 mM) in DNP Juice, suggesting that the electron deficient TCP2 interacts or associates with the electron rich OX063. The Easyspin-simulated[99] EPR spectra of TCP and Trityl are shown in figure 4.2(b).

4.3 Results and Discussion

4.3.1 ^{1}H DNP μw Frequency Profile

The DNP frequency-profile is indicative of the underlying DNP mechanism and the optimum conditions.[1, 100, 101, 102, 47] Figure 4.3(a) shows the DNP frequency-profile of a mixture containing 15 mM TCP2 and 15 mM OX063 in DNP Juice at 4 K. Significant ^{1}H DNP enhancements were observed at the μw irradiation frequencies of ∼193.3 GHZ, ∼193.6 GHz and ∼193.9 GHz. Clearly, the enhancements at 193.3 GHz and 193.9 GHz are ±300 MHz apart from the OX063 center-frequency, and correspond to conditions for SE_{ZQ} and SE_{DQ} DNP, respectively. The enhancement at 193.6 GHz was *a priori* assigned to OE as it corresponds to OX063′s center-frequency at 6.9 T. Observing OE around this frequency was not only unexpected, but also initially inexplicable, and therefore will be dubbed as OE* (till the time it's actual origin is proven later), with the * denoting an apparent OE. Surprisingly, no visible features of DNP resulting from TCP2 in DNP Juice appeared in the observed frequency-profile.

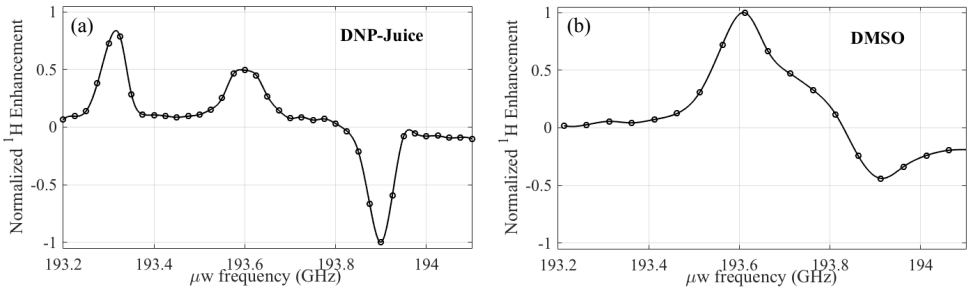

Figure 4.3: DNP frequency profiles of 15 mM TCP2 - 15 mM OX063 mixture at 4 K in (a) DNP Juice; (b) DMSO. DNP frequency-profiles were obtained by measuring ^{1}H DNP signal enhancement as a function of μw irradiation frequency which was swept from 193.2 GHz to 194.1 GHz, with 120 mW μw-power and 60 s irradiation time. The ^{1}H enhancements displayed were normalized by the maximum absolute value.

The DNP frequency-profile was also measured for the same OX063-TCP2 mixture in

DMSO. Adding to the OE* conundrum, the frequency-profile in DMSO displayed a diametrically different frequency envelope compared to DNP Juice, revealing a dominant CE mechanism. The positive and negative maximum enhancements were observed at ∼193.6 GHz and ∼193.9 GHz, respectively (figure 4.3(b)). The separation of these maximum peak positions by 300 MHz is consistent with CE between OX063 and TCP2, while the broader features are presumably due to CE between two TCP2 radicals, where a range of electron spin pairs at different μw-frequencies fulfill the CE conditions. The presence of the OE* mechanism in DMSO cannot be ruled out, since the optimum frequency for the OE* (in DNP Juice) coincides with the peak resulting from TCP2-OX063 CE. At 193.6 GHz (optimum for OE*), enhancements (NMR signal intensity ratio: μw-power on/off) of ∼31 was observed for TCP2-OX063 in DNP Juice and ∼139 in DMSO, both at 4 K with 120 mW μw-power and 60-s irradiation.

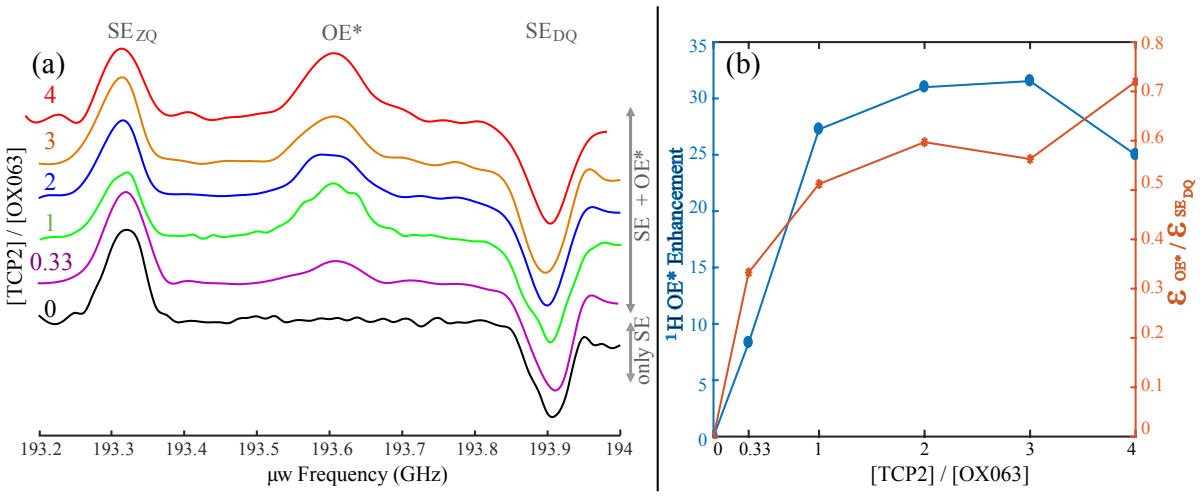

Figure 4.4: (a)TCP2:OX063 ratio optimization for maximum OE* enhancement at 4 K in DNP Juice using: 60 s μw irradiation time and 120 mW μw-power. OX063 concentration was fixed to 15 mM. All the profiles are normalized to the corresponding SE_{DQ} enhancement number. (b) Absolute OE* enhancement is plotted on the left y-axis and $\varepsilon_{OE*}/\varepsilon_{SE_{DQ}}$ ratio is plotted on the right y-axis for different radical concentrations.

Next, the radical mixture composition was investigated to achieve optimum OE* en-

hancements in DNP Juice (at 4 K, 120 mW μw-power, 60-s μw-irradiation). The DNP frequency-profile of a series of TCP2/OX063 mixtures were recorded, where the OX063 concentration was fixed at 15 mM and the TCP2 concentration varied from 0 to 60 mM (figure 4.4(a)). All frequency-profiles were normalized with the optimum SE_{DQ} enhancement. The DNP frequency-profiles show OE* enhancements only with TCP2 doping, in addition to SE enhancements at 193.3 and 193.9 GHz. The absolute OE* enhancement and its relative efficiency with respect to SE_{DQ}, $\varepsilon_{OE^*}/\varepsilon_{SE_{DQ}}$, are plotted in figure 4.4(b). They show that an increase in the TCP2 concentration leads to an increase in the OE* enhancement up to 30 mM, after which it plateaus with increasing TCP2 concentration (and slightly decreases at 60 mM). For all the following investigations, the radical composition was fixed to the optimum composition of 15 mM OX063 and 30 mM TCP2.

4.3.2 Temperature Dependence

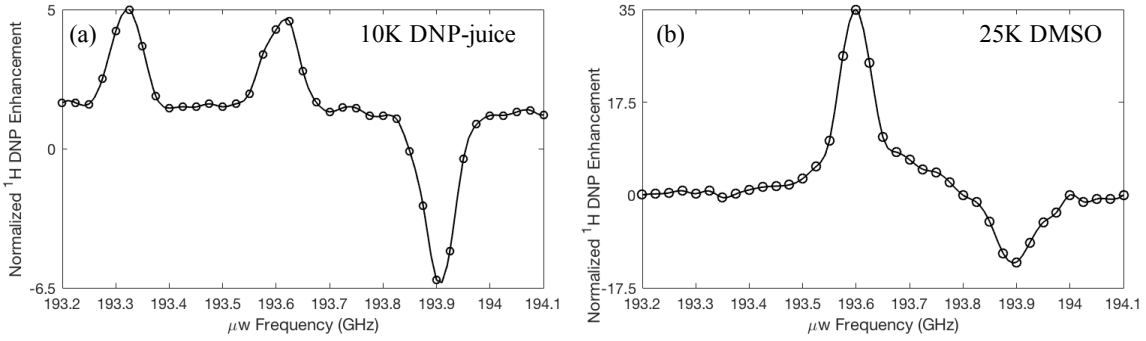

Figure 4.5: Frequency-profile of 20 mM TCP2 15 mM OX063 in (a) DNP Juice at 10 K and (b) DMSO at 25 K with 120 mW μw power and 60 s irradiation time.

To verify the temperature dependence of the underlying DNP mechanism, DNP frequency-profile and power-profile measurements were acquired at higher temperatures. It was found that the overall frequency-profile envelope remains similar, independent of the temperature. The OX063-TCP2 mixture in DNP Juice continues to show the SE

and OE* features, while the same OX063-TCP2 mixture in the DMSO solvent reveals the CE to be the predominant DNP mechanism. The frequency-profiles of OX063-TCP2 mixtures in DNP Juice acquired at 10 K and DMSO acquired at 25 K are shown in figure 4.5. Clearly, the profiles at 25 K are very similar to the ones recorded at 4 K for both the solvents. The temperature dependence of the OE* DNP enhancements was evaluated between 3.3 K and 85 K with the μw conditions: 193.6 GHz irradiation frequency, 120 mW μw power, and 60 s buildup time (see figure 4.6). Above 10 K, OE* enhancements decreased gradually with increasing temperatures, but below 10 K the dependence of enhancement on temperature was found to be more dramatic. Notably, when the temperature was decreased from 4 K to 3.3 K, the OE* enhancements jumps from 31 to 145. To rationalize this sudden jump, we currently have an unproven hypothesis, which is: due to increase in OX063's T_m, the echo-detected μw-off NMR signal is significantly reduced at 3.3 K compared to 4 K, owing to removal of self decoupling from the nearly 100% polarized electron spins. However, under μw irradiation, the paramagnetic effect is repressed,[36] resulting in high apparent DNP signal enhancements, partially owing to the lowered μw-off signal. The full confirmation of this change in spin relaxation will have to be based on a full understanding of the electron spin relaxation mechanisms.

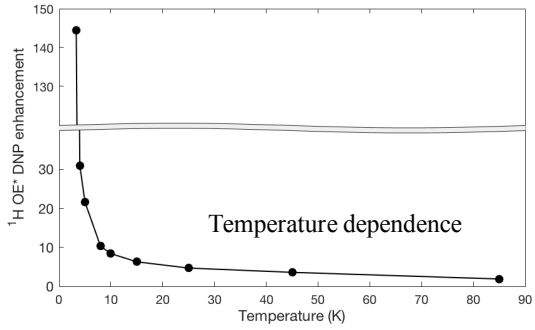

Figure 4.6: OE* DNP enhancement as a function of temperature of 30m M TCP2 15 mM OX063 DNP Juice mixture. Enhancement was calculated as the μw on signal intensity normalized by μw off signal intensity at the same temperature.

4.3.3 Scrutinizing the OE* DNP Observed with Trityl TCP Mixture

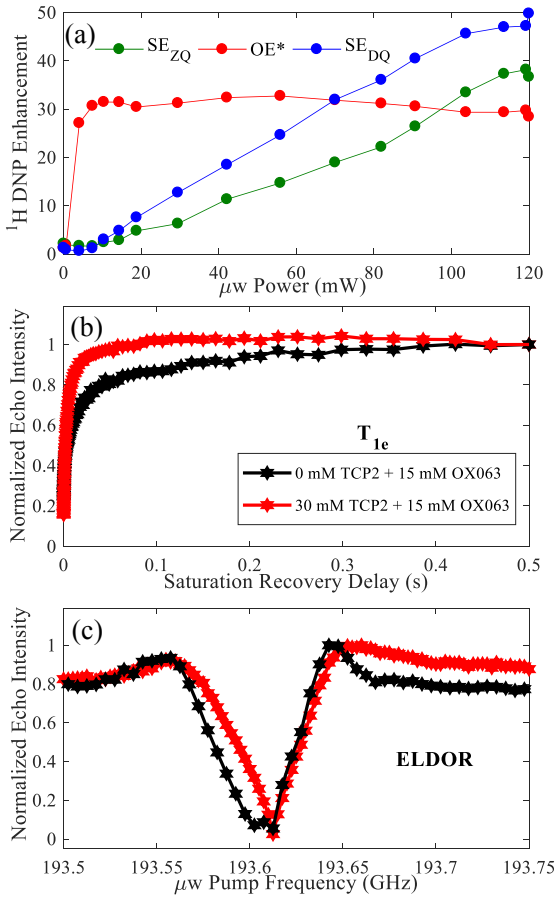

Figure 4.7: (a) DNP power saturation experiments of 15 mM OX063 30 mM TCP2 mixture in DNP Juice recorded at 4 K with μw-power varied from 0 to 120 mW and 60 s μw-irradiation. The μw-frequency was fixed at the optimum conditions for SE_{ZQ} (green), OE* (red) and SE_{DQ} (blue), respectively. (b) T_{1e} of pure OX063 (black) and TCP2-doped OX063 (red) at 4 K. (c) ELDOR of pure OX063 (black) and TCP2-doped OX063 (red) at 4 K.

The DNP power-curve (enhancement vs. μw-power) at the OE* frequency showed that the maximum enhancement (at 60 s μw-irradiation) was reached at merely 7 mW of μw-power, as shown in figure 4.7(a). Remarkably, 90% of the maximum enhancement was achieved with minuscule (4 mW) μw-power, further corroborating the signature proper-

ties of OE. In stark contrast, the optimum-power for SE-DNP enhancements could not be met by even 120 mW of μw-power. At low μw-power, the OE*-derived enhancement was higher by 16-fold compared to the SE-derived enhancements. At higher μw-power (>70 mW), the SE began to dominate over the OE* (at 4 K). Impressively, the low-power requirement to saturate the OE* resonance was observed even at higher temperatures of 10 and 25 K, and at low TCP2 concentrations (5 mM), indicating that the OE* effect is not power limited under the tested conditions (figure 4.8). The OE* phenomenon was observed across all the temperatures, from 3.3 to 85 K (figure 4.6). The temperature dependent DNP-measurement showed a sharp increase in OE* enhancement below 5 K, indicating the pivotal role of electron relaxation in the OE* phenomenon, given that its saturation can be ruled out as a limiting factor.

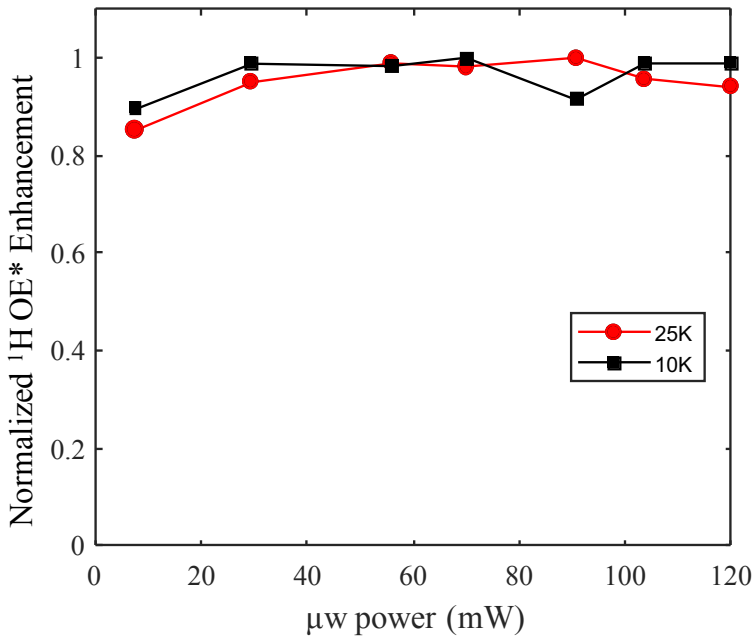

Figure 4.8: Power sweep at OE* center frequency (193.6 GHz) at 10 K (black) and 25 K (red). OE* ^{1}H enhancement was normalized by its maximum enhancement.

Scrutinizing the OE* discovery, we first compare our results with reported OE stud-

ies of BDPA in the literature. Can *et al.* attributed the absence of OE in OX063 and perdeuterated-BDPA (d_{21}-BDPA) to the absence of strong $e-H$ couplings. [91] In our case, OX063, all hydrogen atoms in the aromatic rings joined directly to the carbon radical center are purposefully substituted to remove the influence of large $e-H$ hyperfine-couplings.[85] The study by Pylaeva *et al.* [95] further proposed that fluctuations in the electron spin-density in BDPA results from conjugation in the carbon-radical position, leading to hyperfine-couplings fluctuations. Ji *et al.*[94] hypothesized that stochastic motions at low vibration frequencies can be a source of non-zero spectral-density at the electron resonance frequency leading to cross-relaxation, effective at low temperatures. Hyperfine-coupling fluctuations due to conjugation would not be a plausible mechanism for OX063, as its radical-center is fixed. Therefore, OX063 does not meet any of the hypothesized requirements (strong $e-n$ coupling and conjugation) for exhibiting OE in the pure or doped-state. Equally peculiar is our observation that OE* is turned on/off with the choice of the glassing solvent. Although the results duplicate the apparent properties of OE-DNP observed in insulating-solids, it does not meet the proposed theoretical basis.

Solving this OE* riddle requires scrutiny of the electron spin dynamics. This was enabled with unique instrumentation, which allowed for EPR measurements, polarization-profile, and electron-relaxation times under the relevant DNP conditions.[103] The echo-detected T_{1e} relaxation rates were measured at the frequencies corresponding to OE* and SE transitions. The T_{1e} of pure OX063 in DNP Juice was found to be ∼16 ms, which shortened to ∼4 ms upon addition of 30 mM TCP2 (figure 4.7(b)). Crucially, the T_{1e} of TCP2 in DNP Juice was too short to be detected which was also attributed to very short T_m, while T_{1e} of TCP2 in DMSO was significantly longer (∼17 ms). This hints at clustering[104, 105] of TCP2 in DNP Juice. That the T_{1e} of OX063 and/or nitroxide radicals are so critically solvent and mixture-dependent was unexpected, showcasing the

need to evaluate T_{1e} at the precise experimental DNP conditions. Tabulated T_{1e} values and further discussions on T_{1e} with respect to literature can be found in the later subsection.

Further insight was gained with electron-electron double resonance (ELDOR) that measures how EPR saturation or polarization at one frequency is transferred to another frequency. In the ELDOR-profile shown in figure 4.7(c), the electron detection/probe frequency was set to that of the OX063 center, and the saturating/pump frequency was scanned from 193.5 to 193.75 GHz with 120 mW power at 4 K. The ELDOR-profile showed that μw-irradiation resonant with TCP2 did not affect the OX063 resonance. This is consistent with the very fast relaxation of TCP2 in DNP Juice, which prevents it saturation by μw. Also, the hole burnt at the OX063 frequency narrows upon addition of TCP2, consistent with the shortening of OX063's T_{1e} upon doping with TCP2, especially with clustered TCP2 in DNP Juice.

4.3.4 Clustering of TCP in DNP Juice

The clustering of TCP2 radicals will shorten its electron relaxation rates, both T_{1e} and T_m, and make the Hanh-echo signal of TCP2 undetectable. T_{1e} and ELDOR experiments suggest the formation of TCP2 clusters as explained in the main text. This is verified by comparison of X-band continuous-wave electron paramagnetic resonance (CW-EPR) spectra of (a) 20mM TCP1 alone in DMSO (red), (b) 20mM TCP2 mixed with 15mM OX063 in DMSO (blue), and (c) 20mM TCP2 with 15mM OX063 in DNP Juice (black), shown in figure 4.3.4. All CW experiments were conducted at room temperature on a Bruker EMX X-band spectrometer, which has a center field of 0.35 T

and microwave-frequency of 9.8 GHz. 4 μL sample solution was packed in a 0.66 mm inner-diameter quartz capillary (VitroCom, Mountain Lakes, NJ) designed for EPR measurements. Clearly, in DMSO, the spectrum showed a superposition of TCP and OX063 CW-EPR spectra. However, the CW-EPR lines of OX063-TCP2 mixture in DNP Juice displayed dramatic line broadening, especially at the TCP2 resonance frequencies.

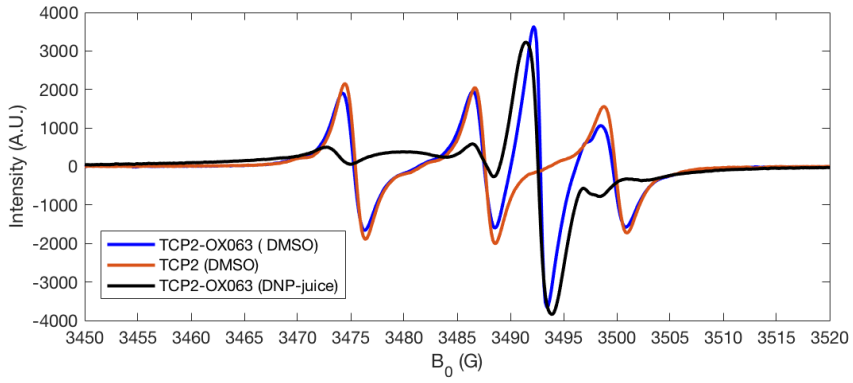

Figure 4.9: X-band CW-EPR spectrum of OX063-TCP2 mixture in DMSO (blue), DNP Juice (black) and TCP2 in DMSO (red). The concentrations of OX063 and TCP2 were fixed similar to the DNP conditions.

4.3.5 Electron Spin Relaxation Measurements

Figure 4.10 (a) and (b) show the intensity of the electron spin echo, observed at the OX063 centre frequency, as a function of magnetization recovery time, following a hard saturation pulse of 50 ms with 120 mW power for three TCP2 concentrations. The overlaid magnetization recovery curves for pure and TCP2-doped OX063 (detected at ~193.6 GHz) show the notable shortening of relaxation rate constant upon doping. While the longitudinal relaxation time constant, T_{1e} of pure OX063 in DNP Juice was long, ~16 ms, it was reduced to ~4 ms upon doping with TCP. No dramatic changes were observed upon changing the TCP2 doping concentration above 15 mM. We clarify here that it is

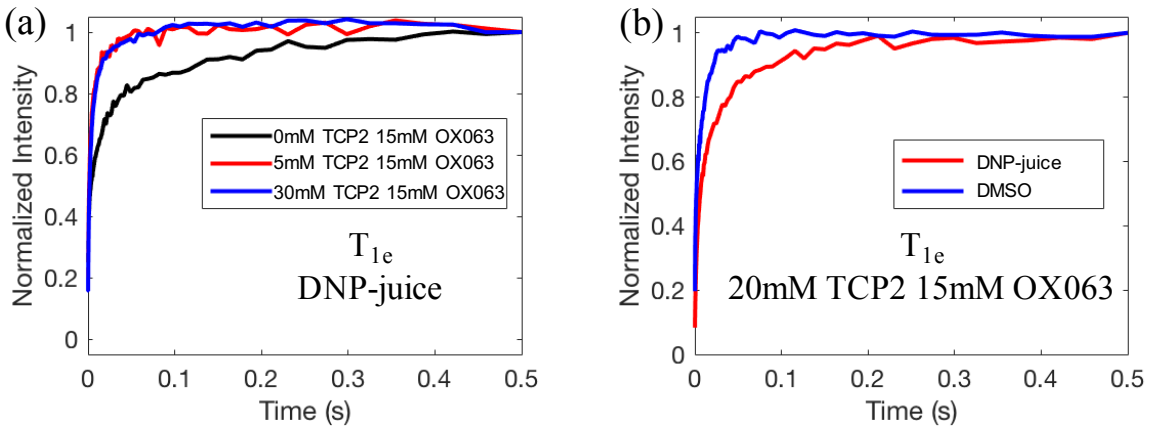

Figure 4.10: (a) T_{1e} experiments of pure OX063 (black), 5 mM TCP2 15 mM OX063 (red), 30 mM TCP2 15 mM OX063 mixtures in DNP Juice (blue). (b) 20 mM TCP2 15 mM OX063 mixtures in DNP Juice (red) and DMSO (blue). All the relaxation rates were measured at 193.6125 GHz, which is the center frequency of OX063.

misleading to fit the T_{1e} curve using either one or two exponential components because of radical clustering. Thus, the T_{1e} values are determined as the time when the recovered echo intensity reached 0.66 of the maximum (fully recovered) following its saturation. The T_{1e} relaxation rates measured in this study (at ~193.9 GHz) and available in the literature[6] for TCP2 are listed in table 4.1, showing that different experimental conditions have a marked effect on the observed T_{1e} values.

Solvent	**Concentration**	**B_0**	**Temperature**	**T_{1e}**
DNP Juice	15 mM	6.9 T	4 K	*
DMSO	15 mM	6.9 T	4 K	17 ms
Trehalose/Sucrose(9:1)[6]	0.1 mM	0.35 T	10 K	100 ms

Table 4.1: T_{1e}, relaxation rate for TCP2 in the presence of 15 mM OX063 in DNP Juice and DMSO/water. *Relaxation rate was very short, below detection limit and the corresponding T_m was also very short, below 0.85 μs and, therefore making the electron echo detection impossible on our instrument.

4.4 Numerical Simulation

Inspired by the observed EPR results, we quantum mechanically simulated the DNP frequency-profile for a narrow radical (e_1-OX063) and a broad radical (e_2-TCP2), unequally coupled to a proton in an $e_1 - e_2 - {}^1$H system. Mimicking the slow-fast relaxation rate combination observed in DNP Juice, T_{1e} of e_1 and e_2 were set to 4 and 0.01 ms, respectively. The DNP simulation was performed using SpinEvolution, a software package for spin dynamics simulations.[61] The SpinEvolution based numerical simulation shown here was performed using a 3-spin system, including 2 electrons and a nucleus, ^{1}H. The $e_1 - e_2$, e_1-H, and e_2-H couplings were taken to be 2, 3, and 0.087 MHz respectively. The principal axis components of the g-tensors of the electrons were taken as: OX063-e_1: g_x=2.0034, g_y=2.0031, g_z=2.0027, and TCP2-e_2: g_x=2.0099, g_y=2.0061, g_z=2.0026. The g-tensor of e_2 was randomly related to e_1 by a set of Euler angles, (0,45,90) and the relative e_1-e_2 dipolar tensor orientation was given by the angles (0,30,0). The orientation of the dominant e_1-n coupling was randomly chosen to be (0,10,90). The relaxation rates, T_{1H}, T_{1e_1}, and T_{1e_2} are set to 4 s, 4 ms, and 0.001 ms, respectively. The microwave irradiation power was fixed at 0.8 MHz for the DNP frequency-profile simulation. Economical power averaging with 100 orientation was used. To circumvent the need of including a very large powder orientations to cover all the possible orientations or the EPR resonances, a low 2.5 kHz spinning of the 100 crystallites was incorporated. Essentially, this will not change the frequency-profile, but rather make it more continuous.

Remarkably, we could replicate the experimental ^{1}H enhancement frequency-profile of the OX063-TCP2 mixture. A positive maximum enhancement is observed at the OX063 center-frequency, as well as ±300 MHz apart from the OX063 center, representing the SE_{ZQ} and SE_{DQ} conditions. Clearly, the OE* feature is observed, even though the

cross-relaxation mechanisms are turned off, i.e. the mechanistic prerequisites for OE are eliminated. This shows that the observed OE* is just a **truncated CE** (tCE) induced by conditions when one of the two electron spins involved in the CE has a very short T_{1e}. The CE relies on the selective saturation of one of the coupled electron spins. Thus, irradiation of the slower relaxing, "*easy to saturate*", electron spin (e_1) (193.6 GHz in figure 4.11(b)) will lead to an effective polarization transfer to the nucleus. In contrast, irradiation of the very fast relaxing electron spin (e_2) will not result in electron saturation, and thus no appreciable polarization differential. Consequently, the CE polarization transfer will be truncated at the EPR frequencies resonant with the fast relaxing radical, TCP2 in this study.

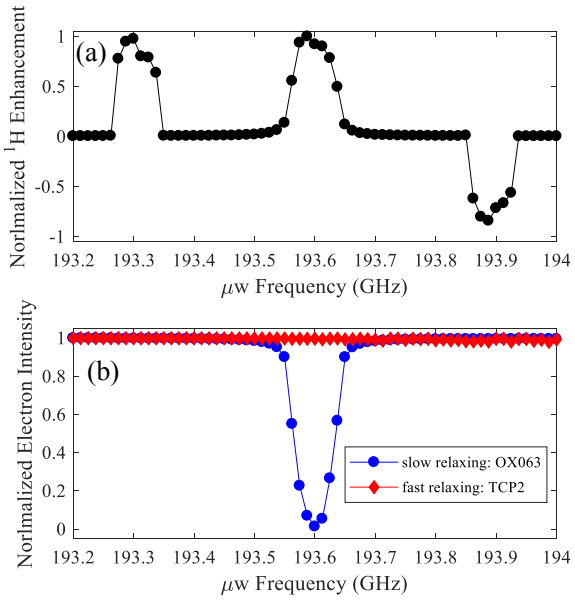

Figure 4.11: (a)Simulated ^{1}H DNP enhancement as a function of μw irradiation frequency, for a e-e-^{1}H spin system at 300 MHz conditions. (b) Polarization measurements of the two electrons under the DNP conditions of figure 4.3(a). This is demonstrated using a three spins (two electrons and one proton) based simulation at the experimental condition taken of figure **??**. The longitudinal relaxation rate constants of electrons are taken to be 0.01 and 4 ms, mimicking relaxation rates of TCP2 and OX063, respectively.

4.5 Conclusion

In summary, this chapter reports on the discovery of a truncated Cross Effect (tCE) that has the appearance of an Overhauser-effect DNP. Such an effect was observed when doping OX063 with the nitroxide based radical, TCP2, in vitrified water/glycerol. The mechanistic basis for this astonishing effect was found to be a substructure of the CE mechanism defined by distinct electron spin dynamics properties of fast and slow relaxing radicals. The puzzling OE* or the tCE mechanism can be replicated by quantum mechanical simulations with a mixed radical system, where the two radicals maximize the EPR spectral overlap to fulfill the CE conditions, while one radical type is easily saturated, but not the other, due to very short T_{1e}. This discovery is potentially important in many different ways, one of which is the prospect of the tCE serving as an indirect read out of "dark" (or invisible) electron spins that, despite being undetectable, elicit a tCE by means of a detectable reporter radical. The OE characteristics may be a spurious effect owing to its similarity with the tCE, and therefore, probing the electron spins dynamics will be the ultimate test of the underlying mechanism, and not just analysis of the DNP frequency- and power- profiles.[48, 106]

We also clarify that our study cannot address the mechanistic basis of OE in BDPA, as it is impossible to differentiate between OE and tCE (OE′s doppelgänger) in the case of BDPA with the present level of theoretical understanding, and the currently available experimental methods. Accordingly, we opine that the proposed theory of OE in BDPA as well as the herein discovered tCE in doped OX063 can stand in parallel.

Chapter 5

Crossover from SE to TM ^{1}H DNP with Trityl-OX063

5.1 Introduction

DNP mechanisms relying on the allowed flip-flop transitions of more than one electron-spins are among the most feasible mechanisms to achieve efficient DNP enhancement, as their effect can be enhanced with strong *e*-*e* couplings and better exploited with lower μw powers. One such process is the simultaneous triple-flip of two coupled electron-spins (e_1 and e_2) and a nuclear-spin (n), achieved when the resonance condition, in which the frequency difference ($\Delta\omega_e$) of the two electron-spins (ω_{e_1} and ω_{e_2}) matching the Larmor frequency (ω_n) of a nucleus coupled unequally to both the electron-spins, is fulfilled. A

keystone feature of the triple-flip mechanism is that it does not require μw to drive the flip-flop-flip transition. Rather, μw irradiation only serves to create a large net polarization difference (ΔP_e) between the electron-spin pairs separated by ω_n across the Electron Paramagnetic Resonance (EPR) line. The amplitude of nuclear polarization is then proportional to ΔP_e.[21, 107, 54] Cross effect (CE) and thermal mixing (TM) are two DNP mechanisms that rely both, at its core, on this triple-flip process.[108, 109, 110]

It is noteworthy that the definition and utility of TM-DNP has been a topic of sustained debate and disagreement. Interestingly, the fundamental triple-flip process underlying both TM and CE is the same. According to a recent study by Wenckebach, these mechanisms merely present two distinct limits of the same process, while the extent of e-e coupling acts as the defining factor.[22] In the case of CE, the coupling between electron-spins is weak compared to ω_n, while for TM the coupling must be stronger than ω_n. Accordingly in CE, the difference in Larmor frequencies between the two coupled electron-spins, $\Delta\omega_e$, is largely a result of the g anisotropy or their anisotropic Zeeman interactions. The CE mechanism can fundamentally proceed with two coupled electron-spins if they fulfill the required triple-flip resonance condition. In contrast, $\Delta\omega_e$ in TM results from differences in the dipolar coupling fields experienced by the participating electron-spins from all other surrounding electron-spins, and hence TM typically involves a large ensemble of coupled electron-spins. Macroscopic spin-temperature formalism is widely applied to analyze the dynamics of the electron-spin ensemble under μw irradiation conditions,[108, 109] in which different spin interactions are treated as heat reservoirs, each having a characteristic spin-temperature. Experimentally, μw irradiation is applied in a way that the electron Zeeman (eZ) reservoir is heated and the electron non-Zeeman (eNZ) reservoir is cooled. The coupling of the eNZ reservoir to the nuclear Zeeman (nZ) reservoir via many triple-flip transitions then leads to their subsequent tempera-

ture equalization (Thermal Mixing), and hence subsequent cooling of the nZ reservoir. Time evolution of these spin-temperatures under μw irradiation can be determined using rate equations based on Provotorov's theory[111]. The theory has been subsequently advanced to incorporate the effect of inhomogeneous spin interactions[112, 113] (including g-tensor and hyperfine coupling which are essential for describing TM-DNP), and has been extended beyond the high-temperature approximation.[114, 107, 115]

Multi-nuclear DNP-NMR measurements have been diligently used by researchers to identify the TM-DNP mechanism–exploiting the cross-talk (or indirect interaction) among different nZ reservoirs of nuclei- coupled via the eNZ reservoir.[116] Recently, Guarin *et al.* [117] and Jähnig *et al.* [23], in separate studies, used this approach to determine the dominance of the TM-DNP mechanism with TEMPO (or its derivative) as a function of radical concentration at ∼7 and/or ∼3.5 T. The TM mechanism was found to dominate for strongly coupled electron-spins (regime where homogeneous coupling becomes dominant), that is more likely at lower B_0 field and higher PA concentration.

While the macroscopic spin-thermodynamics approach is well established, the advancement of DNP methods and applications using this framework is limited, as this model does not provide microscopic insights into the underlying spin-dynamics, and hence does not offer a handle how to improve the polarizing agent (PA) and other concrete experimental conditions to exploit the benefits of TM-DNP. Specifically, the variation and the anisotropy that exists in the electron-spin interactions, and its relaxation properties and spectral diffusion rates across the EPR-line are not incorporated in the macroscopic rate equations.

To provide microscopic insight into the spin-temperature model, Köckenberger and

co-workers provided a purely quantum mechanical description of thermal mixing DNP.[43] The major highlight of the quantum mechanical model was its prediction that a strong asymmetry in the *e*-*e* coupling is an essential criterion for establishing an efficient TM-DNP mechanism in a primarily homogeneously broadened EPR-line.

In another quantum mechanical study, Vega and coworkers predicted that the pump-probe ELDOR experiment can be used to differentiate between the strong *e*-*e* coupling regime giving rise to TM-DNP from the weak coupling regime giving rise to CE DNP.[50] Their simulation showed that strong coupling leads to hyperpolarization of select electron-spin populations that manifests itself in a characteristic ELDOR pattern revealing an electron-spin temperature (i.e. polarization) gradient. Notably, these EPR features signifying the TM mechanism have never been experimentally demonstrated under practical DNP conditions at high B_0 fields.

This chapter reports on the surprising and never before seen observation of crossover in the dominant ^{1}H-DNP mechanism at 7 T from Solid Effect (SE) to TM using Trityl-OX063 with increasing PA concentration. Triple-flip based DNP was never forecasted nor reported for ^{1}H nuclei using Trityl-OX063 at high B_0 field, as its g-anisotropy is much smaller than the ^{1}H Larmor frequency (here 300 MHz). We unambiguously diagnosed the dominant ^{1}H DNP mechanism to be TM by means of experimental EPR analysis, in alignment with theoretical predictions, and by toggling between SE- and TM-DNP by design. Knowing the underlying DNP mechanism is important as the design criteria to optimize the sample system are entirely different for different DNP mechanisms. Furthermore, TM reveals distinctly superior practical benefits for DNP-NMR, as will be discussed in this study.

5.2 Experimental Methods

We present our experimental results that were obtained with a ∼7 T, static, dual EPR-NMR spectrometer. The polarizing agent (PA), Trityl-OX063 (purchased from GE Healthcare AC), was dissolved in DMSO-water glassing solvent of d_6-DMSO (Cambridge Isotopes), D_2O (Cambridge Isotopes) and H_2O in the ratio 78:14:8 by % weight, respectively, unless mentioned otherwise.

5.3 Results and Discussion

5.3.1 DNP Signature of TM

Figure 5.1 shows the normalized ^{1}H-DNP frequency profile of Trityl-OX063 for four different PA concentrations at 20 K using 350 mW of μw power. At a modest concentration of 10 mM, a large positive and negative enhancement was observed for the μw irradiation frequency ($\nu_{\mu w}$) set to 193.35 and 193.95 GHz, corresponding to an offset of ±300 MHz from the Trityl-OX063 center frequency. Therefore, this fulfills the expected conditions for SE-ZQ and SE-DQ DNP for the Trityl-OX063 radical (ZQ and DQ stand for zero-quantum and double-quantum, respectively). Unexpectedly, we observed an additional, small but distinct, enhancement peak (dispersive in feature) for $\nu_{\mu w}$ near the center of the Trityl-OX063 resonance. This center enhancement feature intensified in magnitude to ∼25% of the SE-DNP peak as the PA concentration was increased from 10 mM to 20 mM. When the PA concentration was further increased to 40 mM, its magnitude surpassed that of the SE-DNP enhancement feature by a factor of nearly two. At even higher PA concentration of ∼100 mM, the center enhancement was significantly boosted, while the enhancement observed at the SE conditions was drastically attenu-

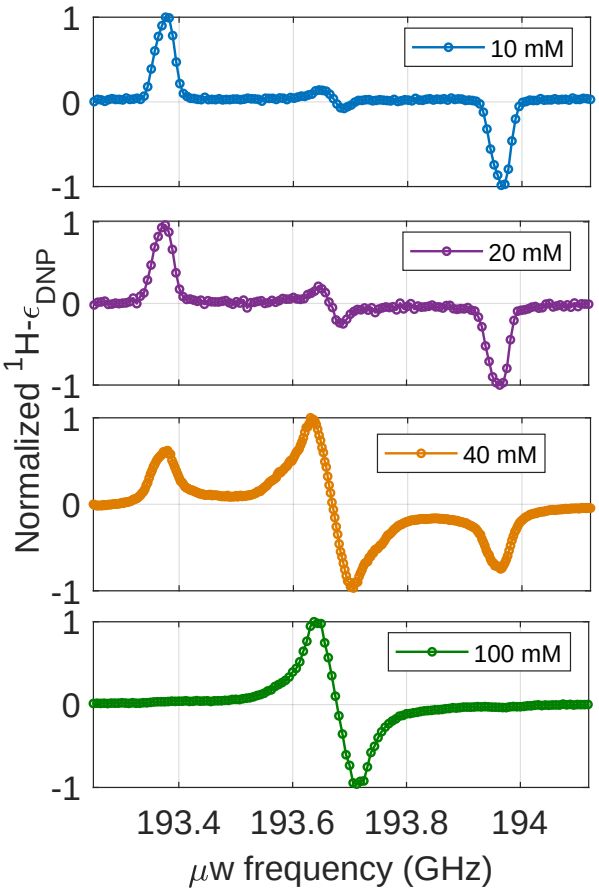

Figure 5.1: **Crossover from SE to TM.** Experimental ^{1}H-ε_{DNP} vs. $\nu_{\mu w}$ at 7 T and 20 K static condition, measured for four different Trityl-OX063 concentrations in DMSO solvent, using $P_{\mu w}$ = 350 mW, $t_{buildup}$ = 2 s.

ated, resulting in an enhancement ratio for the central-to-SE peak greater than 50! This observation was unexpected as Trityl-OX063 has a small g-anisotropy (with associated linewidth of order ∼65 MHz) compared to the ^{1}H Larmor frequency of 300 MHz at 7 T. The DNP enhancement cannot be attributed to OE as the profile is dispersive and the effect clearly increases in relative intensity with increasing radical concentration, i.e. the *e*-*e* coupling strength. There is no mechanistic basis for fluctuating e-n hyperfine couplings of the order of $\omega_e \pm \omega_n$ (∼200 GHz at 7 T) in the Trityl-OX063 PA system dissolved in DMSO-water (insulating matrix) at 20 K that scales with the *e*-*e* coupling

strength. Also, the underlying DNP mechanism cannot be CE as per the established definition of CE, in which $\Delta\omega_e$ originates from the difference in Zeeman interaction between the electron-spins involved in triple-flip.

Conc. (mM)	$^1H - \epsilon_{SE}$	$^1H - \epsilon_{TM}$	$^1H - \epsilon_{TM}/^1H - \epsilon_{SE}$
10	10	1.6	0.16
20	19.2	5	0.26
40	14	30	2.14
100	2	110	55.0

Table 5.1: **DNP Enhancement.** Experimental ^{1}H-ε_{DNP} for different Trityl-OX063 concentration using 2-s long, 350 mM μw power, measured at 20 K and 7 T.

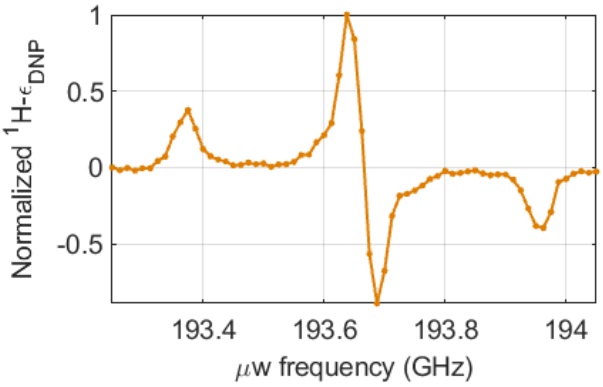

Figure 5.2: **DNP frequency profile** Experimental ^{1}H-ε_{DNP} vs. $\nu_{\mu w}$ at 7 T and 110 K, under static condition, measured for 40 mM Trityl-OX063 concentrations in DMSO solvent, using $P_{\mu w}$ = 350 mW, $t_{buildup}$ = 2 s.

The question then is what is the mechanistic origin of this center peak in the DNP profile? Since the relative contribution of the center peak to the SE enhancement is increasing with PA concentration (see table 5.1), the mechanism must benefit from stronger *e*-*e* couplings. In fact, strong *e*-*e* couplings exceeding the EPR linewidth and approaching that of the ^{1}H Larmor frequency offers a mechanistic basis for TM-DNP, rather than CE DNP. Such enormous *e*-*e* couplings in a Trityl-OXO63 system inevitably requires the clustering of this PA. Reassuringly, it has already been demonstrated in the literature, by a combination of EPR, mass-spectrometery and cryo-electron microscopy, that Trityl

self-assembles (prominently in Trityl-Finland, but also seen in Trityl-OX063) to nanoparticles.[118, 119] The resulting *e*-*e* coupling will be, in part, manifested in a broadened EPR spectrum, while stronger *e*-*e* couplings exceeding the EPR resonance will be increasingly difficult to detect as they broaden into the background. This characteristic center peak in the DNP profile was furthermore observed across a wide temperature range (figure 5.2), which can be reconciled with the TM-DNP, but not the OE-DNP mechanism. The ratio $^1H - \epsilon_{TM}/^1H - \epsilon_{SE}$ increases from 1.81 at 18 K to 2.85 at 120 K. Finally, we point out that the relative contribution of TM dominates over the SE at a PA concentration exceeding 40 mM (figure 5.1).

In fact in the literature, Karabanov *et al*. reported on observing the TM-DNP effect in 15 mM Trityl-D3 dissolved in 2:1 tetrahydrofuran:toluene solvent at 1.4 K and 3.35 T, but suggested that TM-DNP is not expected in Trityl-OX063 given its water solubility.[43] We propound that it cannot be *apriori* predicted whether a PA system will yield significant TM-DNP or not, especially as the DNP efficiency can become less favorable at PA concentration exceeding a threshold. This is because the DNP efficiency depends on the relative rates of μw transition, electron-spectral-diffusion and electron-spin relaxation processes that are not independent of each other, but are inextricably linked with the radical-radical and radical-solvent interactions, and therefore needs experimental scrutiny. We discuss next the empirical diagnosis of TM-DNP by EPR and ELDOR line-shape analysis.

5.3.2 EPR Signatures of Thermal Mixing

5.3.2.1 EPR line-shape

We anticipate that TM is an important mechanism for DNP applications, or is already playing a significant role in existing DNP experiments. However, it is difficult to deconvolute the various, simultaneously operating, mechanisms. In the literature, DNP mechanisms are often discerned based on the shape of the DNP frequency profile or μw power dependence. Such experimental inference can be highly misleading, especially if the EPR characteristic of the source of the polarization is unknown, as exemplified in the recently published discovery of the truncated CE by our group that revealed DNP frequency and power profile reminiscent of OE-DNP that, mechanistically, is not.[38] Here, the capability to measure electron-spin dynamics of the PA under DNP conditions[120, 121, 38] will be critical to discerning the DNP mechanism. Using a quantum mechanical treatment, Karabanov *et al*. had predicted that an essential criterion for efficient TM-DNP mechanism is an asymmetry in the *e*-*e* coupling leading to an asymmetric EPR line-shape.[43] Such an asymmetry ensures that the polarization gradient can be non-zero in the strongly broadened EPR-line. We tested this theoretical prediction experimentally by recording the μw frequency-swept pulsed-echo EPR profile of Trityl-OX063. As shown in figure 5.3, we indeed observed a large asymmetry in the EPR line-shape, which becomes more prominent as the radical concentration is increased from 10 mM to 100 mM. Reassuringly, the asymmetry in the EPR line-shape was clearly visible at concentration $>$ 10 mM, when the TM-DNP signature also became apparent in the DNP frequency profile.

The T_{1e} and T_m relaxation rates of the electron-spins are found to be different across the EPR-line, and increased at higher PA concentrations, consistent with an inhomogeneous electron-spin population. There exists a large electron-spin population that is

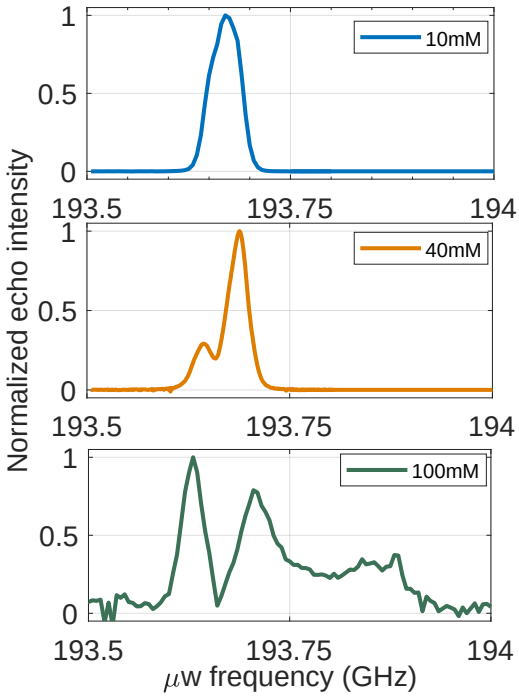

Figure 5.3: **Pulsed EPR spectra.** Echo-detected EPR-line recorded at 20 K for 10, 40 and 100 mM Trityl-OX063 in DMSO solvent under the DNP conditions.

not visible in the echo-detected EPR spectrum shown in figure 5.3 (measured with μw power of 350 mW) due to their very short relaxation times T_{1e} and T_m. By employing higher μw powers available at Q-band, a greater portion of the hidden electron-spin populations could be detected in the echo-detected EPR spectrum (as illustrated in figure 5.4 and 5.5). However, the electron-spin relaxation time was too short to record the entire EPR line. Alternatively, quantum mechanically forbidden, half-field transitions corresponding to $\Delta m_s = \pm 2$ have been used by Eaton *et al.* to estimate the inter-radical (r) distances[122]. However, getting any quantitative information about clustered spin-states using half-field transition is not possible. We note that two electron-spins that are $6.37\mathring{A}$ apart will span an EPR line that is wide enough to readily encompass the ^{1}H NMR Larmor frequency of 300 MHz at 7 T, and hence can satisfy the triple-flip resonance conditions, as demonstrated with simulated spectra shown in the simulation section.

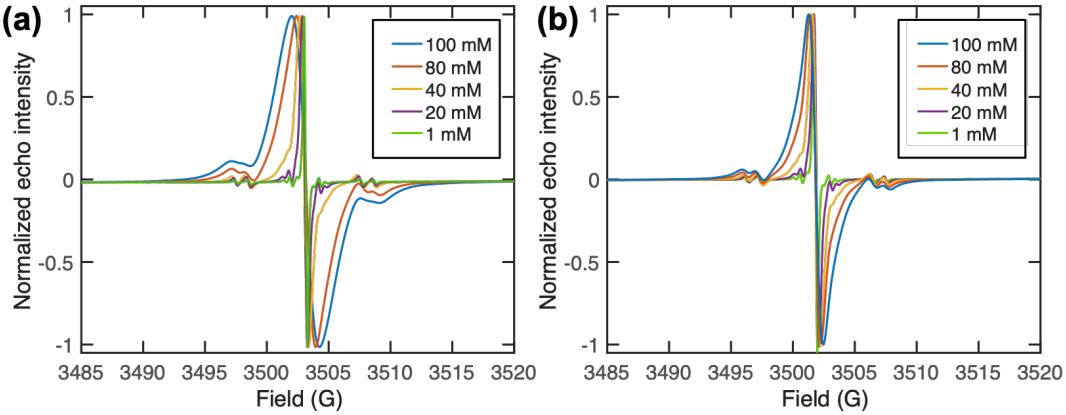

Figure 5.4: **CW EPR** 1-100 mM Trityl-OX063 in (a) d_6DMSO/D_2O/H_2O = 76/14/10 (v/v/v) and (b) d_6DMSO/H_2O = 90/10 (v/v) were examined under room-temperature condition using X-band CW EPR.

5.3.2.2 ELDOR

Pump-probe ELDOR can serve as an important tool to scrutinize the nature of the *e*-*e* coupling network. ELDOR measures how EPR saturation at one frequency (pump) effects the electron-spin polarization at another frequencies (probe) across the EPR spectrum.[106, 47] Strong *e*-*e* coupling (or the consequential TM-DNP) can lead to pronounced hyperpolarization of electron-spins in an ELDOR experiment, as predicted recently in a theoretical study by Kundu *et al.*[50]

To illustrate this effect, we show overlaid ELDOR profiles for 10 mM and 40 mM Trityl-OX063 obtained at 20 K, in figure 5.6. The electron-spin probe frequency was set to (near) the center of the Trityl-OX063 spectrum and the pump frequency was swept from 193.4 to 193.9 GHz using a long saturation pulse of 350 mW of μw power and 50 ms duration. Clearly, at 40 mM PA concentration, the visible hyperpolarization of the probed electron-spin population was observed, as manifested in a gain in the electron-spin

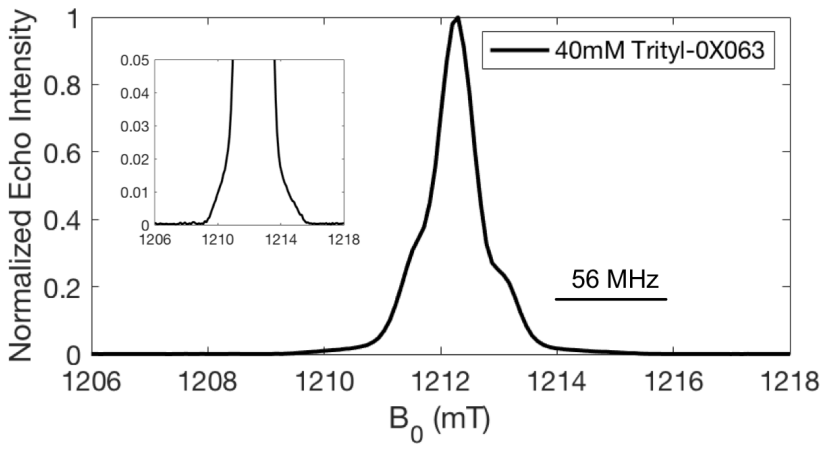

Figure 5.5: **Pulse EPR** Echo-detected EPR spectrum recorded for 40 mM Trityl-OX063 in d_6-DMSO/D_2O/H_2O = 76/14/10 (v/v/v) at Q-Band frequency. A 400 ns long echo delay was used to acquire the spectra. Inset shows zoomed in EPR–line at its base.

echo intensity in the ELDOR spectrum relative to the Boltzmann intensity, normalized to 1. Any visible signature of electron-spin hyperpolarization was absent in the ELDOR spectrum of the 10 mM Trityl-OX063 sample. The ELDOR signature for hyperpolarization of electron-spin populations generated by μw irradiation (also termed an anti-hole in the literature) requires strongly coupled electron-spins, and has been suggested in the literature as a tool to measure electron-spin proximity in Cu(II)-porphyrin dimers.[123, 124]

5.4 Numerical Simulation

5.4.1 Half-filed EPR transition

Half-field transition has been used to show the extent of clustering in Trityl radical by Chen *et al.* and Marin-Montesinos *et al.* [125, 119] To illustrate this spin-physics, we show an Easy-spin[99] simulated EPR spectra for the case of (i) strongly coupled and (ii) uncoupled two-electron spin system (figure 5.7).

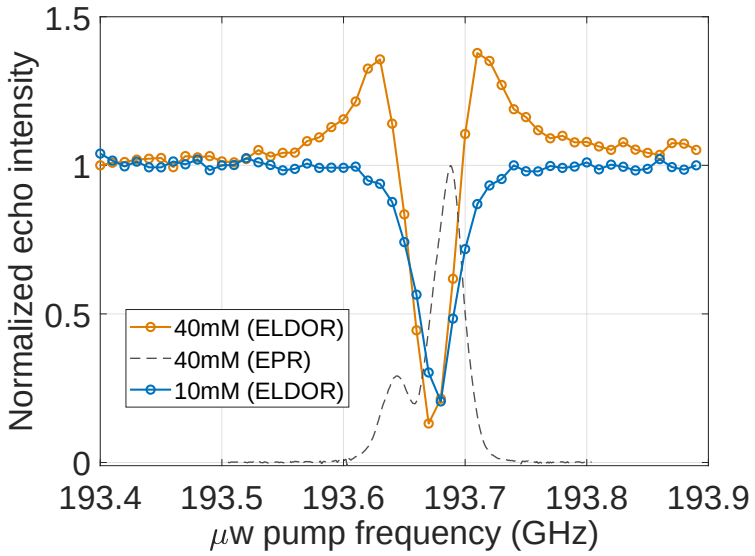

Figure 5.6: **Electron hyperpolarization.** Experimental ELDOR profile recorded at 20 K for 10 and 40 mM Trityl-OX063. Probe frequency was set to 193.675 GHz. A 350 mW and 50 ms long μw saturation pulse was used via the pump channel. Dashed line shows echo detected EPR-line of 40 mM Trityl-OX063 recorded at the same condition.

5.4.2 Multi-component Dipolar Broadened EPR Spectrum

Efficient TM-DNP requires that there is a large dispersion in *e*-*e* coupling strength as pointed out by Karabanov *et al*. [43]. The electron spins (population) that are strongly-coupled presumably have very fast relaxation and may not be detectable in an EPR experiment, but they are important for TM-DNP condition to be satisfied. To illustrate this scenario, figure 5.8 shows simulated EPR of coupled electron spin-system with different ratio of strongly and weakly coupled *e*-*e* pairs. As clustering increases, the population/probability of strongly coupled (broader) component increases.

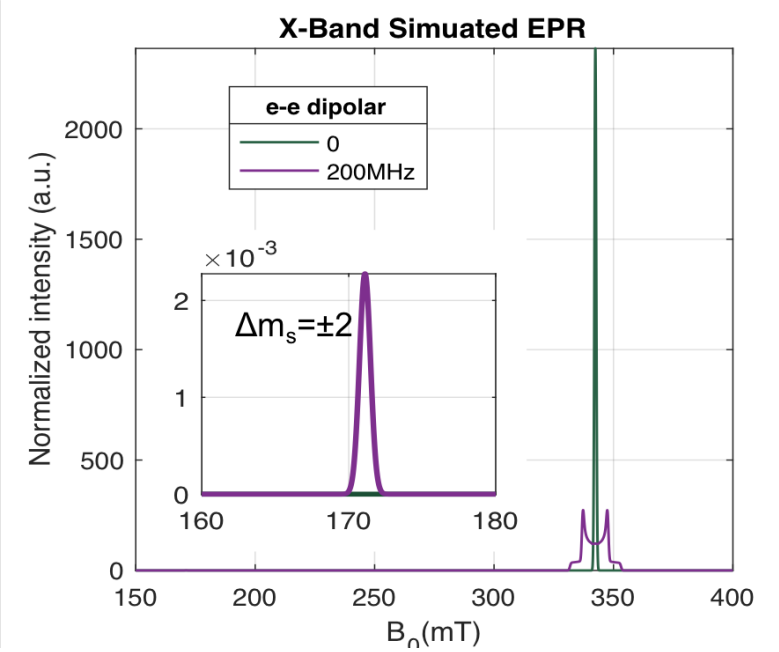

Figure 5.7: **Half-field transition** Easy-spin based simulated EPR spectrum for two electrons having g-ansiotropy equivalent to that of Trityl, at X-band conditions. In case of strong e-e coupling, a non-negligible, $\Delta m_S = \pm 2$ transition is observed.

5.5 DNP μw Power Profile and the CROSS OVER

With the veracity of the TM-DNP mechanism firmly demonstrated, we next examine its practical utility. The ^{1}H DNP frequency profiles shown in figure 5.1 were obtained at the maximum available μw power with our setup. The power dependence of the DNP frequency profile of 40 mM Trityl-OX063 at 20 K using a fixed 2 s μw irradiation time is shown in figure 5.9a. At lower μw power of less than 100 mW, the TM-DNP signature was much more prominent relative to that of SE-DNP. This observation highlights the advantage of TM- over SE-DNP. The μw transition in SE-DNP utilizes the "forbidden" ZQ or DQ transitions of the coupled electron-nuclear spins, while in TM-DNP relies on quantum-mechanically allowed single-quantum spin transitions. With the Trityl-OX063 PA, the TM-DNP feature reached the maximum enhancement with a modest μw power of 200 mW. In stark contrast, the SE-DNP efficiency was far from reaching saturation at

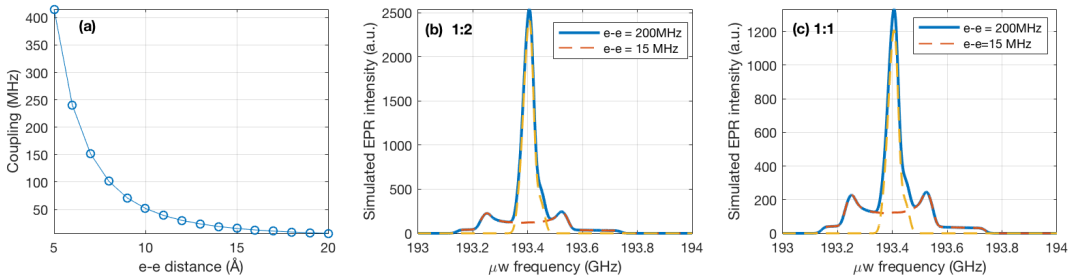

Figure 5.8: **Dipolar Broadening** Dipolar coupling vs. inter radical distance is shown in (a). Easy-spin based simulated EPR spectrum for coupled electron system having two-components in the ratio 1:2 (b) and 1:1 (c). A g-anisotropy equivalent to that of Trityl was considered, at 7 T conditions. Individual components are shown with dashed lines and sum is shown in solid line.

a higher μw power of 350 mW, even at 20 K. This is highlighted with the enhancement at the optimum SE- and TM-DNP conditions plotted vs. μw power in figure 5.9b, clearly demonstrating the lower μw power requirement to achieve effective TM-DNP-induced enhancement. This is also because the TM-DNP mechanism is facilitated by highly efficient electron spectral-diffusion, in which a large number of electron-spins are actively recruited to achieve triple-flip processes. We observe an additional practical benefit of TM-DNP, namely more rapid ^{1}H polarization build-up (table 5.2), and hence greater signal enhancement per unit time. In TM-DNP, the direct e to ^{1}H polarization transfer should be significantly faster due to large e-e couplings, but the bulk nuclear spin polarization buildup is limited by the ^{1}H-^{1}H spin diffusion rate, and hence limited by T_{1n}. An increased rate of triple-flips induced by electron spin clustering has already been shown to cause faster T_{1n} and ^{1}H DNP buildup of protons.[107, 29] This is evident in our investigation too (table 5.2).

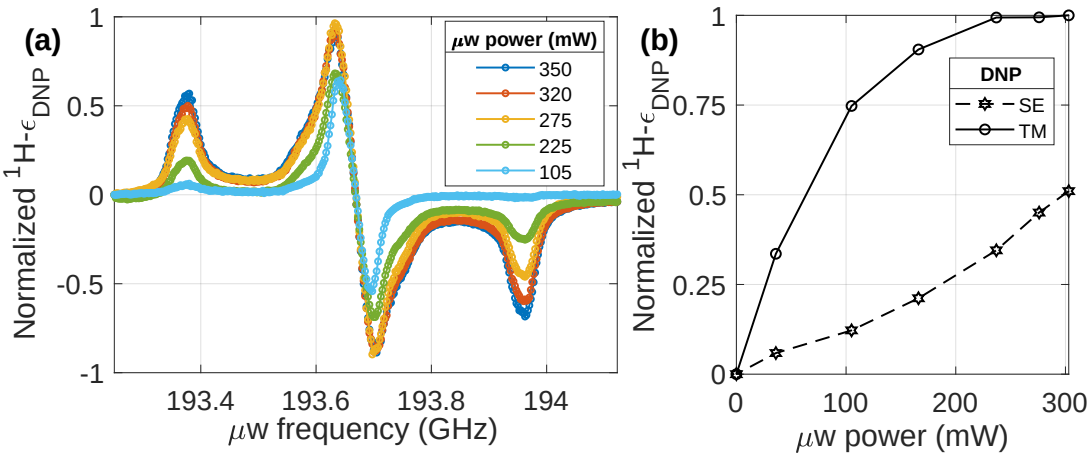

Figure 5.9: μw **power dependence.** (a) Experimental ^{1}H-ε_{DNP} vs. $\nu_{\mu w}$ at 7 T and 20 K static condition, measured for 40 mM Trityl-OX063 using different $P_{\mu w}$, with $t_{buildup} = 2$ s. (b) ^{1}H-ε_{DNP} vs $P_{\mu w}$ obtained at optimum $\nu_{\mu w} = 193.7$ GHz (TM, solid line) and 193.375 GHz (SE, dashed line).

Conc. (mM)	T_{DNP} (s)	T_{1H} (s)
10	80	85
40	40	50
100	1.75	2.5

Table 5.2: Experimental T_{DNP} for TM mechanism and T_{1H} rate constants for different Trityl-OX063 concentration using 350 mM μw power, measured at 7 T and 20 K.

5.6 Conclusion

In conclusion, we report on the crossover of the optimum DNP mechanism from SE to TM using Trityl-OX063 as the PA, as its concentration is increased from 10 to 40 mM at 20 K and 7 T and using 350 mW of μw power. This finding is novel and surprising, as only SE-DNP was expected for the ^{1}H-DNP with Trityl-OX063 in the high B_0 field regime. Electron-spin dynamics investigations under DNP conditions replicated and established the signatures of TM-DNP, including the (i) asymmetry in the otherwise

severely broadened EPR spectrum by strong *e*-*e* coupling, and (ii) hyperpolarization of strongly coupled electron-spin population reflected in a characteristic anti-hole feature observed by pump-probe ELDOR experiment.

The condition required to establish asymmetry in the *e*-*e* coupling network depends on the nature of the molecular interactions, and is not straightforward to predict for a given PA system. Strong *e*-*e* coupling that broadens the EPR line of the order of the nuclear Larmor frequency requires the proximal location of many electron spins, which may be achieved by clustering of electron spins or otherwise close arrangements of multiple electrons, e.g. of multiple radicals grafted on a small molecular framework, serving as PAs.[126] Hence, we presume that asymmetrically and strongly broadened EPR spectra originate from the presence of strongly coupled PAs coexisting with isolated (weakly coupled) PAs (figure 5.8) will bode favorable for TM-DNP. Ideally in the future, PAs with controlled spatial arrangement of electron spins can be designed to tune the TM-DNP effect.

The distinct practical benefits of the TM-DNP process are: (1) lower μw power requirement, (2) faster direct $e - n$ polarization transfer rate leading to enhanced T_{1n} of ^{1}H, and (3) recruitment of a large number of electron-spin pairs (due to fast electron spectral diffusion) to contribute to DNP, making the TM process highly efficient.Further investigation to understand the dependence of TM-DNP on B_0 and magic-angle sample spinning will be an important venture in the future. Another outstanding question is the dependence of equilibration dynamics of the spin-temperature of multiple nuclei on electron and nuclear spin relaxation times, and the cross-talk between nuclei via the electron spins.

Our findings underscore the need to access electron-spins dynamics properties via EPR, in addition to NMR measurements, so as to gain an in-depth understanding of the underlying DNP mechanisms. With a solid understanding, one can more rationally push the limits of the (experimentally) achievable DNP enhancement closer to the theoretical limit. Based on the present investigation, we postulate that TM-DNP can play an important role in the DNP process observed with other commonly used narrow-line radical PAs that can populate PA clusters. For example, the role of BDPA in DNP that was suggested to give rise to OE must be carefully r*e*-*e*xamined.[91] The capability to perform pulsed EPR experiments (using high μw power) under DNP experimental conditions is critical to discover new territories of DNP.[36]

Chapter 6

^{1}H TM DNP with BDPA as Polarizing Agents

6.1 Introduction

A major goal in DNP research is to ramp up the polarization transfer efficiency in the experimentally important regimes of high B_0, under fast magic angle spinning (MAS), and at higher temperatures than the current operating temperature of solid-state DNP at ∼100 K. Significant efforts to make DNP feasible at these conditions are underway,[127, 128, 129] including the impressive improvements shown with newly debuted PAs.[28, 31, 130] Still, the scope of possible development remains expansive and cannot be effectively rendered by heuristic design of PAs and DNP experiments. The

major bottle-neck lies in the lack of precise understanding of the polarization transfer mechanism from electron spins (e) to nuclear spins (n). Transfer can occur via various competing mechanisms that are highly dependent on e-e/e-n couplings and electron spin dynamics. The complexity of electron spin dynamics arises from various factors: electron spin-orbit coupling including the g and hyperfine (A) anisotropies, various possible spin relaxation mechanisms, the number of e interacting with one another, the spatial distribution of e within the e-e coupling network, as well as the spatial distribution of n that interact with the e.[51, 131, 132, 133] In addition, the effects of external perturbation such as the MAS rate and μw pulse irradiation schemes are crucial to understand.

The strategy to improve DNP efficiency, via a rational design of a DNP radical system or new pulse irradiation schemes, largely depends on knowing the precise DNP mechanism requirements and effective conditions. Generally, there are four DNP mechanisms: Solid Effect (SE), Cross Effect (CE), Overhauser Effect (OE), and Thermal Mixing (TM). The operational DNP mechanism directly guides the rational design principle of optimal PAs. To date, PA and DNP experimental design has been focused around optimizing the SE and CE mechanisms,[134, 92, 135, 129, 27, 136, 137, 28] given the in-depth understanding of the two mechanisms that can be illustrated with coupled two-spin e-n or three-spin e-e-n model systems, respectively. [138, 132, 131] However, the intrinsic problem of SE and CE is that the polarization transfer efficiencies are significantly impaired at high B_0.

Unlike the SE and CE mechanisms, TM and OE are less exploited for solid-state DNP. Similar to SE, OE can be described with a two-spin e-n model system, but requires a source of zero quantum (ZQ) and double quantum (DQ) e-n cross-relaxation which is normally absent in insulating solids. This is because cross-relaxation between an electron spin and nuclear spin is mediated by the fluctuation of the e-n hyperfine

couplings, which generally requires molecular dynamics at frequencies comparable to the electron spin Larmor frequencies. Abragam hypothesized that OE exists in non-metallic, paramagnetic solids under circumstances when the *e*-*n* hyperfine coupling is much larger than the nuclear Zeeman interaction.[139] However, such a requirement is mostly not satisfied at the experimental conditions of current solid-state NMR applications, where the ^{1}H Larmor frequencies are on the order of hundred MHz. Furthermore, such effect would be dampened at cryogenic temperatures. Interestingly, there have been on-going efforts in understanding and optimizing the plausible OE DNP in doped silicon at low temperatures (below the metal-insulator transition temperature).[140, 141, 142] OE DNP in doped silicon was originally observed by Honig in 1954 using As doped silicon at 4 K and 0.3 T.[143] Plausible theoretical explanations were proposed by Slichter *et al*. in 1957, [144] where they proposed that the modulation in the hyperfine coupling can be attributed to the lattice vibration between the donor electron and the ^{29}Si. However, it is important to note that unambiguous experimental proof of OE in doped silicon or in insulating material is not available in the literature. Also, the experimental conditions of the above described systems are drastically different from that of solid-state DNP NMR using organic radicals. OE is generally not an effective DNP mechanism in insulating solids at high B_0.

However, in 2014, Can *et al*. reported an unexpected OE-like (which we here refer to as OE') DNP feature at high B_0 (9.4-18.8 T) using the non-conducting, narrow line PA, 1,3-bisdiphenylene-2-phenylallyl (BDPA),[145] where the radical was dispersed in a polystyrene (PS) matrix (2 wt %). The OE' feature was also observed in vitrified samples containing BDPA dissolved in *o*-terphenyl (OTP) solvent, as well as with high concentrations (∼40 mM) of sulfonated-BDPA (a water soluble BDPA derivative) dissolved in a water/glycerol glassy matrix. The performance of this OE' DNP effect with BDPA was

further examined by several groups and showed promising results of large enhancements under diverse conditions: (i) at higher temperatures (up to room temperature) than the operational temperature of conventional solid-state DNP (∼100 K) [127]; (ii) across a wide B_0 field range between 9.4-18.8 T [145, 127], and (iii) with high tolerance towards fast MAS, confirmed up to 40 kHz.[128] The outstanding DNP performance of the OE' in BDPA across such widely divergent conditions urged the validation of the underlying mechanism in order to translate this success to other PAs and applications. Using MD simulations, Pylaeva *et al.* proposed a plausible explanation for the source of potentially rapid fluctuations (on the scale of several hundred GHz) in the hyperfine coupling in the BDPA radical system,[146] but such fluctuations have not been experimentally verified. The subsequent observation by Ji *et al.* of OE' in BDPA at even lower temperatures of 1.2 K generated even greater confusion about the origin of a common molecular fluctuation in the temperatures ranging from 1.2 K to room temperature.[147] A key piece of missing information is the operational electron spin dynamics of the BDPA radical under experimental conditions that yield OE'. There are several EPR studies of BDPA, but of BDPA solution at ultra low temperature (<1 K),[148] or lower magnetic field,[149] or of BDPA-Benzene micro crystals,[150, 151] which are all very different from the current DNP operating conditions, and hence less relevant.

The insight into DNP mechanisms is commonly achieved through DNP-enhanced NMR measurements as a function of B_0 (alternatively μw frequency) or μw power to derive the corresponding B_0 (μw frequency) or μw power dependence of the operational DNP mechanism. However, ascertaining DNP mechanisms only from NMR-based measurements can be misleading, as shown in a recent discovery of the truncated Cross Effect (tCE) with a combination of Trityl-OX063 and Nitroxide radicals in vitrified water/glycerol.[152] In fact, the tCE has a similar DNP frequency and power profiles

as the OE' observed in BDPA.[145] A combination of EPR measurements and quantum mechanical simulations clarified that tCE is fundamentally different from OE' and instead originates from the CE between a slow relaxing, narrow-line, radical (e.g. Trityl) and a fast relaxing broad-line radical that was undetectable with the currently available μw power and detection scheme at high-field, and was posited to originate from clustered nitroxide radical.

Very recently, we discovered TM DNP to be operational in Trityl-OX063 (another narrow line radical with small g-anisotropy, [gx, gy, gz] = [2.0034, 2.0031, 2.0027]),[81] prominently above a PA concentration of 40 mM in a vitrified water/DMSO matrix.[34] A combination of EPR line-shape and electron-electron double resonance (ELDOR) analysis, supported by quantum mechanical simulations were instrumental in the unambiguous assignment of TM DNP as the operational mechanism.[133, 115, 153, 34]

The present study is motivated by the question of whether a different mechanism other than OE is at play for the OE' effect observed with BDPA, and if so, whether the TM mechanism may be operational. We have systematically scrutinized this conundrum for BDPA using a combination of DNP μw frequency and power profile measurements, EPR line-shape analysis and pump-probe ELDOR experiments of BDPA at varying radical concentrations. Quantum mechanical simulations of 3 coupled electron spins and 1 nuclear spin further support our experimental observations.

6.2 Experimental Methods

BDPA in *o*-terphenyl (OTP): Partially deuterated OTP (d_{14}-OTP (Cambridge Isotope) : OTP = 95 : 5, weight percent) melted under 60^{o}C with water bath. BDPA was dissolved in the warm OTP and resulted in concentrations of 0.1 - 40 mM. 40 μL radical-solvent mixture was transferred to a custom cylindrical Teflon sample holder (7.5 mm inner-diameter, 8 mm outer-diameter, 17.8 mm height) and subsequently freeze-quenched in liquid nitrogen to avoid the crystallization of OTP.

2% BDPA in polystyrene (PS): 100 mg PS (Sigma Aldrich, Average MW 35000) was suspended in 5 mL chloroform and 2 mg BDPA (BDPA complex with benzene (1:1), Sigma Aldrich) was added to the mixture. The 2 weight-percent BDPA in polystyrene solid sample was prepared by adding the solution on a glass slice drop-wise and let chloroform vaporize overnight at room temperature. The 2% BDPA PS thin film was scratched off from the glass.

6.3 Results and Discussion

6.3.1 ^{1}H DNP μw Frequency Profile

We first measured the DNP frequency profile, i.e ε^1H (ratio of NMR signal intensities acquired under μw-on and μw-off conditions) vs. μw frequency. Figure 6.1A shows the ^{1}H DNP frequency profile of 10 mM BDPA in the OTP matrix. A large positive and negative ε^1H was observed at μw irradiation frequencies of 193.35 and 193.925 GHz, respectively, which are around $\pm$ 294 MHz (proton Larmor frequency at 6.9 T) away from 193.625 GHz (near the BDPA center frequency at 6.9 T). They correspond to the

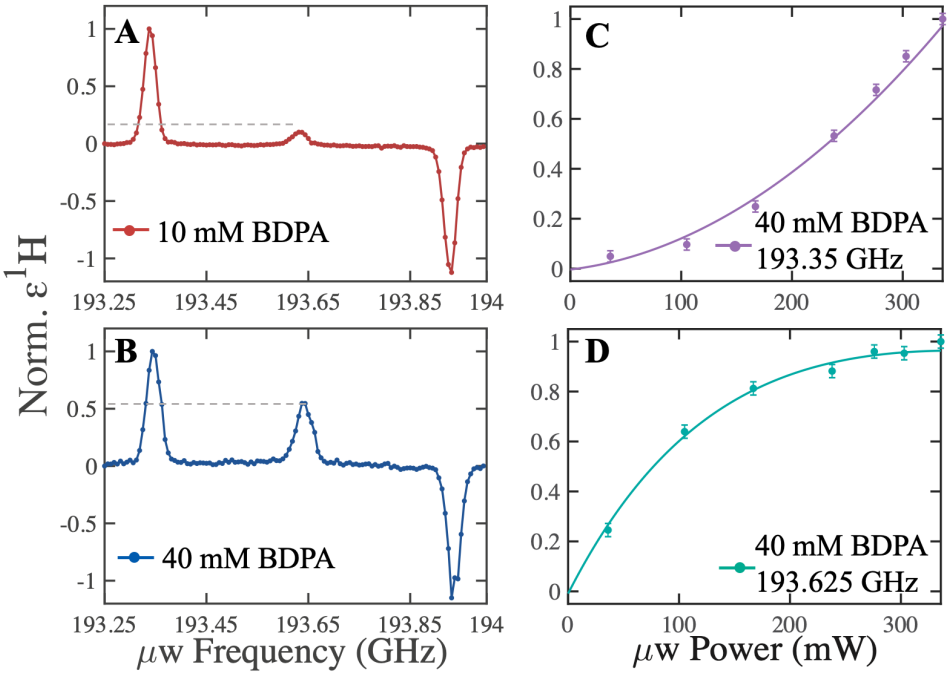

Figure 6.1: ε^1H as a function of μw irradiation frequencies were recorded for (A) 10 mM (red) and (B) 40 mM (blue) BDPA in OTP at 20 K with μw irradiation power of 350 mW. The displayed ε^1H was normalized by the maximum value: 5 for 10 mM BDPA and 55 for 40 mM BDPA. For 40 mM BDPA in OTP, ε^1H was recorded as a function of μw power up to 336 mW with μw irradiation frequency fixed at (C) 193.35 (violet) and (D) 193.625 GHz (green). The solid lines were fitted trendlines while the dots were the experimental data with error bar (standard deviation) indicated. The build-up time was 20 s for ^{1}H DNP measurements.

DQ and ZQ transitions in SE DNP. In addition, a small positive ε^1H intensity ($\sim$10% of the ε^1H acquired at the SE-DQ condition) was observed at the BDPA center transition ($\sim$ 193.625 GHz). This characteristic feature was seen by many other researchers (typically with BDPA at higher concentrations), and is currently assigned to OE DNP in the literature.[145, 147, 146, 128, 127] At a PA concentration of 40 mM, all features of the DNP frequency profile seen with a PA concentration of 10 mM were reproduced. However, the central DNP enhancement dramatically increased from $\sim$10% (10 mM BDPA) to 50% (40 mM BDPA) of the ε^1H at the SE-DQ condition (193.35 GHz) amplitude (figure 6.1B). This observation suggests the central DNP intensity originates from multi-

electron spin effects as they are amplified at increased radical concentration. We note here that fundamentally there should be no dependence of the OE DNP on radical concentration as the OE does not require *e*-*e* interactions. In contrast, mechanisms such as TM and CE DNP have a clear dependence on radical concentration, as recently observed with Trityl-OX063 [34] and 4-Amino TEMPO [47], respectively. Furthermore, the μw power requirement of the SE transition and the central features are strikingly different. The SE DNP effect showed severe power limitations at the maximum μw power of 336 mW available to our DNP instrument (figure 6.1C), while the central DNP intensity readily plateaued off at the same maximum μw power (figure 6.1D). This shows us that the central feature is induced by an allowed transition, leaving the possibility open for CE and TM mechanism to be at play, based on just the DNP-NMR properties. However, CE per definition is incommensurate with narrow line radicals (radicals with small g-anisotropy) whose width does not encompass the nuclear Larmor frequency, leaving TM as the major contender. Of course, the simultaneous existence of OE and TM DNP mechanisms cannot be ruled out.[154] However, the presence of an OE DNP mechanism cannot be proven with presently available experimental techniques and is less likely under DNP conditions at high magnetic fields. With that in mind, next, we further examine whether TM DNP is a viable alternative.

6.3.2 EPR Signatures for TM DNP

6.3.2.1 EPR line-shape Analysis

Using EPR, we have recently established experimental signatures of TM DNP, which is deliberately designed to distinguish TM from other mechanisms. The characteristic EPR signatures are: (i) an asymmetrically broadened EPR line-shape and (ii) hyperpo-

larization of select electron spin populations.[34] Hence, we scrutinized the experimental signatures of TM DNP in both 10 mM and 40 mM BDPA in OTP using EPR measurements under the same DNP conditions.

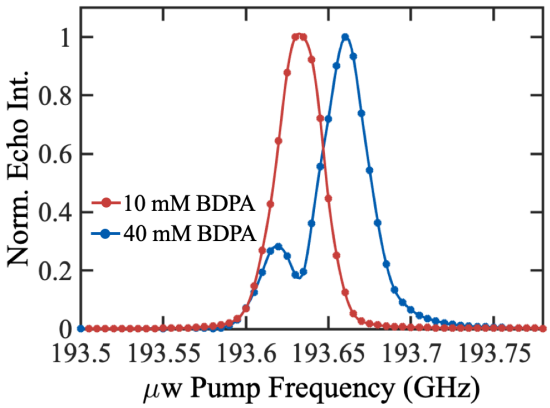

Figure 6.2: Echo-detected EPR lines were recorded for 10 mM (red) and 40 mM (blue) BDPA using 6.9 T pulse EPR/DNP spectrometer under 20 K. The inter-pulse delay for the solid echo detection was 400 ns.

We began with echo-detected EPR line-shape analysis at 6.9 Tesla and at 20 K of the two BDPA samples. The EPR line-shape of 10 mM BDPA showed a single component centered at $\sim$ 193.635 GHz, with a width of 120 MHz at the base (figure 6.2, red). However, the EPR line-shape of 40 mM BDPA was dramatically broadened and displayed significant asymmetry across a μw frequency range of 193.57-193.75 GHz (figure 6.2, blue). Notably, multiple component EPR line-shape for the BDPA sample system has been reported previously under different conditions: 1) 40 mM SN-BDPA (a BDPA derivative) in water/glycerol mixture at 80 K under 5 T [93] and 2) 5 mM BDPA in toluene at 0.5 K under 2.5 T [148]. This asymmetry in the EPR line-shape is the result of strong *e*-*e* (dipolar as well as exchange) couplings indicating the presence of clustered BDPA radicals. In fact, the clustering of BDPA was recently confirmed to occur by a combination of EPR and Mass spectroscopy measurements, where an instability origi-

nating from radical clustering/aggregation was observed with concentrated BDPA and its derivatives (tested up to 30 mM) prepared in a series of organic solvents above -80°C .[149] As previously discussed by Karabanov *et al.*[133] and later confirmed by Equbal *et al.*[34], the asymmetric EPR-line is one of the distinctive features of TM DNP. Asymmetry is necessary to maintain a large polarization gradient across the dipolar broadened EPR-line under μw irradiation, and provide a mechanistic basis to induce effective triple-flips that constructively add up to DNP enhancements. It is important to note that a significant population of electron spins are possibly "hidden" from echo-detected EPR due to fast relaxation (decoherence) of strongly coupled electron spins that approach the detection limit by the current pulsed EPR capabilities at high field.

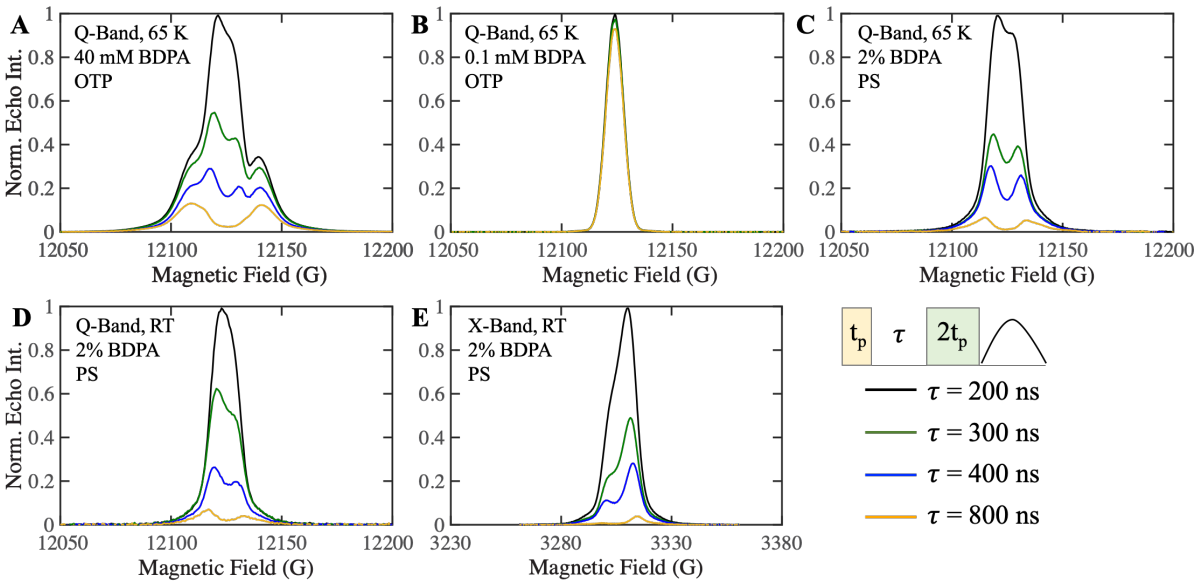

Figure 6.3: Echo-detected EPR line-shapes for different BDPA samples under variable experimental conditions are obtained. Inter-pulse delays are varied between 200 and 800 ns. t_p = 16 ns is used for all the measurements. Under Q-band spectrometer at 65 K, (A) 40 mM BDPA in OTP, (B) 0.1 mM BDPA in OTP and (C) 2% BDPA in PS are examined. 2% BDPA in PS is also examined at room temperature with (D) Q-band as well as (E) X-band.

In figure 6.3, echo detected EPR line-shape of BDPA radical systems were further ex-

amined using X- and Q-band EPR spectrometers. The EPR line-shapes of concentrated BDPA (40 mM BDPA in OTP and 2% BDPA in PS) all displayed asymmetrical multi-component features. These features were observed under different magnetic fields (X- or Q-band) and temperatures (65 K or room temperatures). However, the EPR line-shape of low concentration BDPA (0.1 mM in OTP) had only one narrow component where the asymmetry is not obvious.

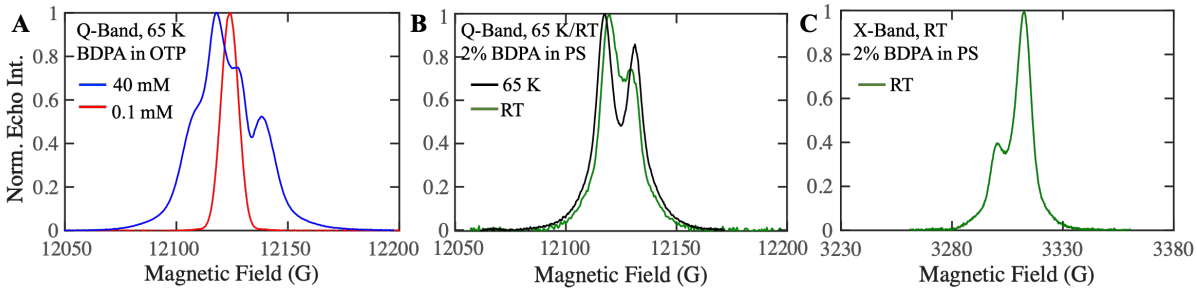

Figure 6.4: Echo detected EPR line-shapes of BDPA systems are overlaid to demonstrate their (A) concentration, (B) temperature and (C) field dependencies.

EPR line-shapes of 40 mM (blue) and 0.1 mM (red) BDPA in OTP obtained at 65 K under Q-band were first overlaid in figure 6.4A. The linewidth at the base for 40 mM BDPA (∼322 MHz or ∼115 Gauss) is much wider than that of 0.1 mM BDPA (∼70 MHz or ∼25 Gauss). EPR line-shape of 2% BDPA in PS obtained at Q-band for both 65 K (black) and room temperature (green) are similar, as displayed in Figure S3B. An asymmetric EPR line-shape containing multiple components was also detected of 2 wt% BDPA in PS at X-band (figure 6.4C). Consistently across different magnetic fields and temperatures (figure 6.4B), the EPR linewidth of 2% BDPA in PS is nearly invariant at ∼154 MHz (∼55 Gauss). This reveals that the EPR line-broadening of high concentrations of BDPA is mainly caused by interactions that are independent of the magnetic field, such as *e*-*e* dipolar and J couplings.

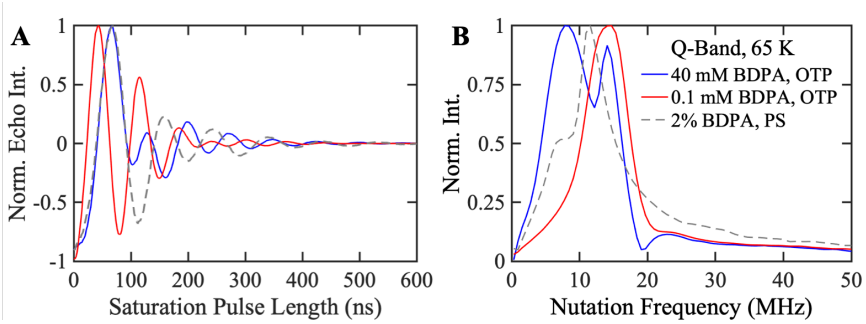

Figure 6.5: A: The nutation experiments (varying the saturation pulse length up to 600 ns followed by a Hahn Echo detection, $t_p = 16$ ns) for 40 mM BDPA in OTP (blue solid line), 0.1 mM BDPA in OTP (red solid line) and 2% BDPA in PS (grey dash line) are obtained under Q-band at 65 K. B: The corresponding Fourier transformed nutation frequencies.

Multi-spin effect has been further verified with the nutation frequency measurement (figure 6.5A) and the corresponding Fourier transformed nutation frequencies (figure 6.5B). It is further confirmed that there are multiple spin species with different nutation frequencies existing in high concentration BDPA (40 mM BDPA in OTP and 2% BDPA in PS) while only one major nutation frequency existing in low concentration BDPA (0.1 mM in OTP).

We suggest that the 40 mM BDPA sample consists of populations of species with varying degrees of clustering that display fast T_{1e} relaxation times. The in-homogeneity in the clustering BDPA species can be deduced from the variations in the T_{1e} values at different μw irradiation frequencies measured for both 10 mM BDPA at 20 K and 40 mM BDPA at 60 K in OTP (figure 6.6). Taken together, this observation demonstrates that the dipolar or exchange broadening of a narrow line radical can be significant enough, in the presence of radical clustering, to encompass the ^{1}H NMR Larmor frequency, here 294 MHz, and hence offer the energy difference to induce a triple *e-e-n* spin flip.

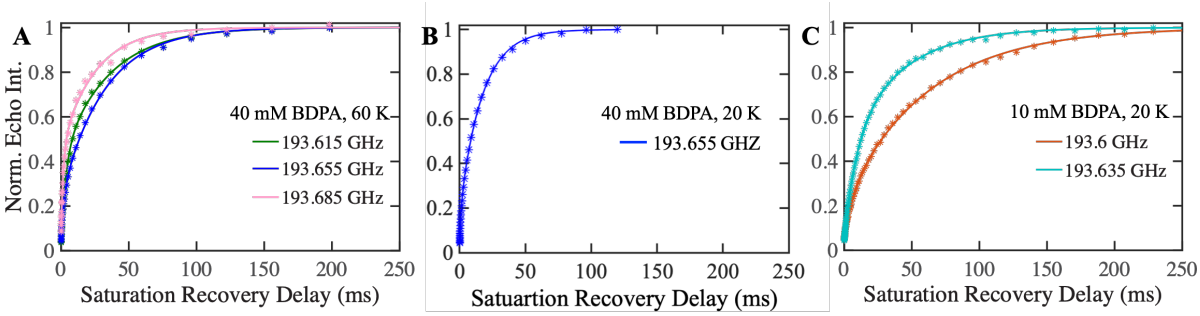

Figure 6.6: Saturation recovery experiments were used to measure the T_{1e} at 6.9 T with variable μw irradiation frequencies. The different BDPA samples are: (A) 40 mM BDPA in OTP at 60 K, (B) 40 mM BDPA at 20 K and (C) 10 mM BDPA at 20 K. The μw irradiation frequencies can be seen in the legend. The experimental data points are displayed in "*" while the fitted curves are in solid lines.

6.3.2.2 ELDOR

We sought to reveal additional TM DNP signatures by ELDOR under DNP conditions.[153, 34] ELDOR is a pump-probe experiment, which measures the μw saturation transfer from the electrons at the pump frequencies to electrons at the probe frequency. The ELDOR spectra were normalized to the echo intensity obtained when the μw pump frequency was set at the far end of the EPR spectral base-line (Boltzmann polarization). Saturation leads to lowering of the echo intensity, i.e. smaller than 1. In contrast, μw induced electron spin hyperpolarization would lead to an echo intensity greater than 1.

Two sets of ELDOR experiments were carried out for each BDPA sample at two different probe frequencies, while continuously stepping through the pump frequency across the entire EPR line. The echo-detected EPR line-shapes of the 10 and 40 mM BDPA samples are indicated in light red and blue shades in figure 6.7 to guide the eye. The ELDOR spectrum of 10 mM BDPA showed an intense dip below 1, reaching values as low as 0.2 at a pump frequency matching the probe frequency, a phenomenon observed when both 193.6 GHz and 193.635 GHz were set as probe frequencies (figure 6.7A). The

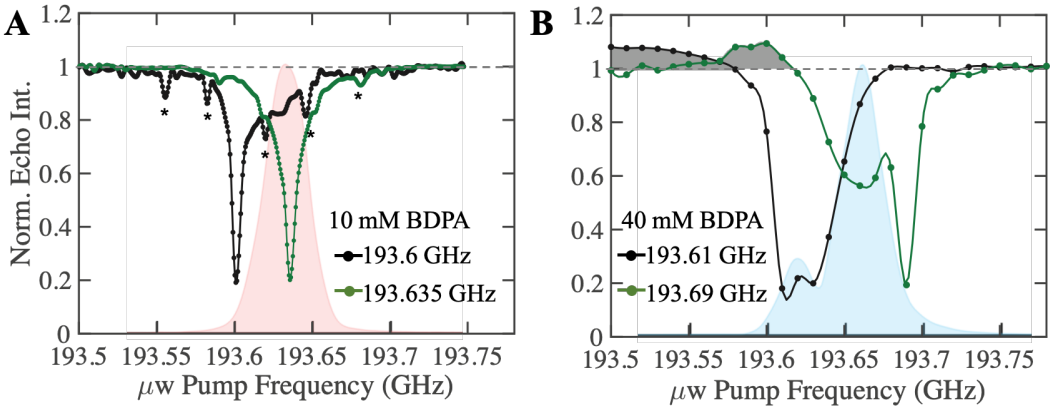

Figure 6.7: A. ELDOR experiments were recorded for 10 mM BDPA in OTP at 20 K, where the μw probe frequencies were set at 193.6 GHz (black) and 193.635 GHz (green). The light red shade is the 10 mM BDPA EPR line recorded under the same experimental conditions displayed as a reference. B. ELDOR experiments were also recorded for 40 mM BDPA at 20 K, where the μw probe frequencies were set at 193.61 GHz (black) and 193.69 GHz (green). The light blue shade is the 40 mM BDPA EPR line. The electron hyperpolarization region are highlighted as the grey shade in the spectra. The saturation pulse for the μw pump frequency is 50 ms with an amplitude of 350 mW.

dips are broadened by electron spectral diffusion (eSD). However, the ELDOR intensity stayed at or below 1 across the entire frequency range, implying that little/no hyperpolarization of electron spin populations occurred upon μw irradiation of 10 mM BDPA. (Here, the sharp dips at the frequencies marked with "*" come from standing wave issues from the DNP spectrometer). The ELDOR spectrum of 40 mM BDPA, acquired under the same experimental conditions as of 10 mM BDPA, is dramatically different (figure 6.7B). We can clearly see a significantly broader hole burnt when the μw probe frequency was set to 193.61 GHz (black), signifying much larger eSD effects due to the presence of the strong *e*-*e* coupling network in 40 mM BDPA. At this probe frequency, in addition to the dip centered around the μw probe frequency, another dip is burnt around the BDPA center frequency of 193.635 GHz due to eSD. A similarly large eSD was also observed when the μw probe frequency was set to 193.69 GHz (green) in the ELDOR profile. Most importantly, we clearly observe the hyperpolarization of electron spins (highlighted in the

grey shaded area) with 40 mM BDPA for both probe frequencies. The hyperpolarization of electron spins have been theoretically predicted by Kundu *et al.*[153], and recently experimentally deduced by Equbal *et al.*[34] as an unambiguous indicator of strong *e*-*e* couplings and an EPR fingerprint for the TM DNP mechanism.

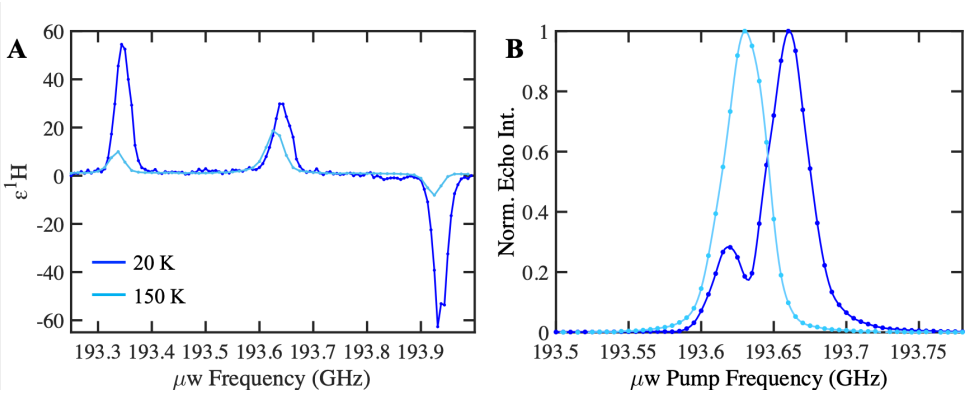

Figure 6.8: A: ε^1H as a function of μw irradiation frequencies were recorded for 40 mM BDPA in OTP under 20 K (blue) and 150 K (light blue). B: Echo-detected pulse EPR line-shapes of the same sample are also displayed for the two temperatures. t_p used in the high field EPR measurement is 500 ns with an amplitude of 350 mW.

Thus, based on the characteristic features of the DNP frequency profiles, power saturation curves, asymmetrically broadened echo-detected EPR line-shape and the ELDOR spectra, we conclude that TM is the underlying DNP mechanism at the BDPA center frequency. Similar to the previous study of ^{1}H TM DNP in Trityl radical systems,[34] the DNP and EPR signatures of TM are clearly visible for 40 mM BDPA and less pronounced in 10 mM BDPA. This TM mechanism is also reproduced in 40 mM BDPA in OTP at higher temperature (150 K), resulting in an enhancement of 19 using 350 mW of μ irradiation power (figure 6.8). In fact, TM of ^{13}C DNP has been reported by Becerra *et al.* in 1993 for 2 wt % BDPA in PS at 5 T [155] and recently by Radaelli *et al.* for 60 mM and 120 mM SA BDPA in water/glycerol mixture at 6.7 T,[156] suggesting that the spatial distribution of such a BDPA spin system can lead to TM DNP already. Although

the possibilities of ^{1}H TM DNP of BDPA in PS or SA-BDPA in water/glycerol mixture have not been examined, we are confident to propound that it is the same TM DNP mechanism arising at the BDPA EPR center transition for ^{1}H DNP of BDPA in PS and SA-BDPA in water/glycerol.

6.4 Numerical Simulation

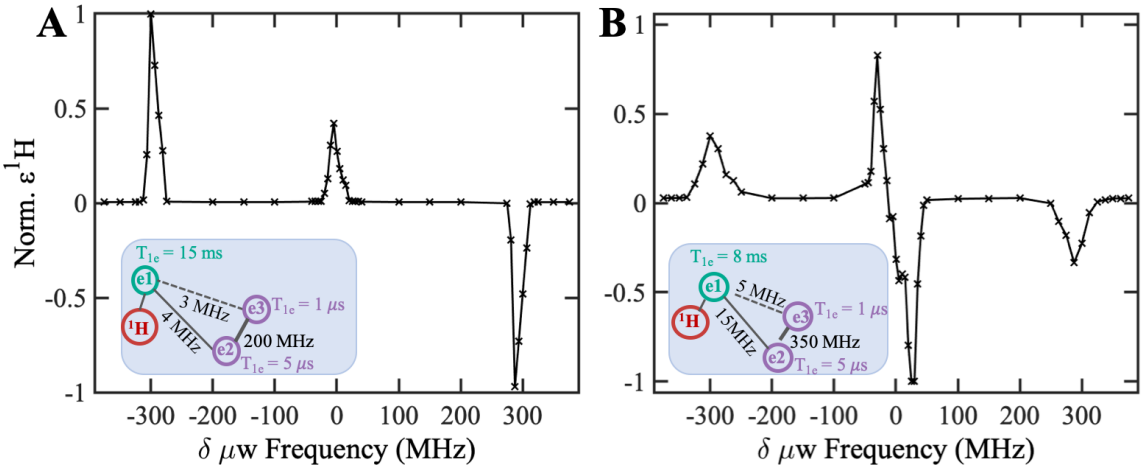

Figure 6.9: Simulated ^{1}H DNP enhancement as a function of μw irradiation frequency for a e_1-e_2-e_3-^{1}H spin system at 294 MHz conditions under MAS rate of 10 kHz. A. Using g-tensor of BDPA, and couplings: e_2- e_3 = 200 MHz, e_1 - e_2 = 4 MHz, e_1- e_3 = 3 MHz, and relaxation rates T_{1e}: 15 ms, 5 μs and 1 μs fore e_1, e_2 and e_3, respectively. B. Using g-tensor of Trityl, and couplings: e_2- e_3 = 350 MHz, e_1- e_2 = 15 MHz, e_1- e_3 = 5 MHz, and relaxation rates T_{1e}: 8 ms, 5 μs and 1 μs fore e_1, e_2 and e_3, respectively.

An intriguing issue is that the envelope shape of the central DNP frequency profile is different when using BDPA v.s. Trityl-OX063 as the PA at 6.9 T. While Trityl-OX063 shows a dispersive shaped (anti-phase) central feature in the ^{1}H TM DNP frequency profile,[34] BDPA consistently shows a positive absorptive shaped (in phase) central feature in the ^{1}H TM DNP frequency profile. We set out to model this difference using

quantum mechanical (QM) simulations. Our aim is not to model the exact experimental condition, but rather to test the hypothesis that the absorptive vs dispersive shape of the central DNP feature depends on the asymmetry in electron spin coupling, which in turn relies on the (spatial) topology of the electron spin coupling network and the different relaxation rates of the different electron spin packets. QM simulation of DNP was performed using the Spin-Evolution software [61]. Taking insights from pulsed EPR measurements, we understand that the electron spin system representing BDPA comprises of the sum of at least two populations: 1) very strongly coupled electron spins with fast relaxation time, i.e the "hidden" BDPA population to EPR detection at the available μw power with our high field EPR spectrometer, and 2) weakly coupled electron spins with relatively slower relaxation times, i.e the "visible" BDPA population that can be detected by EPR and saturated with our high field EPR spectrometer.

The Thermal-Mixing DNP simulations of coupled narrow-line radicals were performed using Spin-Evolution software package, under 6.9 T and 100 K conditions.[61] The simulations were performed in Liouville space, incorporating phenomenological relaxation rates into account. A minimal of 3 electron spins are needed to demonstrate the triple-flip ^{1}H Thermal-Mixing DNP in narrow-line organic radicals (g-anisotropy smaller than ^{1}H Larmor frequency). Therefore, all the simulations were performed for $e_1 - e_2 - e_3 - ^1$H, with e_i representing a narrow-line radical with principle components of g-tensor equivalent to [2.0028 2.0026 2.0025] for BDPA[157] and [2.0034 2.0031 2.0027] for Trityl.[81] The enhancement was calculated with respect to the thermal Boltzmann polarization under static. Powder averaging was done using 50 (α, β) angles following Lebedev scheme for weighted orientation distributions. Notably, numerical results with higher number of orientations showed the same trend as with 50 orientations.

Unless mentioned otherwise, the spin parameters used for the calculations were as follows: the g-tensor of e_2 and e_3 were orientated with respect to e_1 by the Euler angles sets, (20, 30, 0) and (40, 60, 0), respectively (in degrees). In both types of PA, the relative $e_1 - e_2$, $e_1 - e_3$, $e_2 - e_3$ dipolar tensor orientations (relative to e_1 g-tensor) were given by the Euler angles (20, 30, 30), (50, 90, 60), and (0, 45, 90), respectively. These choices were random as the orientations of the spin tensors in a clustered systems are not unique. For simplicity, only $e_1 -^1 H$ hyperfine coupling (2 MHz) was considered with a random orientation of (40, 10, 0). The spin relaxation rate constants of visible electron spins were chosen based on their phenomenological values detected for 40 mM BDPA and Trityl. T_{1H} set to 4 s.

The μw centre frequency was set around isotropic g of the e_i resonance. The simulations were carried out using 0.2 MHz μw power. In the plots presented in this section, an averaging over relative dipolar orientation (β angle) of $e_2 - e_3$ was done to account for conformational distributions in clustered system. Averaging smoothens the shape of frequency profiles but makes computationally significantly expensive. The calculations were under 10 kHz spinning condition to circumvent the need for a very large number of powder orientation in a broad static spectrum.

Accordingly, we constructed a minimal e_1-e_2-e_3-^{1}H four-spin model, in which e_2 and e_3 are strongly coupled (dipolar coupling set to 200 MHz, $r_{e_2e_3} = 6.37\mathring{A}$) and have a short T_{1e} ($5\ \mu s$ and $1\ \mu s$), and e_1, with a longer T_{1e} value of 15 ms, relatively weakly coupled to e_2 (dipolar coupling = 4 MHz, $r_{e_1e_2} = 23.5\mathring{A}$) and e_3 (dipolar coupling = 3 MHz, $r_{e_1e_2} = 25.9\mathring{A}$). Exchange interactions between the coupled electron spins were ignored for simplicity. Plausible T_{1e} values were chosen for the visible electron spins based on T_{1e} measurements of 40 mM BDPA in OTP at 20 K under 6.9 T. The simulations were per-

formed using the g-anisotropy of the BDPA radical.[157] For simplicity, only the e_1-^1H hyperfine coupling (2 MHz) was considered. All DNP simulations were performed at 6.9 T and under MAS at 10 kHz spinning frequency to account for large powder orientation and associated anisotropy. The QM simulation results derived under MAS are also valid under static conditions.[152]

Encouragingly, we could reproduce a DNP frequency profile as observed experimentally using BDPA as the PA, where a positive and absorptive enhancement envelope was observed around the BDPA center transition frequency, along with SE DNP features at the SE-DQ transition of -300 MHz and SE-ZQ transition of 300 MHz (figure 6.9A). This demonstrates the proof-of-principle that the absorptive central feature of the DNP frequency profile observed experimentally can originate from triple-flip DNP mechanisms without needing to invoke cross-relaxation processes, i.e. the spin dynamic mechanism necessary to induce OE. In other words, the possibility of OE can be ruled out in the here presented simulation, as *e*-*n* ZQ and DQ cross-relaxation mechanisms were turned off. Notably, the TM DMP model utilizes the same underlying triple-flip mechanism as CE and truncated CE, but requires a different *e*-*e* coupling network. In contrast to the CE and truncated CE model that can be replicated with a *e*-*e*-*n* spin system, the TM model requires a minimum of three coupled e and one n. While in the truncated CE model the fast relaxing EPR component is broadened by g-anisotropy, in the TM model the fast relaxing EPR species is broadened by strong *e*-*e* (dipolar and/or exchange) coupling.[152]

Next, we tuned the spatial topology of the *e*-*e* coupling network by varying the *e*-*e* coupling strength among the electron spins using the g-anisotropy of the Trityl radical [81] to simulate the dispersive ^{1}H TM DNP frequency profile observed with Trityl. We found that we can deliberately alter the shape of the central feature of the TM DNP

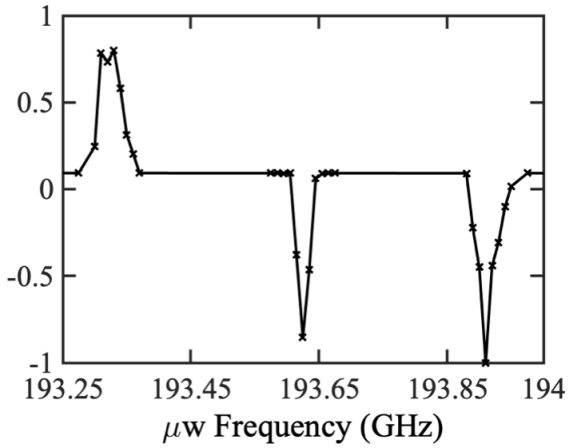

Figure 6.10: Simulated ^{1}H DNP enhancement as a function of μw irradiation frequency for a e_1-e_2-e_3-^{1}H spin system at 294 MHz conditions. G values of [2.0034 2.0031 2.0027] are used in simulating the negative-absorptive DNP profile envelope. e_2 and e_3 are strongly coupled (T_{1e} = 0.1 μs) while e_1 is less strongly coupled to e_2 or e_3 (T_{1e} = 5 ms). The ^{1}H is coupled only to e_1. The e-e dipolar couplings are: e_1-e_2 = 4 MHz, e_1-e_3 = 4 MHz, e_2-e_3 = 200 MHz.

frequency profile envelope. The T_{1e} values of the "visible" electron spin was set to 8 ms. We could replicate the dispersive shape for the central feature of the DNP profile (figure 6.9B) when setting the dipolar couplings between e_2-e_3 to 350 MHz ($r_{e_2e_3} = 5.29\mathring{A}$), e_1-e_2 to 15 MHz ($r_{e_1e_2} = 15.1\mathring{A}$), and e_1-e_3 to 5 MHz ($r_{e_1e_2} = 21.8\mathring{A}$) (schematically illustrated in the inset of figure 6.9B), which are higher values than the dipolar couplings used to simulate the positive absorptive TM frequency profile. Notably, a negative-absorptive (emissive) DNP field profile envelope was observed previously with deuterated BDPA by Griffin and coworkers.[145] The emissive envelope of the TM DNP feature could also be replicated with QM simulations (figure 6.10).

The minimum four-coupled spin model calculations illustrate that the electron spin polarization gradient and the corresponding TM DNP profile can display different shapes/ envelope with respect to the μw irradiation frequency. A more thorough quantum mechanical study, using a larger multi electron spin system and comprehensive explorations

of the various spin dynamics parameters, concurrent with experimental ELDOR investigations are needed to reach a deeper understanding as to how the topology of the *e*-*e* coupling network and the nature of asymmetry tunes the shape of the TM DNP field/frequency profile envelope. Investigating such dependencies will be an important future endeavour. In this study, we could show that TM is a dominant mechanism that generates the large enhancement around the BDPA center transition, while the exact and beneficial features of TM strongly depend on the spatial topology of the coupled multi-electron spin network, as reflected in the tuning of the different frequency profiles. The coupling network is modulated not only by the radical-radical, but also the radical-solvent interaction. Synthetic chemistry prowess (to tune the chemical interactions, i.e. the *e*-*e* coupling network) and further theoretical chemistry studies (to model the molecular dynamics and interactions) are indispensable in the pursuit of radical design to achieve efficient TM DNP with desirable attributes.

6.5 Conclusion

In summary, we propose the presence of TM DNP as an alternative explanation to the OE DNP hypothesis. This revelation is based on experimental EPR measurements that have been missing in recent analyses of DNP with BDPA, further supported by quantum mechanical simulations of the DNP profiles. Prediction of the effective DNP mechanism solely based on NMR measurements can be misleading, as the properties of the electron spin dynamics and the *e*-*e* coupling network are not fully apparent in NMR-based DNP measurements. A similar conundrum was solved in the discovery of the truncated Cross Effect.[152] The direct investigation of electron-spin dynamics by high-field pulsed EPR and pump-probe ELDOR measurement under DNP conditions was critical in revealing

the underlying mechanisms. The TM DNP observed in BDPA is fundamentally similar to the TM effect observed in Trityl-OX063, except with distinct shapes for the DNP μw frequency profile envelopes. The envelope shape of the TM DNP feature matters, in particular for its effectiveness under MAS conditions and broad-band μw irradiation. Quantum mechanical simulations revealed that the shape of this central DNP feature is dependent on the spatial topology of the e-e coupling network. However, this study also reveals that the study of TM DNP deserves more in-depth investigations. How do the microscopic events in DNP mesh with the macroscopic spin temperature arguments that traditionally underlie the discussion around TM? Clearly, CE, truncated CE and TM span a continuum, and this study shows that there are many different flavors of TM that can be exploited. Furthermore, this study has not investigated the effects of equilibration rates of the spin temperature of the electron non-Zeeman reservoir and that of the various coupled nuclear spin reservoirs. Here, we confirm the presence of TM DNP, and in principle leave open the question under what circumstances and for what types of samples OE may exist simultaneously. In the present study of BDPA as the DNP polarizing agent, it is impossible to directly deconvolute the contributions of OE and TM DNP enhancements (even if both were operating simultaneously) based on the field/frequency DNP profile alone. However, quantum mechanically speaking the efficiency of TM DNP mechanism will strongly depend on the magnitude of e-e coupling, and hence on PA concentration, while OE DNP does not require e-e coupling as it is primarily driven by the cross relaxation between a single electron spin with a proximal nuclear spins. Further experimental evidences are needed to clarify the role of OE in DNP using BDPA under cryogenic conditions. In parallel, a great deal of research is needed to quantify the TM DNP mechanism via EPR experiments, as well as seek an improved theoretical understanding and advance numerical simulation models for DNP.

Finally, we point out that the pioneering discoveries of Griffin and co-workers of the OE' effect not only inspired these studies, but the benefit of the originally discovered effects obviously holds. For example, the TM in BDPA has a positive enhancement shape where the enhancement will not be attenuated under fast MAS condition. Furthermore, the TM DNP effect can be deliberately tuned to be highly efficient at a wide range of temperatures, at high magnetic fields, under fast MAS rates and has low μw power requirements. Our own study presented here showed decent ^{1}H DNP enhancements using BDPA spin systems using moderate microwave powers. How to exactly exploit this effect is up to the PA and sample design to replicate the ideal electron and nuclear spin network that teases out the maximum benefit of TM DNP for the specific experimental conditions at hand.

Chapter 7

Solid-State MAS NMR at Ultra Low Temperature of Hydrated Bio-solids Doped with DNP Radicals

7.1 Introduction

Solid-state magic angle spinning (MAS) nuclear magnetic resonance (NMR) is an essential tool for the study of inorganic and biological solid samples. However, NMR has intrinsically low signal sensitivity, and hence instrument and method developments to enhance MAS NMR sensitivity are ongoing efforts. There have been many approaches to improve MAS NMR sensitivity, such as increasing the magnetic field B_0,[158, 159] lowering the sample temperature,[160, 161, 162, 163, 164] cooling the radio frequency (RF) circuitry,[**?**, **?**] applying efficient cross-polarization (CP) from abundant ^{1}H nuclear spins, shortening the experimental repetition time by adding paramagnetic dopants [58, **?**] and by hyperpolarization techniques, most commonly, dynamic nuclear polarization (DNP).[160, 161, 162] Performing DNP enhanced MAS NMR at high B_0 integrated

with ultra low temperature (ULT, $\ll$ 100 K) sample cooling would yield great signal sensitivity by potentially several thousand of folds compared with room temperature MAS NMR at the same field. However, there are many theoretical and technical complexities in building such a system, where achieving ULT is one of the biggest challenges. Moreover, NMR signal line broadening and increasing nuclei spin lattice relaxation time (T_1) are among the biggest concerns in performing ULT NMR experiments.

The minimum sample temperature largely depends on the cooling gas used in the MAS NMR system. Generally speaking, three types of gases have been used to achieve low temperature NMR: 1) dried air ($\sim$ 250 K to room temperature); 2) nitrogen cooled to liquid nitrogen temperature ($\geq$ 77 K); 3) helium cooled by compressors and/or liquid helium ($<$ 77 K). MAS NMR cooled by dried air or cold nitrogen gas has been used to study the structural properties of vitrified proteins in solution and trapped transient states of proteins.[160, 165, 166, 167] However, there is still a large demand in pushing the sample temperature down to the ULT regime. An ideal ULT MAS NMR system achieves stable low temperature and stable MAS with little helium consumption, is easy to operate and requires little maintenance effort, has a broad accessible temperature and MAS range, and is efficient in cooling and exchanging samples.

There have been persistent endeavors in the development of helium cooled systems to achieve ULT NMR/DNP. The journey began in the 1980s when Yannoni and co-workers successfully conducted the ^{13}C CP-MAS NMR experiments at ULT on several organic molecules and polymers using cold helium gas directly warmed up from liquid helium for spinning and cooling.[168, 169] A maximum sample spinning speed of 2.5 kHz and a minimum sample temperature of 4.2 K was achieved with a large liquid helium consumption rate (15 L/h at 30 K with 1 kHz MAS). In 1997, the Griffin group at MIT adapted

the Yannoni design and combined the ULT NMR with DNP capabilities at 5 T. [160] A significant increase in the DNP enhancement was achieved at 25 K (∼100) compared with 100 K (∼ 5). New designs and optimizations have been implemented to further push this field forward. Samoson *et al*. customized a ULT MAS NMR system located in Tallinn to allow ≤ 20 kHz MAS at ≥ 7 K with a 2 mm rotor. [170] In the Tallinn design, helium is used in all three gas lines (bearing, drive, and VT), and is later recovered and recycled. The main problem for the Tallinn design is that the stability is limited and the sample temperature is strongly coupled to the spinning speed. The Levitt group provided another design in Southampton using super-critical helium in a pressurized vessel for the three gas lines. [171] The super-critical helium avoids the instability caused by the inherent two-phase flow of liquid helium. This design allowed a minimum sample temperature of 9.6 K with 15 kHz MAS using a 2 mm rotor. However, the current operation of the Southampton system, especially the super-critical helium generator, is very expensive due to large demand for liquid helium ∼5000 L. The Barnes group customized their own cryostat in order to integrate with versatile MAS DNP probes and rotor designs. The Barnes design uses liquid helium for cooling and spinning with still a large liquid helium consumption rate of ∼33 L/h to achieve sample temperatures of <6 K. [163] The Tycko group in Bethesda (NIH) has provided a new approach, where cold helium gas is used only for cooling the sample and cold nitrogen gas is used for spinning. This design allowed significant reduction in the liquid helium consumption rate of about 3 L/h and enabled MAS-DNP experiments at 20 K with ∼7 kHz MAS for a 4 mm rotor.[162] This design was later commercialized by Revolution NMR LLC and installed in the Han group at UC Santa Barbara.[45]

In order to further reduce the helium consumption rate, closed-cycle helium systems were designed and used to recover the helium used for cooling and spinning. The De

Paëpe group at Grenoble designed a ULT MAS DNP system equipped with a helium circulation system and has achieved up to 15 kHz MAS at 30 K using a 3.2 mm rotor.[164, 172] A spinning stability of 7 kHz ±50 Hz was measured at 50 K.[164] In this design, the cryostat was initially cooled down to ∼80 K using liquid nitrogen. To achieve temperatures < 77 K, the cryostat was flushed with room temperature helium gas and then cooled using cold helium gas directly boiled off from liquid helium Dewar. NMR/DNP probes are further cooled using recirculated pressurized bearing, drive and VT helium gases cooled by the cryostat. The helium gas consumption rate for the Grenoble design is $\ll 1$ L/h for both the leaks and pneumatic rotor insertion/ejection. However, the current Grenoble design still consumes liquid helium at a relatively high rate of 5-25 L/h depending on the desired sample temperature and MAS. The next generation of fully autonomous system with zero liquid helium consumption is under testing. Another closed-cycle helium circulation ULT NMR/DNP design has been introduced by the Fujiwara group in Osaka, where cold helium gas is used for bearing and drive (no VT in the design).[173] It is worth noting that the Osaka design doesn't use liquid helium, which is a big improvement from all the other designs mentioned above. In the Osaka design, helium gas was initially cooled by vacuum insulated heat exchangers for both bearing and drive. The cold helium gas is pressurized by bellows compressors and the precise flow rates are further regulated using mass flow controllers. The regulated helium gas is then used for sample cooling and spinning. Afterwards, the return helium gas is still cold and is used in the initial cooling step through a tube-in-tube type counter-flow heat exchanging system. This system has shown great stability in sample temperature and spinning, where up to of 8 kHz of stable MAS at 20 K has been reported with ± 5 Hz MAS variations for days of testing using a 3.2 mm rotor.[161] In 2020, JEOL RESONANCE Inc. has commercialized the Osaka design and launched its first installation in collaboration with the Han group at UC Santa Barbara.

ULT has allowed large NMR signal sensitivity gain from both the Boltzmann factor and the general increase in the quality factor (Q) as well as the reduction of the Johnson-Nyquist noise (thermal noise) for the RF circuit. In addition, the capabilities of ULT MAS NMR can offer more profound scientific benefits. For example, through measuring the ^{63}Cu NMR quadrupolar broadening and spin-spin lattice relaxation rates at 90-10 K, Krämer and Mehring observed that the superconductor $YBa_2Cu_3O_{7\delta}$ transformed into an ordered charge density wave state at < 35 K.[174] In addition, ULT MAS NMR has been attracting interests for biomolecular systems in which the NMR signal sensitivity may be improved with the slowed down molecular motion of methyl group rotation.[175, 165, 161] Ni *et al*. reported that $^{13}CH_3$ and $^{15}NH_3$ signals in MAS spectra of biological samples disappear due to the interference of the molecular motions with ^{1}H decoupling in the temperature range of 110-80 K.[165] Moreover, such methyl group rotations may also hamper the DNP efficiency, especially for samples where the ^{1}H-^{1}H spin diffusion is limited by really short ^{1}H DNP $T_{buildup}$ (e.g. 1.8 s at 86 K) such as crystalline samples with high methyl-bearing density.[161] Matsuki *et al*. recently showed a DNP enhancement of 15-fold at 27 K with a high methyl-bearing NMR standard sample MLF (N-formyl-Met-Leu-Phe-OH), while almost no enhancement was observed at 100 K.[161] As almost half of the proteinogenic amino acids contain CH_3 or NH_3 groups in their side chain, ULT NMR and DNP have the potential to offer dramatic improvements for the MAS NMR studies of protein samples.

In this chapter, we examined the newly installed JEOL ULT closed-cycle helium MAS NMR system and reported on the helium consumption, cooling efficiency, sample temperature stability and MAS stability. MAS NMR performance was also examined at ULT of a methyl-bearing NMR standard [U-^{13}C]alanine dissolved in a water/glycerol glassy ma-

trix doped with paramagnetic centers. The ^{1}H NMR spectra exhibited the benefit from the enhanced Boltzmann factor at ULT. The impact of different paramagnetic centers is also examined through ^{1}H spin-lattice relaxation and spectral linewidth measurements at variable temperatures.

7.2 Methods

1 mg of ^{13}C uniformly labeled Alanine ([U-^{13}C]alanine, Sigma Aldrich) was added in 30 μL DNP Juice (d_8-glycerol/D_2O/H_2O = 6/3/1, v/v/v), resulting in a concentration of 375 mM [U-^{13}C]alanine, note as Ala in the following text. The solution was then doped with paramagnetic centers, including 10 mM AMUPol (CortecNet), 10 mM TEMTriPol-1, 20 mM 4-Amino TEMPO (Sigma Aldrich), and 14.3 mM Gd-DOTA (Macrocyclics). 30 μL solution was then packed in the center of a 3.2 mm Si_3N_4 rotor using Kel-F spacers. One of the Kel-F spacers was packed with KBr for temperature calibration. In this paper, all the reported temperatures are calibrated by measuring the spin lattice relaxation time of ^{79}Br in KBr,[176] unless mentioned otherwise. Specially designed Vespel caps with Dyneema fiber reinforced plastic inserts that expand at low temperatures were used to ensure the tightness of the caps at low temperatures and easy removal at room temperature.[177, 178]

ULT NMR experiments were conducted using a 600MHz ECZ600R solid-state NMR spectrometer equipped with a closed-cycle helium MAS system (JEOL RESONANCE Inc.). A CH double-resonance ULT MAS NMR probe was used for NMR experiments and was cooled by the heat exchanger (figure 7.1). The Q-factors of the ^{1}H and ^{13}C coils were measured at variable temperatures (room temperature to 30 K) and are reported

in table 7.1. The nutation frequencies of the ^{1}H and ^{13}C channels were also measured at different temperatures (100-26 K) and are recorded in table 7.2. All the NMR experiments shown in this paper are conducted with an MAS of 7 kHz, unless mentioned otherwise. Further evaluations of the system can be found in the instrumentation section.

Pulse sequences used for NMR experiments are shown in figure 7.2. ^{1}H NMR signal was measured after a direct $\pi/2$ pulse (figure 7.2A). A buildup time of $D_1 = 7$ s was used unless mentioned otherwise. ^{13}C CP-MAS experiments were acquired using the pulse sequence shown in figure 7.2B. In ^{13}C CP-MAS experiments, buildup time $D_1 = 7$ s was applied and Spinal64 ^{1}H decoupling pulse with > 80 kHz decoupling power was used.

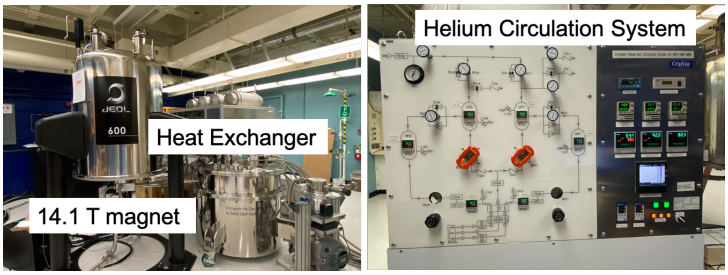

Figure 7.1: Left: Picture of the 14.1 T JEOL magnet and the heat exchanger unit. Right: Picture of the helium circulation unit.

Table 7.1: Q-factor of ^{1}H and ^{13}C RF Coils

Temperature (K)	RT	80	30
^{1}H Q-factor	243	468	709
^{13}C Q-factor	134	269	358

Table 7.2: Nutation Frequencies of ^{1}H and ^{13}C RF

Temperature (K)	98	85	70	60	50	40	26
^{1}H RF 35 W (kHz)	104.2	104.2	108.7	113.6	113.6	119.0	125.0
^{13}C RF 36 W (kHz)	56.8	58.1	59.5	59.5	62.5	62.5	65.8

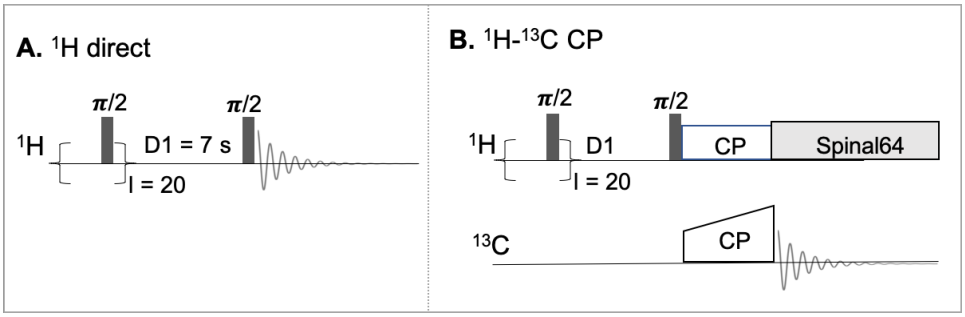

Figure 7.2: NMR pulse sequence for A. ^{1}H direct detection, B. ^{13}C CP-MAS.

7.3 Results and discussion

7.3.1 ^{1}H NMR

A typical hydrated bio-solid sample prepared for ULT NMR/DNP contains target samples, a glassy matrix, and paramagnetic centers as is shown in figure 7.3A. In this study, a typical glassy matrix, DNP Juice (d_8-glycerol/ D_2O/ H_2O = 6/3/1, v/v/v), was used mainly for three purposes: 1) protect the sample at freezing conditions, 2) dissolve the paramagnetic centers, and 3) provide a spin diffusion network for future ULT DNP studies. We chose two bi-radicals, AMUPol and TEMTriPol-1, as the paramagnetic centers. The chemical structure of AMUPol and TEMTriPol-1 can be found in figure 7.3B and 7.3C, respectively. The main purpose of doping the bi-radicals is to enhance the nuclear longitudinal relaxation time (T_1) for cutting down the experimental repetition time. The effects of relaxation enhancement will be discussed in later sections.

One of the major benefits of operating NMR at ULT comes from the Boltzmann dis-

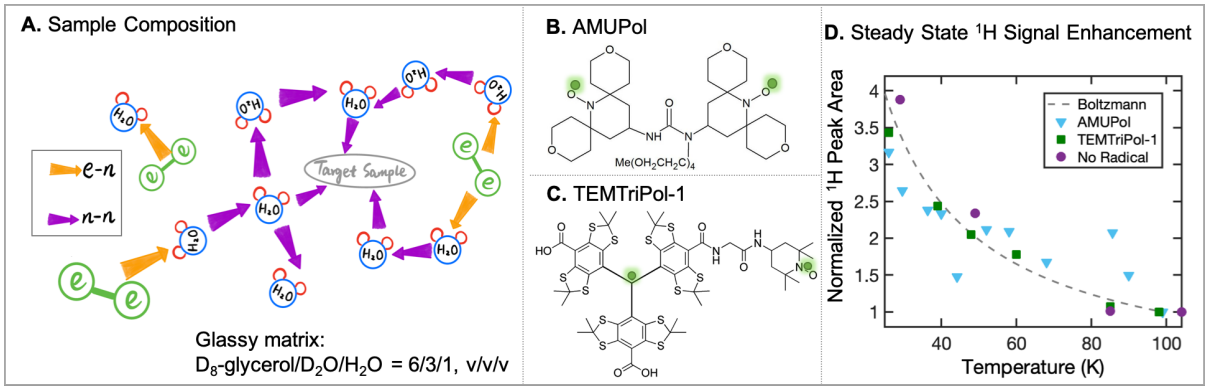

Figure 7.3: A. Sample composition. Electrons (e) in the bi-radicals, oxygen in H_2O, ^1H nuclei in H_2O, and target sample are represented in green, blue, red, and grey, respectively. *e-e* couplings, e-n couplings, and n-n couplings are marked in green lines, yellow arrows, and purple arrows, respectively. B. AMUPol chemical structure (e is highlighted in green). C. TEMTriPol-1 chemical structure (e is highlighted in green). D. Steady state ^1H signal intensity, normalized by what was achieved at 100 K, was plotted as a function of temperature. ^1H signal was measured with hydrated Ala samples doped with 10 mM AMUPol (blue), 10 mM TEMTriPol-1 (green), and no radicals (purple). Signal enhancement from Boltzmann factor is calculated and plotted as the dashed grey line.

tribution favored at low temperature, noted as the Boltzmann factor in the paper. We started our investigation by measuring the ^1H NMR signal intensity in order to confirm the benefits of Boltzmann factor at ULT.

The steady state ^1H NMR signal of the sample was calculated to be the area of the ^1H signal at $5 \times T_1$, where the following equation was used:

$$Area_{Steady} = Area_{D_1} \times \frac{C_1 - C_2 \times exp(-5 \times T_1/T_1)}{C_1 - C_2 \times exp(-D_1/T_1)} \tag{7.1}$$

In the equation, $Area_{steady}$ is the calculated NMR signal area at the steady state and $Area_{D1}$ is the measured signal area with $D_1 = 7$ s. $C_1 - C_2 \times exp(-\tau/T_1)$ is obtained through fitting the saturation recovery experiment at the corresponding temperature, where C_1 and C_2 are constants. Figure 7.3D shows the temperature-dependent steady

state ^{1}H signal area normalized by what was measured at 100 K. The dashed grey line is the ^{1}H NMR signal sensitivity gain calculated from the Boltzmann factor. Normalized steady state ^{1}H NMR signals for the hydrated bio-solid samples doped with 10 mM AMUPol, 10 mM TEMTriPol-1, and no radical are plotted as blue, green, and purple, respectively. Overall, from 100 K to 25 K, the steady state ^{1}H NMR signal enhancements for the three samples follow the Boltzmann factor, where a signal intensity gain of $\sim$ 400 % is obtained at 25 K compared with 100 K.

To be noted, the RF circuit's quality factors (Q) also contribute to the ULT NMR sensitivity enhancement as NMR signal sensitivity is proportional to $\sqrt{Q}$.[?] With the current probe, a sensitivity improvement could be achieved by a factor of 1.71 for ^{1}H and 2.67 for ^{13}C at 30 K compared to at room temperature (table 7.1). However, the current ^{1}H NMR sensitivity enhancement is lower than the product of Boltzmann factor and Q factor gains at ULT, of which the reason is not fully understood. In addition, the noise levels did not change significantly because the thermal noise from the RF coil is not a major factor compared to the noise from the room-temperature preamplifier. For future development, adding and cooling a preamplifier in the probe will increase signal-to-noise ratio considerably.

7.3.2 ^{13}C CP-MAS

We then examined the benefit of ULT for ^{13}C CP-MAS experiments, especially for bio-solids that are highly methyl-bearing. Here Ala (figure 7.4A) was chosen to probe the influence of ULT NMR on samples with CH_3 groups. The paramagnetic center we used for this series of studies was 10 mM AMUPol.

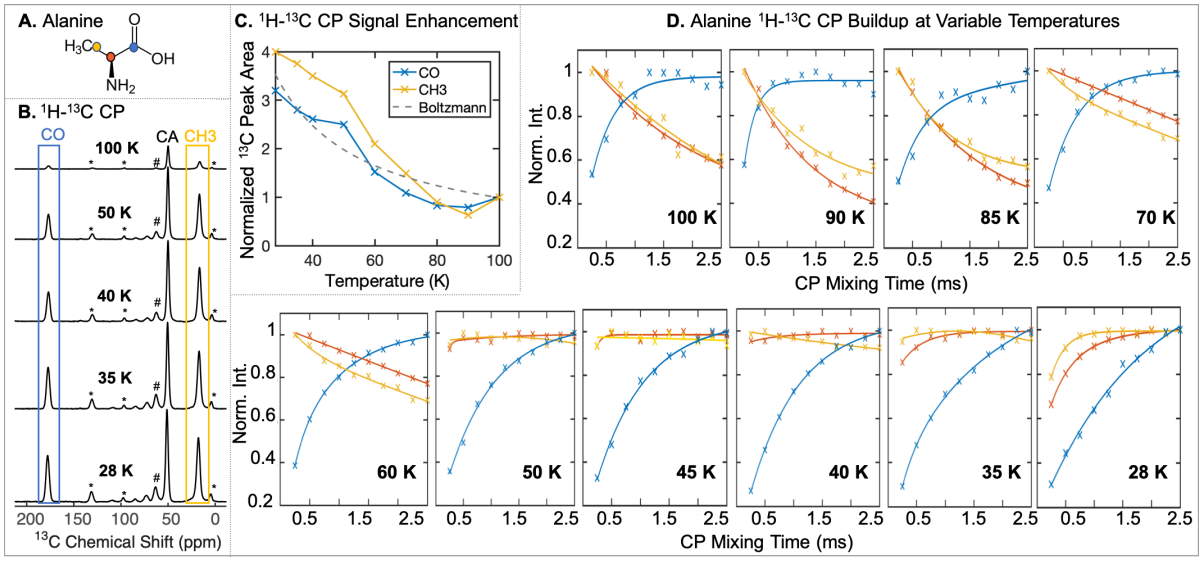

Figure 7.4: A. Chemical structure of Alanine, where the CO, CA, and CH_3 are marked with blue, red, and yellow circles, respectively. B. ^{13}C CP-MAS spectra of Ala from 100 K to 28 K. Spinning side bands are marked in * and solvent glycerol peaks are marked in #. C. ^{13}C CP-MAS CO and CH_3 peak area measured at variable temperatures. CP mixing times are optimized for CO and CH_3 separately. D. Normalized signal intensities for CO, CA, and CH_3 as a function CP mixing time at variable temperatures (from 100 K to 28 K). The solution was doped with 10 mM AMUPol.

Figure 7.4B displays the ^{13}C CP-MAS spectra of Ala measured at variable temperatures from 100 K to 28 K. A decrease in the signal intensities for all the three ^{13}C sites in Ala is observed as temperature goes down from 100 K to 28 K. Figure 7.4C displays the signal area of the CO (blue) and CH_3 (yellow) peaks at variable temperatures from 100 K to 28 K, where the signal intensities are normalized to what was acquired at 100 K. Signal enhancement due to the Boltzmann factor is also plotted as the grey dashed line. We observed that lowering the temperature from 100 K to 28 K leads to signal enhancement by 400% for the ^{13}C in the CH_3 group, which is notably higher than the increment in the Boltzmann factor (357%). In contrast, the ^{13}C in the CO group shows a similar signal enhancement at 28 K compared to the Boltzmann factor. We ascribe the large signal enhancement in the methyl group ^{13}C at 28 K to the improved efficiency of the

CP-MAS due to reduction in methyl proton hopping rate. In addition, a drop in signal intensity $\sim$ 80 K was observed for both CO and CH_3 sites. This was previously observed and discussed by Ni *et al.*, where the signal reduction is attributed to the methyl group dynamics interfering with ^{1}H decoupling around 110-80 K. [165]

^{13}C CP-MAS experiments of methyl-bearing bio-solids also benefit from the choice of CP mixing time. A series of temperature-dependent Ala ^{13}C sites' signal intensities was recorded as a function of CP mixing time and is displayed in figure 7.4D. The signals from CO, CA, and CH_3 sites are shown in blue, red, and yellow crosses, respectively. At 100 K, the optimum CP mixing time for the CO site is 2.5 ms while the signals for CA and CH_3 sites already started decreasing with the mixing time greater than 0.5 ms. As temperature decreased to 28 K, the optimum CP mixing time for all three sites has increased. In addition, signals for CA and CH_3 sites did not decrease with long CP mixing time up to 2.5 ms. In general, the optimum CP mixing times for CO are much longer than for CH_3 due to the weaker ^{1}H-^{13}C coupling in the former case. However, under the long spin-lock pulse required for CP, the methyl protons tend to relax due to their faster relaxation rates in the RF frame ($T_{1\rho}$) at 100 K. Thus, a compromise between optimum CP for CO and methyl carbons has to be made typically at temperatures $>$ 50 K. At ULT, this issue is resolved because the methyl protons hopping rate is significantly slowed down.[175]

In conclusion, operating ^{13}C CP-MAS of high methyl-bearing sample at ULT has major three benefits. First, NMR signal intensity benefits from the Boltzmann factor and Q as temperature goes down. Second, methyl group dynamics have been greatly impaired at temperatures below 50 K, providing higher CP efficiency. Third, optimum CP for both methyl group and non-methyl group carbons can be achieved with long CP mixing time at ULT while a compromise has to be made at higher temperatures.

7.3.3 ^{1}H T_1

Table 7.3: ^{1}H T_1 at variable temperatures measured using ^{13}C CP-MAS saturation recovery

Temperature (K)	RT[a]	100[b]	100	85	50	30
No Radicals (s)	1.6	-	93.5	93.6	85.2	254.7
10 mM AMUPol (s)	-	4.1	5.1	5.6	5.7	5.6
10 mM TEMTriPol-1 (s)	-	1.8	2.3	2.4	2.6	3.2
20 mM 4-Amino TEMPO (s)	-	-	13.5	21.1	26.0	31.8
14.3 mM Gd-DOTA (s)	-	-	5.2	6.2	7.7	12.8

a: Measured for [U-^{13}C]alanine crystal packed in a 1 mm rotor under 600 MHz JEOL NMR. MAS was 7 kHz.
b: Measured using a 3.2 mm HX probe under 400 MHz Bruker DNP-NMR spectrometer. MAS was 7 kHz.

T_1 is another important factor that determines the signal per unit time. At ULT, some samples can have very long T_1, leading to long experimental repetition time and low sensitivity. Generally paramagnetic centers are added to reduce the T_1. In this study, AMUPol, TEMTriPol-1, 4-Amino TEMPO, and Gd-DOTA were examined to reveal the plausible mechanism of nuclear T_1 relaxation enhancement. ^{1}H T_1 was measured through ^{13}C CP-MAS experiments and the fitted values are recorded in table 7.3.

Without any radical addition, ^{1}H T_1 increased significantly from 93.5 s to 254.7 s when temperature was cooled down from 100 K to 30 K. ^{1}H T_1 of [U-^{13}C]alanine solid crystals at room temperature was also provided as a reference. With 10 mM AMUPol addition, ^{1}H T_1 has been significantly shortened to $\sim 6 \pm 1$ s compared with no radical addition. One of the popular mechanisms for explaining the T_1 relaxation enhancement is the Paramagentic Relaxation Enhancement Effect (PRE). According to PRE theory, the

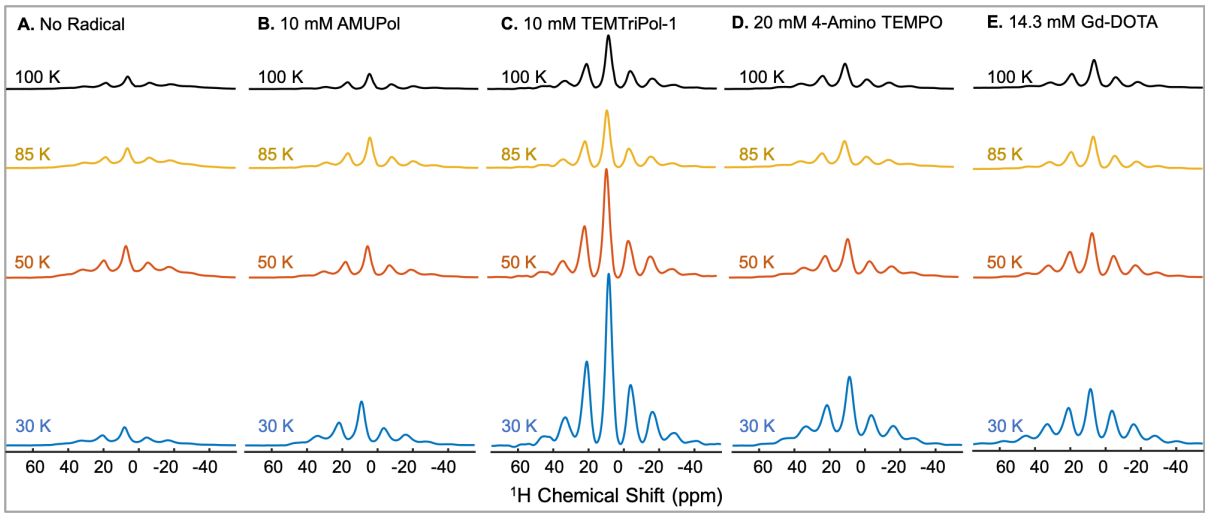

Figure 7.5: ^{1}H NMR spectra of the solvent ^{1}H measured at 100 K (black), 85 K (yellow), 50 K (red) and 30 K (blue). 7 s buildup time was used for all the displayed spectra. Different relaxing agents are used in the solvents: A. no radicals, B, 10 mM AMUPol, C: 10 mM TEMTriPol-1, D: 20 mM 4-Amino TEMPO, and E: 14.3 mM GdDOTA.

nuclear relaxation was enhanced by providing an external magnetic field fluctuation near the nuclear sites. In solids, the PRE rates are given by Solomon-Bloembergen-Morgan (SBM) expressions, where the equations can be found below:

$$\frac{1}{T_{1,PRE}} \approx \frac{2}{15}\left(\frac{\mu_0}{4\pi}\right)\frac{\gamma_n^2 g_e^2 \mu_B^2 S(S+1)}{r^6}\left(\frac{3\tau_{c1}}{1+\omega_n^2\tau_{c1}^2} + \frac{7\tau_{c2}}{1+\omega_e^2\tau_{c2}^2}\right) \tag{7.2}$$

$$\frac{1}{\tau_{c1}} = \frac{1}{T_{1e}} + \frac{1}{\tau_r} + \frac{1}{\tau_M} \tag{7.3}$$

$$\frac{1}{\tau_{c2}} = \frac{1}{T_{2e}} + \frac{1}{\tau_r} + \frac{1}{\tau_M} \tag{7.4}$$

From the equations, it is known that efficiency of PRE is related to many factors, such as the paramagnetic dopant concentration reflected in the e-n distance r, spin angular momentum (S), e relaxations rates (T_{1e} and T_{2e}), rotational motions (τ_r), and chemical

exchange rate (τ_M). In addition to PRE, there is another possible relaxation enhancement mechanism involved in the AMUPol radical, where the $\alpha_e\beta_e\alpha_n$ and $\beta_e\alpha_e\beta_n$ states flip simultaneously during energy level crossings addressed as triple-flip in this paper. This triple-flip driven T_1 enhancement was first discussed by Houten *et al.* in 1977.[179] They observed a significant decrease in the ^{1}H T_1 time of the (Cu,Zn)$Cs_2(SO_4)_2{\cdot}6(H,D)_2O$ crystal whenever the rotating crystal orientation provided EPR frequencies that matched the simultaneous triple-flip condition $\omega_{e1} - \omega_{e2} = \omega_{1H}$. Such a matching condition is also the resonance condition for Cross Effect (CE) DNP. The triple-flip driven nuclear relaxation enhancement mechanism was later investigated by Leavesley *et al.*, where ^{1}H T_1 was measured for glycerol-water mixture doped with a series of mono-, bi-, tri-, and dendritic-nitroxide radicals.[29] They observed that a stronger *e*-*e* coupling can lead to a shorter solvent ^{1}H T_1.

In order to verify the T_1 enhancement mechanism, we measured the ^{1}H T_1 of hydrated Ala sample doped with a mono-nitroxide radical, 20 mM 4-Amino TEMPO. Such a system was chosen as a comparison to the 10 mM bi-nitroxide radical AMUPol, where the 20 mM global e spin concentration was maintained. Overall, the ^{1}H T_1 of sample doped with 4-Amino TEMPO is much longer than with AMUPol, indicating that *e*-*e* coupling is important in the mechanism that relaxes ^{1}H T_1 with bi-radical addition. Since the conventional definition of PRE doesn't include the *e*-*e* coupling term (SBM expressions in SI), we can already conclude that the triple-flip mechanism is playing a significant role in the ^{1}H T_1 enhancement. More importantly, ^{1}H T_1 in solvent doped with 4-Amino TEMPO increased significantly from 13.5 s to 31.8 s as the temperature cools down from 100 K to 30 K while ^{1}H T_1 remains similar when AMUPol was added. This observation can be explained by the theory of PRE and triple-flip in CE DNP, where the temperature dependent e relaxation rates have a large impact on PRE efficiency but very little impact

on the simultaneous triple-flip.

A typical PRE agent Gd-DOTA was also examined to further explore the benefit of using the triple-flip mechanism for nuclear T_1 enhancement rather than simply using PRE. It is already established that the solvent T_1 depends on the Gd-DOTA concentration. Based on the study from Ullrich *et al.*, 14.3 mM Gd-DOTA would result in a ^{1}H T_1 reduction of 88.4 s [180], resulting a ^{1}H T_1 of 5.1 s at 100 K ($93.5s - 88.4s = 5.1s$) in our system theoretically. Experimentally, we measured a 5.2-s ^{1}H T_1 of sample doped with 14.3 mM Gd-DOTA at 100 K. As temperature goes down to 30 K, the ^{1}H T_1 has increased to 12.8 s, longer than what was measured for sample doped with AMUPol (5.6 s). This observation further strengthened the argument that the triple-flip drive relaxation enhancement mechanism could potentially be better than conventional PRE, as the triple-flip mechanism has shown lower temperature dependence.

We further explored the relationship between the efficiency of triple-flip mechanism itself and the nuclear T_1 enhancement. ^{1}H T_1 of sample doped with 10 mM TEMTriPol-1 radical was measured to be only 2.3 s at 100 K, even shorter than what was measured with AMUPol. The ^{1}H T_1 only increased to 3.2 s upon cooling down to 30 K. With the commercial Bruker 400 MHz DNP-NMR system, ^{1}H T_1 measured with 10 mM TEMTriPol-1 is only 1.8 s at 100 K, still much shorter than what was measured with AMUPol (4.1 s). It is known that the efficiency of triple-flip in TEMTriPol-1 radical is higher than that of AMUPol as simulated by Equbal *et al.*.[181] Our observation suggests that higher triple-flip efficiency can enhance the T_1 relaxation more.

Next, we compared the ^{1}H NMR signals of all the five samples, shown in figure 7.5. The set of experiments was acquired using $D_1 = 7$ s and 4 scans. This comparison takes

into account of all the factors that can enhance/attenuate NMR signal intensity, such as Boltzmann factor, Q factor, T_1, paramagnetic quenching,[**?**] and the depolarization effect.[45] Among all the samples, Ala solution doped with TEMTriPol-1 has the highest NMR signal intensity across a large range of temperatures from 100 K to 30 K. This observation suggests that TEMTriPol-1 is not only a radical that can provide high CE DNP enhancement[25, 81] but also a good nuclear T_1 relaxing agent with less impairment in the NMR signal.

7.3.4 Spectral linewidth

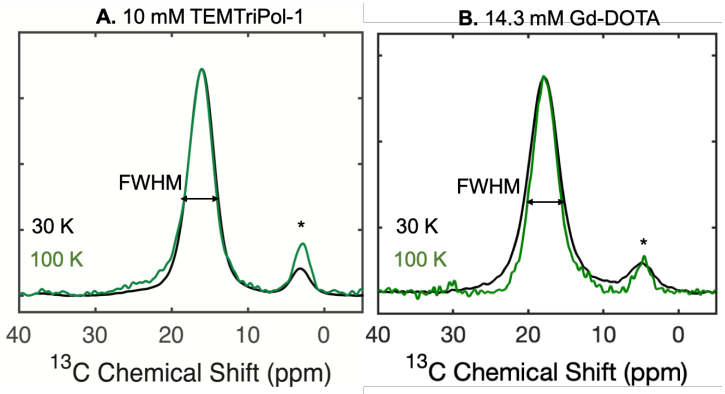

Figure 7.6: ^{13}C CP-MAS of CH_3 in Ala measured at 30 K (black) and 100 K (green) with the addition of paramagnetic centers: A: 10 mM TEMTriPol-1, B: 14.3 mM Gd-DOTA. The spinning side bands were marked in *.

Spectral resolution is another critical factor in bio-solid NMR applications. In this paper, spectral resolution is reflected by the full width at half maximum (FWHM) of the CH_3 peak measured using ^{13}C CP-MAS, as recorded in table 7.4. Without radical addition, as temperature decreases from 100 K to 30 K, FWHM of ^{13}C signal in CH_3 increases from 3.3 ppm to 3.9 ppm. The significant increase of FWHM to 4.3 ppm at 85 K results from interference between the methyl group rotation frequency and ^1H decou-

Table 7.4: CH_3 Peak Full Width at Half Maximum (FWHM) at Variable Temperatures Measured Using ^{13}C CP-MAS (20 Hz line broadening was applied)

Temperature (K)	100[a]	100	85	50	30
No Radicals (ppm)	-	3.3	4.3	3.7	3.9
10 mM AMUPol (ppm)	4.7	3.8	4.5	3.8	4.0
10 mM TEMTriPol-1 (ppm)	4.6	3.7	4.5	3.7	4.0
20 mM 4-Amino TEMPO (ppm)	-	3.6	3.8	3.9	4.2
14.3 mM Gd-DOTA (ppm)	-	4.0	4.9	4.4	4.8

a: Measured using a 3.2 mm HX probe under 400 MHz Bruker DNP-NMR spectrometer. MAS was 7 kHz.

pling, as already discussed previously.[165] With the addition of 10 mM AMUPol, at 100 K the FWHM increases by 0.5 ppm compared with no radical addition, while at 30 K FWHM only increases by 0.1 ppm. Compared with that of no radical addition, the line broadening with the addition of 10 mM AMUPol is insignificant at 30 K.

With the addition of 10 mM TEMTriPol-1, FWHM values are similar to that of 10 mM AMUPol. This suggests that the increase in the triple-flip efficiency does not increase the spectral linewidth further. However, with the addition of 20 mM 4-Amino TEMPO, FWHM increases from 3.6 ppm to 4.2 ppm from 100 K to 30 K, which is much larger compared with that of no radical addition. The increase in linewidth at ULT is even more severe with doping the PRE agent Gd-DOTA, where the FWHM has increased from 4.0 to 4.8 ppm. Figure 7.6 shows the overlaid normalized ^{13}C CP-MAS spectra of CH_3 in Ala measured at 30 K (black) and 100 K (green), where the effects of line broadening doped with TEMTriPol-1 (figure 7.6A) or with Gd-DOTA (figure 7.6B) are compared side by side. The spectral linewidth of the CH_3 peak has a much more significant increase when doped with Gd-DOTA compared with TEMTriPol-1. This observation suggests that the PRE agent might cause more severe line broadening compared with triple-flip radicals,

which is another great advantage of using triple-flip radicals as the paramagentic centers for ULT NMR experiments. However, more rigorous examinations are required to understand the line broadening effects from PRE and triple-flip mechanism.

7.4 Conclusion

In conclusion, the JEOL closed-cycle helium MAS system has allowed efficient cooling and stable spinning (tested from 1.5 kHz to 12 kHz) under variable temperatures (tested from 25 K to 105 K) with little helium consumption. Using this system, we have systematically examined the ULT NMR properties of a hydrated bio-solid, [U-^{13}C]alanine (Ala) dissolved in d_8-glycerol/D_2O /H_2O (DNP Juice) solution doped with paramagnetic centers. Steady state ^{1}H NMR signal at ULT has shown a similar signal intensity increment compared with the Boltzmann factor. ULT NMR benefits signal sensitivity through many aspects: Boltzmann factor, increasing in the quality factor of the RF circuitry as well as the reduction of spin dynamics such as methyl group rotation. At 28 K, ^{13}C CP-MAS signal for the methyl ^{13}C in Ala has achieved a signal enhancement of 400% compared with signal at 100 K, which is higher than the contribution from the Boltzmann factor (357%). This signal enhancement was ascribed to the improved efficiency of the CP due to reduction in methyl proton hopping rate. In addition, at ULT, an optimum CP mixing time can be chosen to achieve high CP efficiency for both CO and CH_3 carbons while a compromise has to be made at higher temperatures (> 50 K).

It is also worth noting that the choice of paramagnetic centers can significantly influence the nuclear T_1 relaxation enhancement. ^{1}H T_1 has shorten significantly from 254.7 s to 3.2 s at 30 K with the addition of 10 mM TEMTriPol-1, a radical known to provide

efficient Cross Effect (CE) DNP enhancement at high field and under fast magic angle spinning. The efficient T_1 relaxation enhancement using TEMTriPol-1 is due to not only the paramagnetic relaxation enhancement (PRE) effect but also the triple-flip driven relaxation enhancement. The higher efficiency of the triple-flip can result in greater nuclear T_1 relaxation enhancement. More importantly, the linewidths of the ^{13}C CP-MAS spectra for Ala doped with triple-flip radicals are not further impeded at ULT compared with that at 100 K, suggesting that the prospects for NMR and DNP under ULT conditions are highly promising. This observation provides a promising design principle for future nuclear relaxation enhancement radical development. The developed radicals with efficient triple-flip can also be a good candidate for future CE DNP applications.

Chapter 8

Prospective DNP Applications in Inorganic and Biological Materials

8.1 Revealed Minor Species of Surface Silanol Groups on Silica Nano-particles

Silica nano-particle plays an important role in heterogeneous catalytic systems, due to its tunable surface properties by thermal treatment and chemical modification. During calcination, silanol groups (-SiOH) of silica nanoparticles on nearby silica sites undergo dehydration to form siloxane groups (-Si-O-Si-). There are four kinds of sites on silica surface, termed Q1, Q2, Q3, and Q4, corresponding to the number of silanol groups decreasing from three to zero. With DNP enhanced NMR, we revealed that silica nanoparticle after calcined at high temperatures of 1000 C can surprisingly still undergo rehydration and form Q1 surface species (figure 8.2). This Q1 species is only $\sim 1\%$ of the total surface sites meaning that the NMR active Q1 species is only 0.05% of the total surface sites (^{29}Si natural abundance is only 4.67%). Such a minor amount of Q1 species

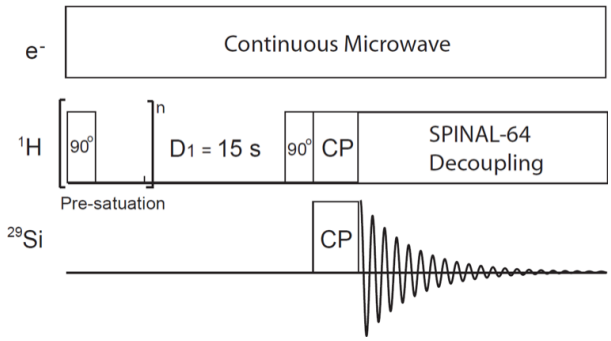

Figure 8.1: ^{1}H-^{29}Si cross polarization (CP) pulse sequence used for quantification of the Q1 species on the silica surface.

could only be probed due to the sensitivity enhancement of the NMR signal though DNP.

8.2 Probe Tau Amyloid Fibrils Self-Assembly Intermediates

Tau aggregation is involved in many neurodegenerative diseases, such as Parkinson's and Alzheimer's diseases. Although the structure of tau aggregate has been solved using cryo-EM and solid-state NMR,[182, 183, 184] the aggregation pathway is still elusive. While understanding this pathway is indispensable for understanding Tauopathies, probing protein self-assembly intermediates is a big challenge. Using DNP enhanced NMR at ultra low temperature, Tycko's group in NIH has successfully captured a protofibrillar stage before Amyloid-β(Aβ) fibril formation.[185] However, Tau aggregation is more complicated than the Aβ case as the full-length Tau peptide is around 10 times larger than Aβ and it is an intrinsically disordered protein, making it difficult to obtain homogenous Tau fibrils as the first step.

Thus, the first stage of the project is to obtain homogeneous Tau fibrils in vitro con-

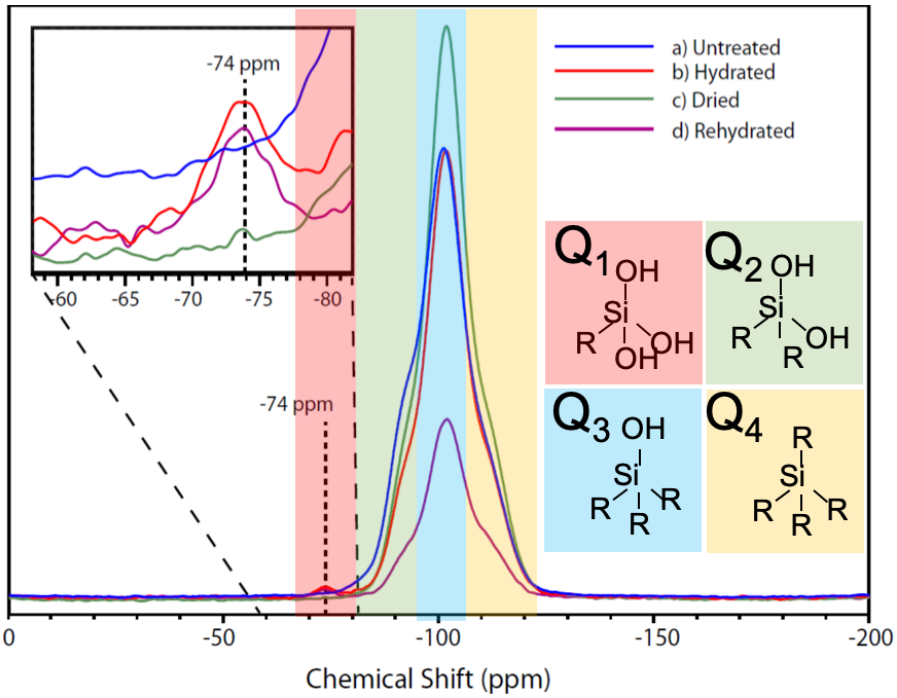

Figure 8.2: NMR ^{29}Si DNP-enhanced CP-MAS NMR spectra of the hydrophilic (αOH = 4.5 nm^{-2}) silica nanoparticles. The spectra were recorded at 95 K in a solvent prepared by mixing d_6-DMSO, D_2O, and H_2O in weight percentages of 78, 14, and 8, respectively. The blue line corresponds to the silica ~10 mins after immersion in the aqueous NMR solution. The red curve corresponds to the silica after 16 hours in 1× PBS, the green curve after drying for 18 hours, and the magenta curve after 16 hours of rehydration in 1× PBS. The inset shows the peak (or lack thereof) at -74 ppm, which corresponds to the Q1 signal. The Q1 signal comprises 1.4 % of the total integration of the red curve, and 2.7 % of the magenta curve.

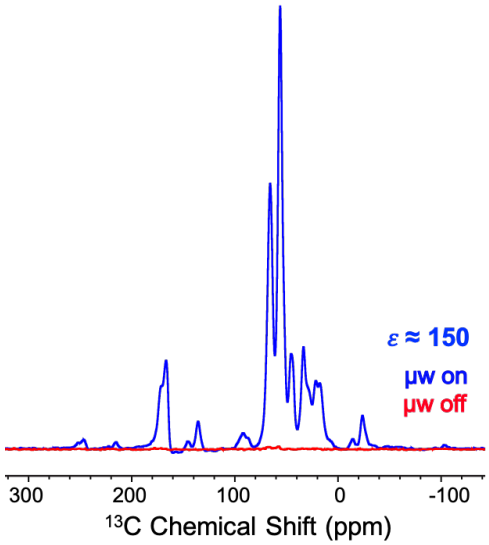

Figure 8.3: Tau peptide fragment used here was ^{273}GKVQIINKKLDL^{284} with the ^{274}K and ^{283}D residues uniformly labeled with ^{13}C and ^{15}N. 1 mg tau fragment was aggregated using heparin (15 kDa) with the concentration of peptide:heparin = 4:1. The fibril was then lyophilized and resuspended in 30 μL DNP Juice with 10 mM AMUPol radical dissolved. Sample was packed in a 3.2 mm Bruker sapphire DNP rotor. The spectra were acquired suing ^{13}C CP-MAS using a 400 MHz Bruker DNP system operating at 95 K. The buildup time used in the set of experiments was D1 = 10 s and the number of scans is 4. Blue spectra was acquired with μw irradiation. Red spectra was acquired without μw irradiation as a comparison. DNP enhancement was calculated to be $\sim$ 150.

dition. Using the Bruker 400 MHz DNP system operating at 95 K, we have reported large DNP enhancement of 150 for an aggregated Tau fragment (figure 8.3). Once homogeneous fibrils are produced, we would be able to utilize the large enhancement and reveal the intermediate stage.

8.3 Denoise the PR Transmembrane Protein DNP Spectra

Proteorhodopsin (PR) is a light-driven proton transport pump which belongs to the family of eubacterial retinal proteins. PR contains a highly conserved histidine site, His75, that directly interacts with PR's primary proton acceptor, Asp97, and is considered a "switch" in the proton transport. The hydrogen bond interaction between His75 and Asp97 has been suggested to stabilize the protonated form of Asp97, and hence increase the pKA of Asp97 (pKAD97). Previously our group has found that the electrostatic environment of PR embedded in liposomes, modulated by the ion concentration and type in the buffer and/or the net charge of liposomes, can directly toggle this apparent pKAD97 value significantly.[186] However, the reason why the intrinsic pKAD97 is altered by the electrostatic environment is not understood. DNP enhanced NMR has been applied to reveal the atomic-level structural rearrangements of PR upon changing electrostatic environment. DNP has provided an enhancement of 11, which requires further optimization of the sample preparation method. In addition, the signal sensitivity is also intrinsically limited by the protein sample loading amount and the amount of His sites in the PR protein.

In addition to the efforts in DNP radical optimization, wavelet denoising methods were applied to further overcome the low sensitivity issue. Figure 8.5A shows the ^{13}C CP-MAS spectrum upon applying wavelet denoising (green line). The DNP spectrum with 100 Hz exponential decay line-broadening window function (maroon line) and spectrum without line-broadening (grey line) were overlaid for comparison. With the wavelet denoising methods applied, the noise level of the DNP spectrum is significantly reduced. Moreover, using wavelet denoising instead of line-broadening function, the spectral linewidth is not

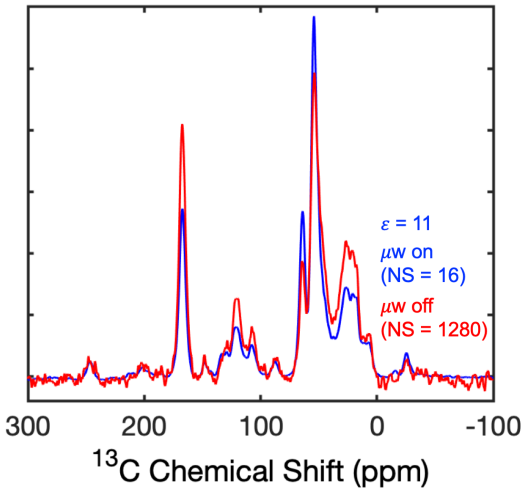

Figure 8.4: 3.5 mg [U-^{13}C]PR was prepared with POPC/POPG (80/20, mol/mol) membrane in a solvent with D_2O:H_2O = 3:1. The ratio of PR protein to lipid is 1:50. D_8glycerol was added to the solution and result in a solvent mixture with the ratio $d_8$glycerol:D_2O:H_2O = 6:3:1. 10 mM AMUPol was dissolved for DNP experiments. Sample was packed in a 3.2 mm Bruker sapphire DNP rotor. The spectra were acquired suing ^{13}C CP-MAS using a 400 MHz Bruker DNP system operating at 95 K. The buildup time used here was D1 = 2 s. Blue spectra was acquired with μw irradiation with 16 scans. Red spectra was acquired without μw irradiation with 1280 scans as a comparison. DNP enhancement was calculated to be $\sim$ 11.

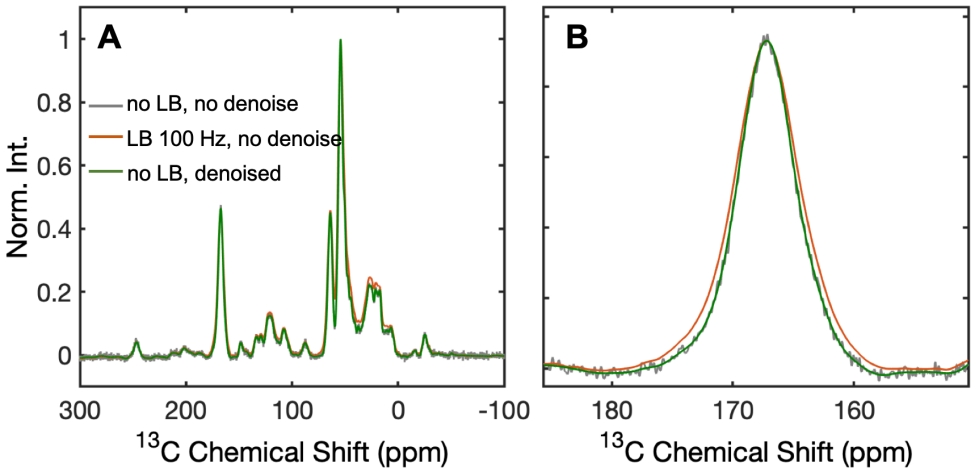

Figure 8.5: Acquired PR DNP spectra figure 8.4 was compared using different processing methods. Grey line shows the spectrum without applying line-broadening window functions or denoising methods. Maroon line displays the result with 100 Hz exponential decay line-broadening function applied. Green line is after applying wavelet denoising without line-broadening functions. A shows the PR DNP spectra. B displays the spectra zoomed in to the region corresponding to CO chemical shift.

impaired as shown in figure 8.5B, which is another great advantage of applying denoising in DNP signal processing. Further more, methods to denoise multi-dimensional DNP spectra are under development.

Chapter 9

Conclusion and Outlook

In conclusion, understanding DNP mechanism is essential in the field of DNP methods development to push the DNP enhancement close to the theoretical limit in the experimentally crucial high B_0 and fast magic angle spinning regimes under a large range of temperatures. I have shown that it is incomplete and sometimes misleading to diagnose DNP mechanisms using only NMR signal enhancements as a function of μw irradiation parameters such as resonance frequency, power, and irradiation time. As the efficiency and viability of DNP mechanisms rely heavily on the electron spin properties of the polarizing agent (PA), characterization of electron spin parameters is critical to understand and improve DNP mechanisms. Herein, a technical workflow of diagnosing DNP mechanisms and improving their efficiencies was developed and standardized, where DNP experiments, electron paramagnetic resonance (EPR) measurements and quantum mechanical simulations are all involved.

In this workflow, continuous wave and pulsed electron paramagnetic resonance (EPR) spectrometers at various fields (from 0.35 to 7 Tesla) were used to measure the EPR lineshapes, electron spin relaxation rates, and the electron spin polarization profiles under

μw irradiation obtained by pump-probe experiments. These experiments are vital to gain insight into the electron spin dynamics as well as the electron-electron coupling network and its effect on DNP mechanism efficiencies. For example, Cross Effect (CE) and Thermal Mixing (TM) DNP mechanisms can be diagnosed and optimized with the help of EPR spectroscopy to reveal the dynamics of the coupled electron spin system under operational DNP conditions. Pump-probe electron-electron double resonance (ELDOR) experiments can directly diagnose the polarization gradient generated by (shaped) μw irradiation; predict the efficiency of triple (e-e-n) flip processes; determine the extent of the e-e coupling network; and identify characteristic signatures of the underlying DNP mechanisms. Such diagnostic capabilities will be key to rational development of effective high field DNP methods. Such capabilities to diagnose the properties of the coupled electron and nuclear spin network are critical to utilize and apply TM using strongly coupled narrow line radicals that we believe is one of the most promising approaches for DNP.[54, 65]

Quantum mechanical simulation is another important part in this workflow as it offers a unique handle to selectively monitor the effect of different spin dynamics parameters and to dissect and understand DNP at a microscopic level. DNP is a complex process involving a multitude of interconnected parameters and events that occur on nanosecond timescales. As such, it is impossible to individually tune the effect of a single parameter experimentally, e.g., the coupling strength or type (dipolar or J coupling) or the microscopic, time dependent processes that lead to the build-up of bulk DNP enhancements. However, insight into these factors can be gained from fully quantum mechanical analysis of spin dynamics underlying DNP, which can in turn assist in the design of efficient PAs or new μw pulse schemes to maximize DNP under desirable experimental conditions.

Using this workflow, I have further optimized CE DNP efficiency through tuning the

e spin density by altering the ratio of mixed TEMPO and Trityl line radical.[27] By increasing the TEMPO:Trityl radical ratio from 1:1 to 2:1, I observed a DNP enhancement rise of 94% and 30% at static and spinning condition, respectively, in addition to much faster polarization buildup rate. With the help of quantum mechanical simulation, I have proposed a new CE radical design principle,*electron spin density matching*, which is tuning the composition of a mixed broad and narrow-line radical to boost the DNP efficiency. This workflow is also used to discover new DNP mechanisms. The discovery of a truncated CE DNP NMR that has the features of an Overhauser Effect (OE) DNP is a good example.[152] The apparent OE DNP, where minimal μw power achieved optimum enhancement, was observed when doping Trityl with a pyrroline nitroxide radical that possesses electron withdrawing, tetracarboxylate substitutes (tetracarboxylate-ester-pyrroline or TCP) in vitrified water/glycerol at 6.9 T and at 3.3 to 85 K, in apparent contradiction to expectations. While the observations are fully consistent with OE, we discovered that a truncated CE is the underlying mechanism, owing to TCP′s shortened T_{1e}. Quantum mechanical simulation is used to demonstrate that a crossover from CE to truncated CE can be replicated by simulating CE of a narrow-line (Trityl-OX063) and a broad-line (TCP) radical pair, with a significantly shortened T_{1e} of the broad-line radical. In addition to this study, we used this workflow and observed a surprising ^{1}H TM DNP with high concentration narrow-line radicals Trityl and BDPA.[54, 65] TM DNP diagnostic signatures have been experimentally ascertained by us that have only been theoretically predicted previously. The TM DNP signatures are: i) an EPR spectrum that maintains an asymmetrically broadened EPR-line from strong e-e couplings, and ii) hyperpolarization, i.e. cooling, of select electron-spin populations manifested in a characteristic pump-probe ELDOR spectrum under DNP conditions. In this TM DNP study, quantum mechanical simulations using a spatially asymmetrically coupled three electron spins and a nuclear spin demonstrated that triple-flip DNP, with hyperfine fluctuations

turned off, can yield the ^{1}H DNP profile as observed with Trityl or BDPA depending on the *e*-*e* coupling network. Low microwave power requirements, high polarization transfer rates and efficient DNP at high magnetic field B_0 are key benefits of TM DNP.

Instrumentation development is also critical for DNP methods development. Achieving MAS DNP/NMR experiments at ultra low temperature (ULT) ($\ll$ 100 K) have demonstrated clear benefits for obtaining large signal sensitivity gain and probing spin dynamics phenomena at ULT. However, ULT DNP/NMR is not widely used, given limited availability of such instrumentation from commercial sources. In this work, I present a comprehensive study of hydrated [U-^{13}C]alanine, a standard biosolid sample, from the first commercial 14.1 Tesla NMR spectrometer equipped with a closed-cycle helium ULT-MAS system. The closed-cycle helium MAS system provides precise temperature control from 25 K to 100 K and stable MAS from 1.5 kHz to 12 kHz with little Helium gas consumption. The ^{13}C CP-MAS NMR of [U-^{13}C]alanine showed 400% signal gain at 28 K compared with 100 K. The ULT NMR sensitivity enhancement results from the Boltzmann distribution favored at low temperature, radio frequency circuitry quality factor improvement and the suppression of Alanine's methyl group rotation. ^{1}H T_1 of H_2O in a d_8-glycerol/ D_2O/ H_2O mixture is dramatically shortened from minutes to a few seconds with the addition of 10 mM biradicals (AMUPol or TEMTriPol-1) due to allowed *e*-*e*-*n* triple flip transitions that also give rise to CE DNP. It is worth nothing that the ^{13}C spectral linewidth is not furthered broadened at ULT upon adding CE biradicals compared with no radical addition.

With the current DNP mechanism improvement and instrumentation development, the next step is to apply DNP in the characterization of biological and inorganic materials. With the enhancement of DNP, I showed that Q1 species (–$Si(OH)_3$) with the

amount of ~ 1 % of the total surface sites was formed upon hydration. This was observed using a natural abundance silica nano-particle sample, where the ^{29}Si natural abundance is only 4.67 %. DNP has also provided a large enhancement of 150 with the isotope labeled Tau amyloid fibril fragment impregnated with water/glycerol solution with 10 mM AMUPol dissolved in. However, better NMR spectral resolution is still needed for the bio-solid NMR applications. In this regard, significant efforts have been devoted to obtain high quality Tau amyloid fibrils that packed more homogeneously. Transmission electron microscopy (TEM) and double electron-electron resonance (DEER) spectroscopy have been used rigorously to reveal the fibril packing quality. In addition, wavelet denoising is another on going project to further improve the NMR signal sensitivity and resolution during the signal processing stage.

Appendix A

Appendix: Instrumentation

A.1 DNP

A.1.1 Bruker 400 DNP-NMR

Bruker 400 MHz (9.4T) Dynamic Nuclear Polarization (DNP) NMR spectrometer with a 25 W gyrotron microwave source (G-factor range from 2.0163777 to 1.9844550) was used for DNP applications. The sample was cooled down to ∼95 K using cold nitrogen gas. The sample can be spun up to 12.5 kHz. 3.2mm MAS DNP-NMR triple resonance broadband X/Y/H probe was used for experiments.

A.1.2 Static 6.9 T Dual Pulsed DNP/EPR System

The cylindrical Teflon sample holder has the following dimensions: 7 mm o.d. and outer height, with 0.5 mm thick walls. The sample holder was inserted into a 294 MHz home-built inductively coupled Alderman-Grant ^{1}H NMR coil,[77] with a silver-plated mirror below the sample to increase the microwave B_1 field. The NMR probe insert

consisting of a NMR coil and associated circuitry and a corrugated waveguide (Thomas Keating Ltd) to transmit microwaves to the sample for DNP and EPR was top-loaded into a custom-designed Janis STVP-NMR wide-bore cryostat. Continuous flow of liquid helium was used to cool the cryostat and NMR probe insert to 3.3 K-200 K. All DNP experiments were performed using a Bruker 300 Avance solid-state NMR spectrometer at a field strength of 6.9 Tesla (T). Microwaves for DNP and EPR experiments were produced from ss-microwave YIG sources (Microlambda and Virginia Diodes Inc), where 12 GHz irradiation passed through 16x amplification and multiplication chains (AMCs) to reach ≈194 GHz. A home-built pulse forming network with arbitrary waveform generators (AWGs) at 12 GHz allowed for precise frequency and phase manipulation of continuous wave (CW) and pulsed microwave irradiation.[77, 78] After amplification and multiplication of the microwaves, quasi optics (Thomas Keating Ltd) were used to couple the microwaves in free space to the waveguide in the NMR probe insert, which were then directed to the sample. For heterodyne EPR operation, a wiregrid polarizer in the quasi optics was used to separate the elliptical reflected microwaves into induction and reflection mode EPR signal. The two sources used for pump-probe type experiments have orthogonal polarizations, thus one source would result in induction mode EPR signal at the heterodyne detector, while the second source would result in reflection mode EPR signal at the detector. A receiver system (Virginia Diodes Inc) was used to collect the 194 GHz EPR signal and down convert the EPR signal to a 3 GHz intermediate frequency. This 3 GHz EPR signal was then mixed with a 3 GHz reference in an IQ mixer to achieve phase sensitive heterodyne detection that is directly digitized. The microwave manipulation and synchronization with NMR detection schemes were controlled by Specman4EPR. Additional descriptions of the hardware setup can be found in previous publications by the Han group.[77, 78, 47, 187, 103]

A.1.3 MAS 6.9 T Pulsed DNP System

30 μL sample solution was blended with ~60 mg dry KBr for the purpose of temperature calibration inside a zirconia rotor obtained from Revolution NMR, which has the following dimension: 4 mm outer-diameter, 2.36 mm inner-diameter, and 46 mm axial-length. The sample position was fixed at the center of the rotor using Teflon-inserts placed at its both ends. The rotor was cooled down to 25 K with helium gas in the center, and was spun with room temperature nitrogen gas on the side. The sample temperature was calibrated by measuring the spin-lattice relaxation time of ^{79}Br, as demonstrated by Thurber *et al.*.[188, 189] Continuous-wave μw was irradiated from tuneable Virginia Diode Inc. source, with a frequency range of 193-201 GHz and μw irradiation power up to 350 mW, measured at right after AMC transmitter. The transmitted μw beam was guided through QO bridge, and finally reached to the corrugated wave-guide inside the 6.9 T wide bore magnet. The sample rotor (MAS-Stator) was located at the end of the wave-guide. The design of the probe was an adaptation from the design of Thurber *et al.*.[188, 189] More detailed description can be found in a recent publication from Han group.[45]

A.2 Low Field EPR

X-band CW: CW EPR experiments were operating at 0.35 T (10 GHz) (X-band frequency) using a commercial Bruker EMX CW EPR spectrometer. Samples were prepared in quartz capillaries (0.6 inner-diameter, 0.8 outer-diameter), and inserted into 3 mm EPR quartz tubes.

X-band ELEXYS: pulse EPR experiments at X-band (10 GHz) were conducted with an ELEXYS 580 Bruker spectrometer with a liquid helium cryostat from Oxford

Inc.. Samples were prepared in quartz capillaries (0.6 inner-diameter, 0.8 outer-diameter), and inserted into 3 mm EPR quartz tubes.

Q-band ELEXYS: pulse EPR experiments at Q-band (34 GHz) were also performed on an ELEXYS 580 Bruker spectrometer equipped with a liquid helium cryostat from Oxford Inc. Quartz capillaries (0.6 inner-diameter, 0.8 outer-diameter) were also used for sample preparation and were inserted into 3 mm EPR quartz tubes inside the resonator.

A.3 ULT MAS NMR with Helium Circulation

The JEOL ULT closed-cycle helium MAS system requires little helium gas for operation without losing helium during experiments. With the current probe design, the major source of helium gas consumption is the sample exchange. In this process, the probe was detached from the heat exchanger and was loaded with the sample rotor. Afterwards, the probe was connected back to the magnet and was flushed with helium gas before reattaching to the heat exchanger. In total, a 7-m^3 helium gas tank allows >15 times of sample exchange process.

There are major two steps to cool down the sample: heat exchanger cooling and probe cooling. During the first step, the heat exchanger was initially disconnected from the probe. Helium gas in the heat exchanger was cooled with compressors and the temperature was stabilized using internal heaters. It took ∼4 h to cool down the heat exchanger from room temperature to < 20 K. During the sample exchange process, the heat exchanger was disconnected from the probe and the temperature was maintained at the setting values. In the second step, the probe was connected back to the heat

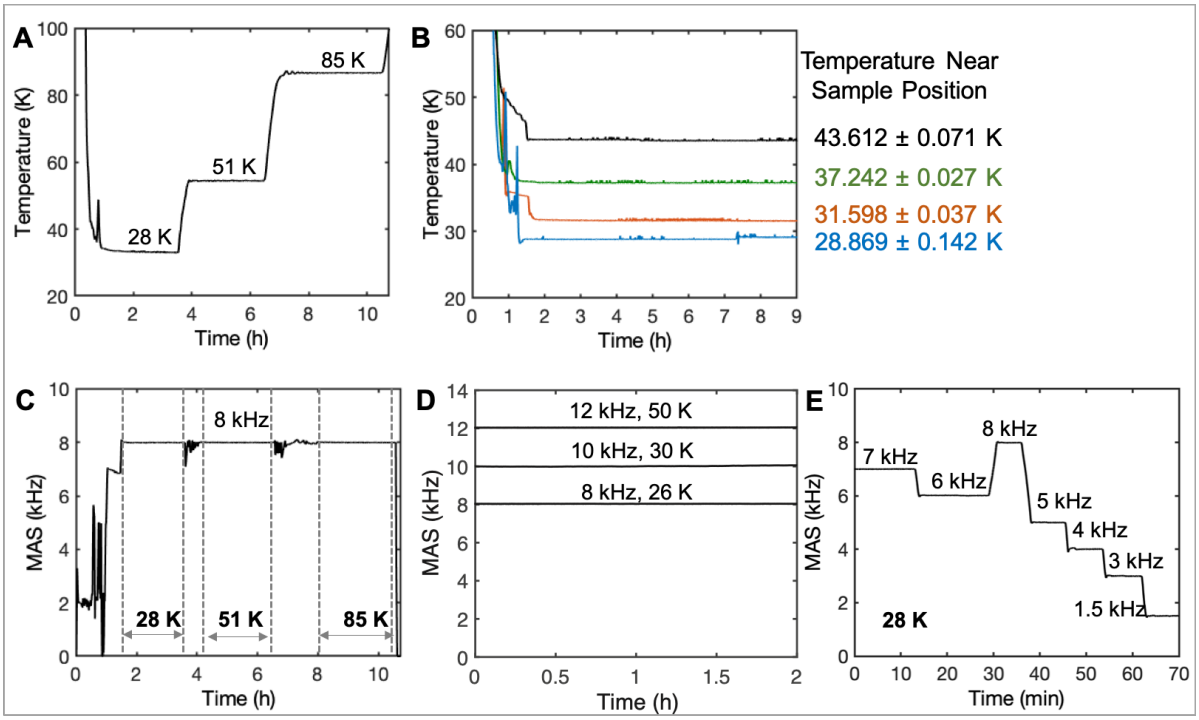

Figure A.1: A. Sample temperature (calibrated using KBr) as a function of time during cooling and warming up at setting temperatures. B. Temperature measured through the sensor near the sample position as a function of time during cooling and stabilization. C. MAS as a function of time at different setting temperatures. D. MAS as a function of time when temperature was stabilized at 26 K, 30 K and 50 K. Stable MAS of 8 kHz ±3 Hz at 26 K, 10 kHz ±3 Hz at 30 K and 12 kHz ±3 Hz at 50 K were reached. E. Changing MAS from 1.5 to 8 kHz with a step size of 1-1.5 kHz at 28 K.

exchanger. Both the sample and probe were cooled by the cold bearing and drive helium gas provided by the heat exchanger. Sample temperature was further regulated using the heaters in the probe for bearing and drive helium. It took ∼1 h for the sample temperature to be brought down to and stabilized at the target value.

We then tested the efficiency of the warmup process and sample temperature stability. Figure A.1A shows that the sample temperature is stabilized from 28 K to 51 K within 0.5 h and from 51 K to 85 K within 1 h. Figure A.1B displays temperature sensor readings at the sample position as a function of time. Upon stabilization, the sample temperature

sensor reading only displays a fluctuation of up to ± 0.142 K over a long duration (> 7 h).

Sample spinning using the helium circulation system was further evaluated. Figure A.1C shows that the sample achieved stable 8 kHz MAS while changing the temperature from 28 K to 51 K and 85 K. Further MAS stability tests were performed at different temperatures, where stable MAS of 8 kHz ± 3 Hz, 10 kHz ± 3 Hz and 12 kHz ± 3 Hz were achieved at 26 K, 30 K and 50 K, respectively (figure A.1D). The MAS variation was calculated using standard deviation for the 2-h duration. 8 kHz stable MAS at 26 K was attained for more than 10 h. The helium circulation system also allows convenient variable MAS speeds as shown in figure A.1E. Stable MAS was achieved from 1.5 to 8 kHz within ∼ 2 min of stabilizing time at each step. It is worth noting that the reported MAS (8 kHz at 26 K, 10 kHz at 30 K and 12 kHz at 50 K) are not the maximum MAS speeds the system can reach. With the current design, the maximum achievable MAS is mainly limited by the capacity of the bellows compressors, where the bearing line bellows compressor produces a maximum helium flow rate of 80 L/min and pressure of 270 kPa and drive line bellows compressor produce a maximum helium flow rate of ∼ 120 L/min and pressure of 270 kPa. All the helium gas flow rates measured by us are using the normal liter per minute (NLPM) standard. As a reference, using the Osaka system, Matsuki *et al*. has reported maximum MAS speeds of 12 kHz ± 5 Hz at 30 K and 14 kHz ± 5 Hz at 60 K, where the reported MAS speeds are stable for days. [161] With the Grenoble system, Lee *et al*. achieved a maximum MAS of 17.5 kHz at 50 K. [164] The maximum helium gas flow rates for the Grenoble system are: 250 L/min for bearing, 250 L/min for drive and 500 L/min for VT. The reported MAS stability for the Grenoble system at 50 K with 7 kHz MAS is ± 50 Hz.

The evaluation results suggest that the JEOL ULT helium circulation system provides

a stable MAS at variable temperatures. The cooling is efficient and requires low helium consumption. The sample spinning speed is not coupled to temperature and can be easily stabilized at different MAS rates. A future probe designed with sample exchange ability is under construction for even more efficient cooling and less helium consumption. We further explored the benefits of conducting MAS NMR experiments for hydrated bio-solid samples under ULT using this setup.

Appendix B

Appendix: Spin Labeling

B.1 Labeling Silica Nano-particle

1. Dehydroxylate silica nanoparticle (np-Si) under a certain temperature:

a. Weigh around 150 mg np-Si and use a tube furnace to perform dehydroxylation at a certain temperature.

b. Condition of tube furnace: Heat the sample up 10 C/min to the target temperature and then maintain the temperature for 6 h. Then, cool the sample down 10 C/min. N2 or Ar gas flow should be applied from the beginning to the end.

2. Functionalize silica:

a. Mix 20 mg np-Si with 2 mL PBS Buffer (pH = 7.4). Stir under room temperature for 16 h. The result concentration is 10mg silica/mL PBS.

b. Add 1.1 L APDMES into silica solution. Stir for another 16 h under room temperature. (Calculation is: add L= (3.12*10 $^{-4}$)*m silica*SSA*n_{NH2}/, where msilica is the mass of silica sample in mg, SSA is the specific surface area of our sample in m^2/g, n_{NH2} is the desired amount of NH_2 in numbers of NH_2/nm^2 , is the efficiency 0-1)

c. Separate the solution into two portions: one will be spin labeled, another one is the control group. Centrifuge each portion at 8000 rpm/rcf 23 C for 4 min.

3. Spin label:

a. Add $\geq$ 666 L 10 mM TEMPO solution (TEMPO dissolved in MES buffer 0.1 M, pH = 4.5) into silica solution, which result in a concentration 20 times excess. For the reference sample, just add 666 L MES buffer. Vortex and sonicate the mixture until suspended.

b. Add catalyst $\geq$ 1.333 mL EDC+MES buffer ($\sim$ 50 mM, 8-10 mg/mL) solution to the mixture. Store it in fridge to react 20 min (rotate the solution at the same time). (EDC solution should only be made right before usage.)

c. Centrifuge the solution for 5 min at 8000 rpm/rcf 23 oC. Remove the solvent.

d. Wash the silica sample with 1 mL NaCl (15 mM) five times: 8000 rpm/rcf 23 C for 4 min each time.

e. Mix the final sample with 42 L NaCl (15 mM), Vortex and sonicate. Store the final solution in fridge until Overhauser DNP measurements.

B.2 Tau Fibrils for EPR Measurements

MTSL Labeling Peptides

a. Dissolve 1 mg peptide in 1 mL of 20 mM Ammonium Acetate (pH=7, fully deuterated) and MTSL at a concentration 5 times the concentration of cysteines. Incubate the solution at 4 C overnight or room temperature for 1 h.

b. Buffer exchange through a G-10 column twice into MTSL free buffer. Since G-10 elutes 1.2 mL but only takes 1 mL, the extra 200 uL for the second run can be considered as a lost. The instruction can be found from the instruction website using the gravity protocol.[190]

Aggregating Spin labeled Tau Fibril

a. Spin labeled peptides are mixed with Cys-less monomer tau peptides resulting a total concentration of 600 uM total peptide concentration and 6.6 % spin label concentration in 20 mM Ammonium Acetate buffer (pH = 7, D_2O). 150 μM heparin (15 kDa) was added to the 600 μM peptide resulting a 4:1 = peptide : heparin mixture. The whole sample was incubated under 37 C overnight.

b. 60 uL tau 16 heparin fibril solution was purified through dialysis bag (12 kDa cut off) at 4 C for 24 h. The solution outside the dialysis bag is also 20 mM Ammonium Acetate buffer (pH = 7, D_2O). Concentrate the sample solution by 30-50% through

purging N_2 gas.

Bibliography

[1] A. S. L. Thankamony, J. J. Wittmann, M. Kaushik, and B. Corzilius, *Dynamic nuclear polarization for sensitivity enhancement in modern solid-state nmr*, *Progress in Nuclear Magnetic Resonance Spectroscopy* **102-103** (2017), no. Supplement C 120 – 195.

[2] J. Jeon, K. R. Thurber, R. Ghirlando, W.-M. Yau, and R. Tycko, *Application of millisecond time-resolved solid state nmr to the kinetics and mechanism of melittin self-assembly*, *Proceedings of the National Academy of Sciences* **116** (2019), no. 34 16717–16722.

[3] A. Potapov, W.-M. Yau, R. Ghirlando, K. R. Thurber, and R. Tycko, *Successive stages of amyloid-β self-assembly characterized by solid-state nuclear magnetic resonance with dynamic nuclear polarization*, *J. Am. Chem. Soc.* **137** (2015), no. 25 8294–8307.

[4] B. J. Wylie, B. G. Dzikovski, S. Pawsey, M. Caporini, M. Rosay, J. H. Freed, and A. E. McDermott, *Dynamic nuclear polarization of membrane proteins: covalently bound spin-labels at protein–protein interfaces*, *Journal of Biomolecular NMR* **61** (Apr, 2015) 361–367.

[5] Y. Su, L. Andreas, and R. G. Griffin, *Magic angle spinning nmr of proteins: High-frequency dynamic nuclear polarization and 1h detection*, *Annual Review of Biochemistry* **84** (2015), no. 1 465–497, [https://doi.org/10.1146/annurev-biochem-060614-034206]. PMID: 25839340.

[6] A. N. Smith, M. A. Caporini, G. E. Fanucci, and J. R. Long, *A method for dynamic nuclear polarization enhancement of membrane proteins*, *Angewandte Chemie International Edition* **54** (2015), no. 5 1542–1546, [https://onlinelibrary.wiley.com/doi/pdf/10.1002/anie.201410249].

[7] F. A. Perras, T. Kobayashi, and M. Pruski, *Natural abundance 17o dnp two-dimensional and surface-enhanced nmr spectroscopy*, *J. Am. Chem. Soc.* **137** (2015), no. 26 8336–8339.

[8] W. R. Grüning, A. J. Rossini, A. Zagdoun, D. Gajan, A. Lesage, L. Emsley, and C. Copéret, *Molecular-level characterization of the structure and the surface*

chemistry of periodic mesoporous organosilicates using dnp-surface enhanced nmr spectroscopy, *Physical Chemistry Chemical Physics* **15** (2013), no. 32 13270–13274.

[9] O. Lafon, A. S. L. Thankamony, M. Rosay, F. Aussenac, X. Lu, J. Trébosc, V. Bout-Roumazeilles, H. Vezin, and J.-P. Amoureux, *Indirect and direct 29 si dynamic nuclear polarization of dispersed nanoparticles*, *Chemical Communications* **49** (2013), no. 28 2864–2866.

[10] T. Wolf, S. Kumar, H. Singh, T. Chakrabarty, F. Aussenac, A. I. Frenkel, D. T. Major, and M. Leskes, *Endogenous dynamic nuclear polarization for natural abundance 17o and lithium nmr in the bulk of inorganic solids*, *Journal of the American Chemical Society* **141** (2018), no. 1 451–462.

[11] O. Lafon, A. S. L. Thankamony, T. Kobayashi, D. Carnevale, V. Vitzthum, I. I. Slowing, K. Kandel, H. Vezin, J.-P. Amoureux, G. Bodenhausen, *et. al.*, *Mesoporous silica nanoparticles loaded with surfactant: low temperature magic angle spinning 13c and 29si nmr enhanced by dynamic nuclear polarization*, *J. Phys. Chem. C* **117** (2013), no. 3 1375–1382.

[12] P. Berruyer, L. Emsley, and A. Lesage, *Dnp in materials science: touching the surface*, *Emagres* (2007) 93–104.

[13] H. Nagashima, J. Trebosc, Y. Kon, K. Sato, O. Lafon, and J.-P. Amoureux, *Observation of low-γ quadrupolar nuclei by surface-enhanced nmr spectroscopy*, *Journal of the American Chemical Society* (2020).

[14] A. Lesage, M. Lelli, D. Gajan, M. A. Caporini, V. Vitzthum, P. Miéville, J. Alauzun, A. Roussey, C. Thieuleux, A. Mehdi, *et. al.*, *Surface enhanced nmr spectroscopy by dynamic nuclear polarization*, *Journal of the American Chemical Society* **132** (2010), no. 44 15459–15461.

[15] M. Lelli, D. Gajan, A. Lesage, M. A. Caporini, V. Vitzthum, P. Miéville, F. Héroguel, F. Rascón, A. Roussey, C. Thieuleux, *et. al.*, *Fast characterization of functionalized silica materials by silicon-29 surface-enhanced nmr spectroscopy using dynamic nuclear polarization*, *Journal of the American Chemical Society* **133** (2011), no. 7 2104–2107.

[16] V. Vitzthum, P. Miéville, D. Carnevale, M. A. Caporini, D. Gajan, C. Copéret, M. Lelli, A. Zagdoun, A. J. Rossini, A. Lesage, *et. al.*, *Dynamic nuclear polarization of quadrupolar nuclei using cross polarization from protons: surface-enhanced aluminium-27 nmr*, *Chemical Communications* **48** (2012), no. 14 1988–1990.

[17] V. Aladin, M. Vogel, R. Binder, I. Burghardt, B. Suess, and B. Corzilius, *Complex formation of the tetracycline-binding aptamer investigated by specific*

cross-relaxation under dnp, *Angewandte Chemie International Edition* **58** (2019), no. 15 4863–4868,
[https://onlinelibrary.wiley.com/doi/pdf/10.1002/anie.201811941].

[18] R. Rogawski, I. V. Sergeyev, Y. Li, M. F. Ottaviani, V. Cornish, and A. E. McDermott, *Dynamic nuclear polarization signal enhancement with high-affinity biradical tags*, *The Journal of Physical Chemistry B* **121** (2017), no. 6 1169–1175, [https://doi.org/10.1021/acs.jpcb.6b09021]. PMID: 28099013.

[19] T. R. Carver and C. P. Slichter, *Polarization of nuclear spins in metals*, *Phys. Rev.* **92** (Oct, 1953) 212–213.

[20] Y. Hovav, A. Feintuch, and S. Vega, *Theoretical aspects of dynamic nuclear polarization in the solid state–the solid effect*, *Journal of Magnetic Resonance* **207** (2010), no. 2 176–189.

[21] Y. Hovav, A. Feintuch, and S. Vega, *Theoretical aspects of dynamic nuclear polarization in the solid state–the cross effect*, *Journal of Magnetic Resonance* **214** (2012) 29–41.

[22] W. T. Wenckebach, *Dynamic nuclear polarization via the cross effect and thermal mixing: A. the role of triple spin flips*, *Journal of Magnetic Resonance* **299** (2019) 124–134.

[23] F. Jähnig, A. Himmler, G. Kwiatkowski, A. Däpp, A. Hunkeler, S. Kozerke, and M. Ernst, *A spin-thermodynamic approach to characterize spin dynamics in tempo-based samples for dissolution dnp at 7 t field*, *Journal of Magnetic Resonance* **303** (2019) 91–104.

[24] A. Zagdoun, G. Casano, O. Ouari, M. Schwarzwälder, A. J. Rossini, F. Aussenac, M. Yulikov, G. Jeschke, C. Coperet, A. Lesage, *et. al.*, *Large molecular weight nitroxide biradicals providing efficient dynamic nuclear polarization at temperatures up to 200 k*, *Journal of the American Chemical Society* **135** (2013), no. 34 12790–12797.

[25] G. Mathies, M. A. Caporini, V. K. Michaelis, Y. Liu, K.-N. Hu, D. Mance, J. L. Zweier, M. Rosay, M. Baldus, and R. G. Griffin, *Efficient dynamic nuclear polarization at 800 mhz/527 ghz with trityl-nitroxide biradicals*, *Angewandte Chemie International Edition* **54** (2015), no. 40 11770–11774.

[26] D. Wisser, G. Karthikeyan, A. Lund, G. Casano, H. Karoui, M. Yulikov, G. Menzildjian, A. C. Pinon, A. Purea, F. Engelke, *et. al.*, *Bdpa-nitroxide biradicals tailored for efficient dynamic nuclear polarization enhanced solid-state nmr at magnetic fields up to 21.1 t*, *Journal of the American Chemical Society* **140** (2018), no. 41 13340–13349.

[27] Y. Li, A. Equbal, K. Tagami, and S. Han, *Electron spin density matching for cross-effect dynamic nuclear polarization*, *Chemical Communications* **55** (2019), no. 53 7591–7594.

[28] F. Mentink-Vigier, I. Marin-Montesinos, A. P. Jagtap, T. Halbritter, J. Van Tol, S. Hediger, D. Lee, S. T. Sigurdsson, and G. De Paëpe, *Computationally assisted design of polarizing agents for dynamic nuclear polarization enhanced nmr: the asympol family*, *Journal of the American Chemical Society* **140** (2018), no. 35 11013–11019.

[29] A. Leavesley, S. Jain, I. Kamniker, H. Zhang, S. Rajca, A. Rajca, and S. Han, *Maximizing nmr signal per unit time by facilitating the e–e–n cross effect dnp rate*, *Physical Chemistry Chemical Physics* **20** (2018), no. 43 27646–27657.

[30] M. Lelli, S. R. Chaudhari, D. Gajan, G. Casano, A. J. Rossini, O. Ouari, P. Tordo, A. Lesage, and L. Emsley, *Solid-state dynamic nuclear polarization at 9.4 and 18.8 t from 100 k to room temperature*, *Journal of the American Chemical Society* **137** (2015), no. 46 14558–14561.

[31] A. Lund, G. Casano, G. Menzildjian, M. Kaushik, G. Stevanato, M. Yulikov, R. Jabbour, D. Wisser, M. Renom-Carrasco, C. Thieuleux, *et. al.*, *Tinypols: a family of water-soluble binitroxides tailored for dynamic nuclear polarization enhanced nmr spectroscopy at 18.8 and 21.1 t*, *Chemical Science* **11** (2020), no. 10 2810–2818.

[32] P. Berruyer, S. Björgvinsdottir, A. Bertarello, G. Stevanato, Y. Rao, G. Karthikeyan, G. Casano, O. Ouari, M. Lelli, C. Reiter, *et. al.*, *Dynamic nuclear polarization enhancement of 200 at 21.15 t enabled by 65 khz magic angle spinning*, *The Journal of Physical Chemistry Letters* **11** (2020), no. 19 8386–8391.

[33] A. Equbal, K. Tagami, and S. Han, *Balancing dipolar and exchange coupling in biradicals to maximize cross effect dynamic nuclear polarization*, *Physical Chemistry Chemical Physics* **22** (2020), no. 24 13569–13579.

[34] A. Equbal, Y. Li, T. Tabassum, and S. Han, *Crossover from solid effect to thermal mixing 1h dynamic nuclear polarization in trityl-ox063*, *The Journal of Physical Chemistry Letters* (2020).

[35] A. Bornet, A. Pinon, A. Jhajharia, M. Baudin, X. Ji, L. Emsley, G. Bodenhausen, J. H. Ardenkjaer-Larsen, and S. Jannin, *Microwave-gated dynamic nuclear polarization*, *Physical Chemistry Chemical Physics* **18** (2016), no. 44 30530–30535.

[36] S. K. Jain, T. A. Siaw, A. Equbal, C. B. Wilson, I. Kaminker, and S. Han, *Reversal of paramagnetic effects by electron spin saturation*, *The Journal of Physical Chemistry C* **122** (2018), no. 10 5578–5589.

[37] A. Leavesley, C. B. Wilson, M. Sherwin, and S. Han, *Effect of water/glycerol polyhysrevlett.18.110morphism on dynamic nuclear polarization*, *Physical Chemistry Chemical Physics* **20** (2018), no. 15 9897–9903.

[38] A. Equbal, Y. Li, A. Leavesley, S. Huang, S. Rajca, A. Rajca, and S. Han, *Truncated cross effect dynamic nuclear polarization: An overhauser effect doppelgänger*, *The journal of physical chemistry letters* **9** (2018), no. 9 2175–2180.

[39] P. Gast, D. Mance, E. Zurlo, K. L. Ivanov, M. Baldus, and M. Huber, *A tailored multi-frequency epr approach to accurately determine the magnetic resonance parameters of dynamic nuclear polarization agents: application to amupol*, *Physical Chemistry Chemical Physics* **19** (2017), no. 5 3777–3781.

[40] J. Soetbeer, P. Gast, J. J. Walish, Y. Zhao, C. George, C. Yang, T. M. Swager, R. G. Griffin, and G. Mathies, *Conformation of bis-nitroxide polarizing agents by multi-frequency epr spectroscopy*, *Physical Chemistry Chemical Physics* **20** (2018), no. 39 25506–25517.

[41] K. Tagami, A. Equbal, I. Kaminker, B. Kirtman, and S. Han, *Biradical rotamer states tune electron j coupling and mas dynamic nuclear polarization enhancement*, *Solid state nuclear magnetic resonance* **101** (2019) 12–20.

[42] W. Zhai, Y. Feng, H. Liu, A. Rockenbauer, D. Mance, S. Li, Y. Song, M. Baldus, and Y. Liu, *Diastereoisomers of l-proline-linked trityl-nitroxide biradicals: synthesis and effect of chiral configurations on exchange interactions*, *Chemical science* **9** (2018), no. 19 4381–4391.

[43] A. Karabanov, G. Kwiatkowski, C. U. Perotto, D. Wiśniewski, J. McMaster, I. Lesanovsky, and W. Köckenberger, *Dynamic nuclear polarisation by thermal mixing: quantum theory and macroscopic simulations*, *Physical Chemistry Chemical Physics* **18** (2016), no. 43 30093–30104.

[44] D. J. Kubicki, G. Casano, M. Schwarzwälder, S. Abel, C. Sauvée, K. Ganesan, M. Yulikov, A. J. Rossini, G. Jeschke, C. Copéret, *et. al.*, *Rational design of dinitroxide biradicals for efficient cross-effect dynamic nuclear polarization*, *Chemical Science* **7** (2016), no. 1 550–558.

[45] A. Lund, A. Equbal, and S. Han, *Tuning nuclear depolarization under mas by electron t 1e*, *Phys. Chem. Chem. Phys.* **20** (2018), no. 37 23976–23987.

[46] E. Weber, H. Vezin, J. Kempf, G. Bodenhausen, D. Abergél, and D. Kurzbach, *Anisotropic longitudinal electronic relaxation affects dnp at cryogenic temperatures*, *Physical Chemistry Chemical Physics* **19** (2017), no. 24 16087–16094.

[47] A. Leavesley, D. Shimon, T. A. Siaw, A. Feintuch, D. Goldfarb, S. Vega, I. Kaminker, and S. Han, *Effect of electron spectral diffusion on static dynamic nuclear polarization at 7 tesla*, *Physical Chemistry Chemical Physics* **19** (2017), no. 5 3596–3605.

[48] Y. Hovav, D. Shimon, I. Kaminker, A. Feintuch, D. Goldfarb, and S. Vega, *Effects of the electron polarization on dynamic nuclear polarization in solids*, *Physical Chemistry Chemical Physics* **17** (2015), no. 8 6053–6065.

[49] Y. Hovav, A. Feintuch, S. Vega, and D. Goldfarb, *Dynamic nuclear polarization using frequency modulation at 3.34 t*, *Journal of Magnetic Resonance* **238** (2014) 94–105.

[50] K. Kundu, A. Feintuch, and S. Vega, *Theoretical aspects of the cross effect enhancement of nuclear polarization under static dynamic nuclear polarization conditions*, *The journal of physical chemistry letters* **10** (2019), no. 8 1769–1778.

[51] F. Mentink-Vigier, S. Vega, and G. De Paëpe, *Fast and accurate mas–dnp simulations of large spin ensembles*, *Physical Chemistry Chemical Physics* **19** (2017), no. 5 3506–3522.

[52] F. Mentink-Vigier, A.-L. Barra, J. Van Tol, S. Hediger, D. Lee, and G. De Paëpe, *De novo prediction of cross-effect efficiency for magic angle spinning dynamic nuclear polarization*, *Physical Chemistry Chemical Physics* **21** (2019), no. 4 2166–2176.

[53] F. A. Perras, A. Sadow, and M. Pruski, *In silico design of dnp polarizing agents: can current dinitroxides be improved?*, *ChemPhysChem* **18** (2017), no. 16 2279–2287.

[54] A. Equbal, A. Leavesley, S. K. Jain, and S. Han, *Cross-effect dynamic nuclear polarization explained: polarization, depolarization, and oversaturation*, *The journal of physical chemistry letters* **10** (2019), no. 3 548–558.

[55] K. R. Thurber and R. Tycko, *Theory for cross effect dynamic nuclear polarization under magic-angle spinning in solid state nuclear magnetic resonance: The importance of level crossings*, *The Journal of chemical physics* **137** (2012), no. 8 084508.

[56] F. Mentink-Vigier, Ü. Akbey, H. Oschkinat, S. Vega, and A. Feintuch, *Theoretical aspects of magic angle spinning-dynamic nuclear polarization*, *Journal of Magnetic Resonance* **258** (2015) 102–120.

[57] B. A. Rodin and K. L. Ivanov, *Representation of population exchange at level anti-crossings*, *Magnetic Resonance Discussions* (2020) 1–26.

[58] K. R. Thurber and R. Tycko, *Perturbation of nuclear spin polarizations in solid state nmr of nitroxide-doped samples by magic-angle spinning without microwaves*, *The Journal of chemical physics* **140** (2014), no. 18 05B608_1.

[59] F. Mentink-Vigier, S. Paul, D. Lee, A. Feintuch, S. Hediger, S. Vega, and G. De Paëpe, *Nuclear depolarization and absolute sensitivity in magic-angle spinning cross effect dynamic nuclear polarization*, *Physical Chemistry Chemical Physics* **17** (2015), no. 34 21824–21836.

[60] A. Equbal, K. Tagami, and S. Han, *Pulse-Shaped Dynamic Nuclear Polarization under Magic-Angle Spinning*, *Journal of Physical Chemistry Letters* **10** (dec, 2019) 7781–7788.

[61] M. Veshtort and R. G. Griffin, *Spinevolution: a powerful tool for the simulation of solid and liquid state nmr experiments*, *Journal of Magnetic Resonance* **178** (2006), no. 2 248–282.

[62] H. Hogben, M. Krzystyniak, G. Charnock, P. Hore, and I. Kuprov, *Spinach–a software library for simulation of spin dynamics in large spin systems*, *Journal of Magnetic Resonance* **208** (2011), no. 2 179–194.

[63] A. Karabanov, A. van der Drift, L. J. Edwards, I. Kuprov, and W. Köckenberger, *Quantum mechanical simulation of solid effect dynamic nuclear polarisation using krylov–bogolyubov time averaging and a restricted state-space*, *Physical Chemistry Chemical Physics* **14** (2012), no. 8 2658–2668.

[64] A. Lund, A. Equbal, and S. Han, *Tuning nuclear depolarization under mas by electron t1e*, *Physical Chemistry Chemical Physics* **xx** (2018), no. xx xxx–xxx.

[65] Y. Li, A. Equbal, T. Tabassum, and S. Han, *1h thermal mixing dynamic nuclear polarization with bdpa as polarizing agents*, *The Journal of Physical Chemistry Letters* **11** (2020) 9195–9202.

[66] F. A. Perras, M. Raju, S. L. Carnahan, D. Akbarian, A. C. Van Duin, A. J. Rossini, and M. Pruski, *Full-scale ab initio simulation of magic-angle-spinning dynamic nuclear polarization*, *The Journal of Physical Chemistry Letters* **11** (2020), no. 14 5655–5660.

[67] C. F. Hwang and D. A. Hill, *New effect in dynamic polarization*, *Phys. Rev. Lett.* **18** (1967), no. 4 110.

[68] M. Rosay, L. Tometich, S. Pawsey, R. Bader, R. Schauwecker, M. Blank, P. M. Borchard, S. R. Cauffman, K. L. Felch, R. T. Weber, *et. al.*, *Solid-state dynamic nuclear polarization at 263 ghz: spectrometer design and experimental results*, *Phys. Chem. Chem. Phys.* **12** (2010), no. 22 5850–5860.

[69] K.-N. Hu, H.-h. Yu, T. M. Swager, and R. G. Griffin, *Dynamic nuclear polarization with biradicals*, *J. Am. Chem. Soc.* **126** (2004), no. 35 10844–10845.

[70] A. Zagdoun, G. Casano, O. Ouari, M. Schwarzwälder, A. J. Rossini, F. Aussenac, M. Yulikov, G. Jeschke, C. Coperet, A. Lesage, *et. al.*, *Large molecular weight nitroxide biradicals providing efficient dynamic nuclear polarization at temperatures up to 200 k*, *J. Am. Chem. Soc.* **135** (2013), no. 34 12790–12797.

[71] C. Song, K.-N. Hu, C.-G. Joo, T. M. Swager, and R. G. Griffin, *Totapol: a biradical polarizing agent for dynamic nuclear polarization experiments in aqueous media*, *J. Am. Chem. Soc.* **128** (2006), no. 35 11385–11390.

[72] C. Sauvée, M. Rosay, G. Casano, F. Aussenac, R. T. Weber, O. Ouari, and P. Tordo, *Highly efficient, water-soluble polarizing agents for dynamic nuclear polarization at high frequency*, *Angew. Chem.* **125** (2013), no. 41 11058–11061.

[73] K.-N. Hu, V. S. Bajaj, M. Rosay, and R. G. Griffin, *High-frequency dynamic nuclear polarization using mixtures of tempo and trityl radicals*, *J. Chem. Phys.* **126** (2007), no. 4 044512.

[74] Y. Liu, F. A. Villamena, A. Rockenbauer, Y. Song, and J. L. Zweier, *Structural factors controlling the spin–spin exchange coupling: Epr spectroscopic studies of highly asymmetric trityl–nitroxide biradicals*, *J. Am. Chem. Soc.* **135** (2013), no. 6 2350–2356.

[75] D. Wisser, G. Karthikeyan, A. Lund, G. Casano, H. Karoui, M. Yulikov, G. Menzildjian, A. C. Pinon, A. Purea, F. Engelke, *et. al.*, *Bdpa-nitroxide biradicals tailored for efficient dynamic nuclear polarization enhanced solid-state nmr at magnetic fields up to 21.1 t*, *J. Am. Chem. Soc.* **140** (2018), no. 41 13340–13349.

[76] G. Mathies, M. A. Caporini, V. K. Michaelis, Y. Liu, K.-N. Hu, D. Mance, J. L. Zweier, M. Rosay, M. Baldus, and R. G. Griffin, *Efficient dynamic nuclear polarization at 800 mhz/527 ghz with trityl-nitroxide biradicals*, *Angew. Chem., Int. Ed.* **54** (2015), no. 40 11770–11774.

[77] T. A. Siaw, A. Leavesley, A. Lund, I. Kaminker, and S. Han, *A versatile and modular quasi optics-based 200 ghz dual dynamic nuclear polarization and electron paramagnetic resonance instrument*, *Journal of Magnetic Resonance* **264** (2016) 131–153.

[78] I. Kaminker, R. Barnes, and S. Han, *Arbitrary waveform modulated pulse epr at 200 ghz*, *Journal of Magnetic Resonance* **279** (2017) 81–90.

[79] A. Leavesley, I. Kaminker, and S. Han, *Versatile dynamic nuclear polarization hardware with integrated electron paramagnetic resonance capabilities*, *eMagRes* (2018) 133–154.

[80] E. M. Weber, G. Sicoli, H. Vezin, G. Frébourg, D. Abergel, G. Bodenhausen, and D. Kurzbach, *Sample ripening through nanophase separation influences the performance of dynamic nuclear polarization*, *Angew. Chem., Int. Ed.* **57** (2018), no. 18 5171–5175.

[81] F. Mentink-Vigier, G. Mathies, Y. Liu, A.-L. Barra, M. A. Caporini, D. Lee, S. Hediger, R. G. Griffin, and G. De Paëpe, *Efficient cross-effect dynamic nuclear polarization without depolarization in high-resolution mas nmr*, *Chemical science* **8** (2017), no. 12 8150–8163.

[82] M. Veshtort and R. G. Griffin, *Spinevolution: A powerful tool for the simulation of solid and liquid state nmr experiments*, *J. Magn. Reson.* **178** (2, 2006) 248–282.

[83] I. V. Sergeyev, F. Aussenac, A. Purea, C. Reiter, E. Bryerton, S. Retzloff, J. Hesler, L. Tometich, and M. Rosay, *Efficient 263 ghz magic angle spinning dnp at 100 k using solid-state diode sources*, *Solid State Nuclear Magnetic Resonance* (2019).

[84] C. Song, K.-N. Hu, C.-G. Joo, T. M. Swager, and R. G. Griffin, *Totapol: a biradical polarizing agent for dynamic nuclear polarization experiments in aqueous media*, *Journal of the American Chemical Society* **128** (2006), no. 35 11385–11390.

[85] K.-N. Hu, V. S. Bajaj, M. Rosay, and R. G. Griffin, *High-frequency dynamic nuclear polarization using mixtures of tempo and trityl radicals*, *The Journal of chemical physics* **126** (2007), no. 4 044512.

[86] A. Zagdoun, G. Casano, O. Ouari, G. Lapadula, A. J. Rossini, M. Lelli, M. Baffert, D. Gajan, L. Veyre, W. E. Maas, *et. al.*, *A slowly relaxing rigid biradical for efficient dynamic nuclear polarization surface-enhanced nmr spectroscopy: expeditious characterization of functional group manipulation in hybrid materials*, *Journal of the American Chemical Society* **134** (2012), no. 4 2284–2291.

[87] C. Sauvée, M. Rosay, G. Casano, F. Aussenac, R. T. Weber, O. Ouari, and P. Tordo, *Highly efficient, water-soluble polarizing agents for dynamic nuclear polarization at high frequency*, *Angewandte Chemie* **125** (2013), no. 41 11058–11061.

[88] F. A. Perras, R. R. Reinig, I. I. Slowing, A. D. Sadow, and M. Pruski, *Effects of biradical deuteration on the performance of dnp: towards better performing polarizing agents*, *Physical Chemistry Chemical Physics* **18** (2016), no. 1 65–69.

[89] A. W. Overhauser, *Polarization of nuclei in metals*, *Physical Review* **92** (1953), no. 2 411.

[90] T. R. Carver and C. P. Slichter, *Polarization of nuclear spins in metals*, *Physical Review* **92** (1953), no. 1 212.

[91] T. V. Can, M. A. Caporini, F. Mentink-Vigier, B. Corzilius, J. J. Walish, M. Rosay, W. E. Maas, M. Baldus, S. Vega, T. M. Swager, and R. G. Griffin, *Overhauser effects in insulating solids*, *The Journal of Chemical Physics* **141** (2014), no. 6 064202, [https://doi.org/10.1063/1.4891866].

[92] C. F. Koelsch, *Syntheses with triarylvinylmagnesium bromides. $\hat{I}\pm,\hat{I}^3$-bisdiphenylene-$\hat{I}^z$-phenylallyl, a stable free radical*, *Journal of the American Chemical Society* **79** (1957), no. 16 4439–4441, [http://dx.doi.org/10.1021/ja01573a053].

[93] O. Haze, B. Corzilius, A. A. Smith, R. G. Griffin, and T. M. Swager, *Water-soluble narrow-line radicals for dynamic nuclear polarization*, *Journal of the American Chemical Society* **134** (2012), no. 35 14287–14290.

[94] X. Ji, T. Can, F. Mentink-Vigier, A. Bornet, J. Milani, B. Vuichoud, M. Caporini, R. Griffin, S. Jannin, M. Goldman, and G. Bodenhausen, *Overhauser effects in non-conducting solids at 1.2k*, *Journal of Magnetic Resonance* **286** (2018) 138 – 142.

[95] S. Pylaeva, K. L. Ivanov, M. Baldus, D. Sebastiani, and H. Elgabarty, *Molecular mechanism of overhauser dynamic nuclear polarization in insulating solids*, *The Journal of Physical Chemistry Letters* **8** (2017), no. 10 2137–2142, [https://doi.org/10.1021/acs.jpclett.7b00561]. PMID: 28445055.

[96] S. R. Chaudhari, D. Wisser, A. C. Pinon, P. Berruyer, D. Gajan, P. Tordo, O. Ouari, C. Reiter, F. Engelke, C. Copéret, *et. al.*, *Dynamic nuclear polarization efficiency increased by very fast magic angle spinning*, *Journal of the American Chemical Society* **139** (2017), no. 31 10609–10612.

[97] S. Huang, J. T. Paletta, H. Elajaili, K. Huber, M. Pink, S. Rajca, G. R. Eaton, S. S. Eaton, and A. Rajca, *Synthesis and electron spin relaxation of tetracarboxylate pyrroline nitroxides*, *The Journal of organic chemistry* **82** (2017), no. 3 1538–1544.

[98] S. Huang, H. Zhang, J. T. Paletta, S. Rajca, and A. Rajca, *Reduction kinetics and electrochemistry of tetracarboxylate nitroxides*, *Free radical research* **52** (2018), no. 3 327–334.

[99] S. Stoll and A. Schweiger, *Easyspin, a comprehensive software package for spectral simulation and analysis in epr*, *Journal of magnetic resonance* **178** (2006), no. 1 42–55.

[100] C. F. Hwang and D. A. Hill, *Phenomenological model for the new effect in dynamic polarization*, *Physical Review Letters* **19** (1967), no. 18 1011.

[101] D. Banerjee, D. Shimon, A. Feintuch, S. Vega, and D. Goldfarb, *The interplay between the solid effect and the cross effect mechanisms in solid state 13c dnp at 95 ghz using trityl radicals*, *Journal of Magnetic Resonance* **230** (2013) 212–219.

[102] E. Ravera, D. Shimon, A. Feintuch, D. Goldfarb, S. Vega, A. Flori, C. Luchinat, L. Menichetti, and G. Parigi, *The effect of gd on trityl-based dynamic nuclear polarisation in solids*, *Physical Chemistry Chemical Physics* **17** (2015), no. 40 26969–26978.

[103] T. A. Siaw, M. Fehr, A. Lund, A. Latimer, S. A. Walker, D. T. Edwards, and S.-I. Han, *Effect of electron spin dynamics on solid-state dynamic nuclear polarization performance*, *Physical Chemistry Chemical Physics* **16** (2014), no. 35 18694–18706.

[104] A. Olankitwanit, V. Kathirvelu, S. Rajca, G. R. Eaton, S. S. Eaton, and A. Rajca, *Calix [4] arene nitroxide tetraradical and octaradical*, *Chemical Communications* **47** (2011), no. 22 6443–6445.

[105] H. Sato, V. Kathirvelu, G. Spagnol, S. Rajca, A. Rajca, S. S. Eaton, and G. R. Eaton, *Impact of electron- electron spin interaction on electron spin relaxation of nitroxide diradicals and tetraradical in glassy solvents between 10 and 300 k*, *The Journal of Physical Chemistry B* **112** (2008), no. 10 2818–2828.

[106] Y. Hovav, I. Kaminker, D. Shimon, A. Feintuch, D. Goldfarb, and S. Vega, *The electron depolarization during dynamic nuclear polarization: measurements and simulations*, *Physical Chemistry Chemical Physics* **17** (2015), no. 1 226–244.

[107] W. T. Wenckebach, *Essentials of dynamic nuclear polarization*. Spindrift Publications, 2016.

[108] A. Abragam and M. Goldman, *Nuclear magnetism: order and disorder*, .

[109] V. Atsarkin and A. Kessenikh, *Dynamic nuclear polarization in solids: the birth and development of the many-particle concept*, *Applied Magnetic Resonance* **43** (2012), no. 1-2 7–19.

[110] W. T. Wenckebach, *Spectral diffusion and dynamic nuclear polarization: Beyond the high temperature approximation*, *Journal of Magnetic Resonance* **284** (2017) 104–114.

[111] B. Provotorov, *Magnetic resonance saturation in crystals*, *Sov. Phys. JETP* **14** (1962), no. 5 1126–1131.

[112] M. Borghini, *Spin-temperature model of nuclear dynamic polarization using free radicals*, *Physical Review Letters* **20** (1968), no. 9 419.

[113] V. A. Atsarkin and M. Rodak, *Temperature of spin-spin interactions in electron spin resonance*, *Soviet Physics Uspekhi* **15** (1972), no. 3 251.

[114] W. de Boer, *Dynamic orientation of nuclei at low temperatures*, *Journal of Low Temperature Physics* **22** (1976), no. 1-2 185–212.

[115] W. T. Wenckebach, *Dynamic nuclear polarization via thermal mixing: Beyond the high temperature approximation*, *Journal of Magnetic Resonance* **277** (2017) 68–78.

[116] S. Cox, V. Bouffard, and M. Goldman, *The coupling of two nuclear zeeman reservoirs by the electronic spin-spin reservoir*, *Journal of Physics C: Solid State Physics* **6** (1973), no. 5 L100.

[117] D. Guarin, S. Marhabaie, A. Rosso, D. Abergel, G. Bodenhausen, K. L. Ivanov, and D. Kurzbach, *Characterizing thermal mixing dynamic nuclear polarization via cross-talk between spin reservoirs*, *The journal of physical chemistry letters* **8** (2017), no. 22 5531–5536.

[118] I. Marin-Montesinos, J. C. Paniagua, M. Vilaseca, A. Urtizberea, F. Luis, M. Feliz, F. Lin, S. Van Doorslaer, and M. Pons, *Self-assembled trityl radical capsules–implications for dynamic nuclear polarization*, *Physical Chemistry Chemical Physics* **17** (2015), no. 8 5785–5794.

[119] I. Marin-Montesinos, J. C. Paniagua, A. Peman, M. Vilaseca, F. Luis, S. Van Doorslaer, and M. Pons, *Paramagnetic spherical nanoparticles by the self-assembly of persistent trityl radicals*, *Physical Chemistry Chemical Physics* **18** (2016), no. 4 3151–3158.

[120] T. A. Siaw, A. Leavesley, A. Lund, I. Kaminker, and S. Han, *A versatile and modular quasi optics-based 200ghz dual dynamic nuclear polarization and electron paramagnetic resonance instrument*, *Journal of Magnetic Resonance* **264** (2016) 131 – 153. Hyperpolarized NMR Comes of Age.

[121] A. Leavesley, I. Kaminker, and S. Han, *Versatile dnp hardware with integrated epr*, *Dynamic Nuclear Polarization Handbook* **ISBN 9781119441649.** (2018).

[122] S. S. Eaton, K. M. More, B. M. Sawant, and G. R. Eaton, *Use of the esr half-field transition to determine the interspin distance and the orientation of the interspin vector in systems with two unpaired electrons*, *Journal of the American Chemical Society* **105** (1983), no. 22 6560–6567.

[123] N. Cox, A. Nalepa, W. Lubitz, and A. Savitsky, *Eldor-detected nmr: A general and robust method for electron-nuclear hyperfine spectroscopy?*, *Journal of Magnetic Resonance* **280** (2017) 63–78.

[124] N. Wili, S. Richert, B. Limburg, S. J. Clarke, H. L. Anderson, C. R. Timmel, and G. Jeschke, *Eldor-detected nmr beyond hyperfine couplings: a case study with cu (ii)-porphyrin dimers*, *Physical Chemistry Chemical Physics* **21** (2019), no. 22 11676–11688.

[125] H. Chen, A. G. Maryasov, O. Y. Rogozhnikova, D. V. Trukhin, V. M. Tormyshev, and M. K. Bowman, *Electron spin dynamics and spin–lattice relaxation of trityl radicals in frozen solutions*, *Physical Chemistry Chemical Physics* **18** (2016), no. 36 24954–24965.

[126] E. Badetti, V. Lloveras, J. L. Munõz Gómez, R. M. Sebastián, A. M. Caminade, J. P. Majoral, J. Veciana, and J. Vidal-Ganced, *Radical dendrimers: A family of five generations of phosphorus dendrimers functionalized with tempo radicals*, *Macromolecules* **47** (2014), no. 22 7717–7724.

[127] M. Lelli, S. R. Chaudhari, D. Gajan, G. Casano, A. J. Rossini, O. Ouari, P. Tordo, A. Lesage, and L. Emsley, *Solid-state dynamic nuclear polarization at 9.4 and 18.8 t from 100 k to room temperature*, *Journal of the American Chemical Society* **137** (2015), no. 46 14558–14561.

[128] S. R. Chaudhari, D. Wisser, A. C. Pinon, P. Berruyer, D. Gajan, P. Tordo, O. Ouari, C. Reiter, F. Engelke, C. Copéret, *et. al.*, *Dynamic nuclear polarization efficiency increased by very fast magic angle spinning*, *Journal of the American Chemical Society* **139** (2017), no. 31 10609–10612.

[129] G. Mathies, M. A. Caporini, V. K. Michaelis, Y. Liu, K.-N. Hu, D. Mance, J. L. Zweier, M. Rosay, M. Baldus, and R. G. Griffin, *Efficient dynamic nuclear polarization at 800 mhz/527 ghz with trityl-nitroxide biradicals*, *Angewandte Chemie International Edition* **54** (2015), no. 40 11770–11774.

[130] G. Stevanato, G. Casano, D. J. Kubicki, Y. Rao, L. Esteban Hofer, G. Menzildjian, H. Karoui, D. Siri, M. Cordova, M. Yulikov, *et. al.*, *Open and closed radicals: Local geometry around unpaired electrons governs mas dnp performance*, *Journal of the American Chemical Society* (2020).

[131] F. Mentink-Vigier, Ü. Akbey, H. Oschkinat, S. Vega, and A. Feintuch, *Theoretical aspects of magic angle spinning-dynamic nuclear polarization*, *Journal of Magnetic Resonance* **258** (2015) 102–120.

[132] K. R. Thurber and R. Tycko, *Theory for cross effect dynamic nuclear polarization under magic-angle spinning in solid state nuclear magnetic resonance: the*

importance of level crossings, *The Journal of Chemical Physics* **137** (2012), no. 8 084508.

[133] A. Karabanov, G. Kwiatkowski, C. U. Perotto, D. Wiśniewski, J. McMaster, I. Lesanovsky, and W. Köckenberger, *Dynamic nuclear polarisation by thermal mixing: quantum theory and macroscopic simulations*, *Physical Chemistry Chemical Physics* **18** (2016), no. 43 30093–30104.

[134] J. Ardenkjaer-Larsen, I. Laursen, I. Leunbach, G. Ehnholm, L.-G. Wistrand, J. Petersson, and K. Golman, *Epr and dnp properties of certain novel single electron contrast agents intended for oximetric imaging*, *Journal of Magnetic Resonance* **133** (1998), no. 1 1–12.

[135] M. Magerstädt, O. A. Gansow, M. W. Brechbiel, D. Colcher, L. Baltzer, R. H. Knop, M. E. Girton, and M. Naegele, *Gd (dota): an alternative to gd (dtpa) as a t1, 2 relaxation agent for nmr imaging or spectroscopy*, *Magnetic Resonance in Medicine* **3** (1986), no. 5 808–812.

[136] A. Equbal, K. A. Tagami, and S. Han, *Pulse shaped dynamic nuclear polarization under magic-angle spinning*, *The Journal of Physical Chemistry Letters* **10** (2019), no. 24 7781–7788.

[137] F. A. Perras and M. Pruski, *Large-scale ab initio simulations of mas dnp enhancements using a monte carlo optimization strategy*, *The Journal of Chemical Physics* **149** (2018), no. 15 154202.

[138] Y. Hovav, A. Feintuch, and S. Vega, *Theoretical aspects of dynamic nuclear polarization in the solid state–the solid effect*, *Journal of Magnetic Resonance* **207** (2010), no. 2 176–189.

[139] A. Abragam, *Overhauser effect in nonmetals*, *Physical Review* **98** (1955), no. 6 1729.

[140] A. E. Dementyev, D. G. Cory, and C. Ramanathan, *High-field overhauser dynamic nuclear polarization in silicon below the metal–insulator transition*, *The Journal of Chemical Physics* **134** (2011), no. 15 154511.

[141] J. Järvinen, D. Zvezdov, J. Ahokas, S. Sheludiakov, L. Lehtonen, S. Vasiliev, L. Vlasenko, Y. Ishikawa, and Y. Fujii, *Dynamic nuclear polarization and esr hole burning in as doped silicon*, *Physical Chemistry Chemical Physics* **22** (2020), no. 18 10227–10237.

[142] H. Hayashi, T. Itahashi, K. M. Itoh, L. S. Vlasenko, and M. P. Vlasenko, *Dynamic nuclear polarization of ^{29}si nuclei in isotopically controlled phosphorus doped silicon*, *Physical Review B* **80** (2009), no. 4 045201.

[143] A. Honig, *Polarization of arsenic nuclei in a silicon semiconductor*, *Physical Review* **96** (1954), no. 1 234.

[144] D. Pines, J. Bardeen, and C. P. Slichter, *Nuclear polarization and impurity-state spin relaxation processes in silicon*, *Physical Review* **106** (1957), no. 3 489.

[145] T. Can, M. Caporini, F. Mentink-Vigier, B. Corzilius, J. Walish, M. Rosay, W. Maas, M. Baldus, S. Vega, T. Swager, *et. al.*, *Overhauser effects in insulating solids*, *The Journal of Chemical Physics* **141** (2014), no. 6 064202.

[146] S. Pylaeva, K. L. Ivanov, M. Baldus, D. Sebastiani, and H. Elgabarty, *Molecular mechanism of overhauser dynamic nuclear polarization in insulating solids*, *The Journal of Physical Chemistry Letters* **8** (2017), no. 10 2137–2142.

[147] X. Ji, T. Can, F. Mentink-Vigier, A. Bornet, J. Milani, B. Vuichoud, M. Caporini, R. G. Griffin, S. Jannin, M. Goldman, *et. al.*, *Overhauser effects in non-conducting solids at 1.2 k*, *Journal of Magnetic Resonance* **286** (2018) 138–142.

[148] W. de Boer, *Dynamic orientation of nuclei at low temperatures*, *Journal of Low Temperature Physics* **22** (1976), no. 1-2 185–212.

[149] S. Mandal and S. T. Sigurdsson, *On the limited stability of bdpa radicals*, *Chemistry–A European Journal* **26** (2020), no. 33 7486–7491.

[150] D. G. Mitchell, R. W. Quine, M. Tseitlin, R. T. Weber, V. Meyer, A. Avery, S. S. Eaton, and G. R. Eaton, *Electron spin relaxation and heterogeneity of the 1: 1 α, γ-bisdiphenylene-β-phenylallyl (bdpa)/benzene complex*, *The Journal of Physical Chemistry B* **115** (2011), no. 24 7986–7990.

[151] C. B. Wilson, D. T. Edwards, J. A. Clayton, S. Han, and M. S. Sherwin, *Dressed rabi oscillation in a crystalline organic radical*, *Physical Review Letters* **124** (2020), no. 4 047201.

[152] A. Equbal, Y. Li, A. Leavesley, S. Huang, S. Rajca, A. Rajca, and S. Han, *Truncated cross effect dynamic nuclear polarization: an overhauser effect doppelganger*, *The Journal of Physical Chemistry Letters* **9** (2018), no. 9 2175–2180.

[153] K. Kundu, A. Feintuch, and S. Vega, *Theoretical aspects of the cross effect enhancement of nuclear polarization under static dynamic nuclear polarization conditions*, *The Journal of Physical Chemistry Letters* **10** (2019), no. 8 1769–1778.

[154] R. Wind, M. Duijvestijn, C. Van Der Lugt, A. Manenschijn, and J. Vriend, *Applications of dynamic nuclear polarization in 13c nmr in solids*, *Progress in Nuclear Magnetic Resonance Spectroscopy* **17** (1985) 33–67.

[155] L. R. Becerra, G. J. Gerfen, R. J. Temkin, D. J. Singel, and R. G. Griffin, *Dynamic nuclear polarization with a cyclotron resonance maser at 5 t*, *Physical Review Letters* **71** (1993), no. 21 3561.

[156] A. Radaelli, H. A. Yoshihara, H. Nonaka, S. Sando, J. H. Ardenkjaer-Larsen, R. Gruetter, and A. Capozzi, *13c dynamic nuclear polarization using sa-bdpa at 6.7 t and 1.1 k: Coexistence of pure thermal mixing and well-resolved solid effect*, *The Journal of Physical Chemistry Letters* **11** (2020) 6873–6879.

[157] V. Meyer, S. S. Eaton, and G. R. Eaton, *X-band electron spin relaxation times for four aromatic radicals in fluid solution and comparison with other organic radicals*, *Applied Magnetic Resonance* **45** (2014), no. 10 993–1007.

[158] K. Hashi, S. Ohki, S. Matsumoto, G. Nishijima, A. Goto, K. Deguchi, K. Yamada, T. Noguchi, S. Sakai, M. Takahashi, *et. al.*, *Achievement of 1020 mhz nmr*, *Journal of Magnetic Resonance* **256** (2015) 30–33.

[159] M. Callon, A. A. Malär, S. Pfister, V. Římal, M. E. Weber, T. Wiegand, J. Zehnder, M. Chávez, R. Cadalbert, R. Deb, *et. al.*, *Biomolecular solid-state nmr spectroscopy at 1200 mhz: the gain in resolution*, *Journal of Biomolecular NMR* (2021) 1–18.

[160] D. A. Hall, D. C. Maus, G. J. Gerfen, S. J. Inati, L. R. Becerra, F. W. Dahlquist, and R. G. Griffin, *Polarization-enhanced nmr spectroscopy of biomolecules in frozen solution*, *Science* **276** (1997), no. 5314 930–932.

[161] Y. Matsuki, T. Sugishita, and T. Fujiwara, *Surface-only spectroscopy for diffusion-limited systems using ultra-low-temperature dnp mas nmr at 16.4 t*, *The Journal of Physical Chemistry C* **124** (2020), no. 34 18609–18614.

[162] K. R. Thurber, W.-M. Yau, and R. Tycko, *Low-temperature dynamic nuclear polarization at 9.4 t with a 30 mw microwave source*, *Journal of Magnetic Resonance* **204** (2010), no. 2 303–313.

[163] F. J. Scott, N. Alaniva, N. C. Golota, E. L. Sesti, E. P. Saliba, L. E. Price, B. J. Albert, P. Chen, R. D. O'Connor, and A. B. Barnes, *A versatile custom cryostat for dynamic nuclear polarization supports multiple cryogenic magic angle spinning transmission line probes*, *Journal of Magnetic Resonance* **297** (2018) 23–32.

[164] D. Lee, E. Bouleau, P. Saint-Bonnet, S. Hediger, and G. De Paëpe, *Ultra-low temperature mas-dnp*, *Journal of Magnetic Resonance* **264** (2016) 116–124.

[165] Q. Z. Ni, E. Markhasin, T. V. Can, B. Corzilius, K. O. Tan, A. B. Barnes, E. Daviso, Y. Su, J. Herzfeld, and R. G. Griffin, *Peptide and protein dynamics and low-temperature/dnp magic angle spinning nmr*, *The Journal of Physical Chemistry B* **121** (2017), no. 19 4997–5006.

[166] A. N. Smith, K. Märker, T. Piretra, J. C. Boatz, I. Matlahov, R. Kodali, S. Hediger, P. C. van der Wel, and G. De Paëpe, *Structural fingerprinting of protein aggregates by dynamic nuclear polarization-enhanced solid-state nmr at natural isotopic abundance*, *Journal of the American Chemical Society* **140** (2018), no. 44 14576–14580.

[167] A. N. Smith, M. A. Caporini, G. E. Fanucci, and J. R. Long, *A method for dynamic nuclear polarization enhancement of membrane proteins*, *Angew. Chem.* **127** (2015), no. 5 1562–1566.

[168] V. Macho, R. Kendrick, and C. Yannoni, *Cross polarization magic-angle spinning nmr at cryogenic temperatures*, *Journal of Magnetic Resonance (1969)* **52** (1983), no. 3 450–456.

[169] A. Hackmann, H. Seidel, R. Kendrick, P. Myhre, and C. Yannoni, *Magic-angle spinning nmr at near-liquid-helium temperatures*, *Journal of Magnetic Resonance (1969)* **79** (1988), no. 1 148–153.

[170] A. Samoson, T. Tuherm, J. Past, A. Reinhold, T. Anupõld, and I. Heinmaa, *New horizons for magic-angle spinning nmr*, *New Techniques in Solid-State NMR* (2005) 15–31.

[171] M. Concistrè, O. G. Johannessen, E. Carignani, M. Geppi, and M. H. Levitt, *Magic-angle spinning nmr of cold samples*, *Accounts of chemical research* **46** (2013), no. 9 1914–1922.

[172] E. Bouleau, P. Saint-Bonnet, F. Mentink-Vigier, H. Takahashi, J.-F. Jacquot, M. Bardet, F. Aussenac, A. Purea, F. Engelke, S. Hediger, *et. al.*, *Pushing nmr sensitivity limits using dynamic nuclear polarization with closed-loop cryogenic helium sample spinning*, *Chemical science* **6** (2015), no. 12 6806–6812.

[173] Y. Matsuki, S. Nakamura, S. Fukui, H. Suematsu, and T. Fujiwara, *Closed-cycle cold helium magic-angle spinning for sensitivity-enhanced multi-dimensional solid-state nmr*, *Journal of Magnetic Resonance* **259** (2015) 76–81.

[174] S. Krämer and M. Mehring, *Low-temperature charge ordering in the superconducting state of* $yba_2cu_3o_{7\delta}$, *Physical review letters* **83** (1999), no. 2 396.

[175] S. Clough and J. Hill, *Temperature dependence of methyl group tunnelling rotation frequency*, *Journal of Physics C: Solid State Physics* **7** (1974), no. 1 L20.

[176] K. R. Thurber and R. Tycko, *Measurement of sample temperatures under magic-angle spinning from the chemical shift and spin-lattice relaxation rate of 79br in kbr powder*, *Journal of magnetic resonance* **196** (2009), no. 1 84–87.

[177] Y. Endo, T. Fujiwara, Y. Matruki, S. Nakamura, and T. Nemoto, *Nmr sample tube*, U.S. Patent US10914799B2, Feb. 2021.

[178] Y. Endo, T. Fujiwara, Y. Matruki, S. Nakamura, and T. Nemoto, *Nmr sample tube*, Japanese Patent JP6750819B2, Sep. 2020.

[179] J. Van Houten, W. T. Wenckebach, and N. Poulis, *Proton spin-lattice relaxation in deuterated diluted copper tutton salts*, *Physica B+ C* **92** (1977), no. 2 201–209.

[180] S. J. Ullrich, S. Hölper, and C. Glaubitz, *Paramagnetic doping of a 7tm membrane protein in lipid bilayers by gd^{3+}-complexes for solid-state nmr spectroscopy*, *Journal of biomolecular NMR* **58** (2014), no. 1 27–35.

[181] A. Equbal, K. Tagami, and S. Han, *Balancing dipolar and exchange coupling in biradicals to maximize cross effect dynamic nuclear polarization*, *Physical Chemistry Chemical Physics* **22** (2020), no. 24 13569–13579.

[182] B. Falcon, W. Zhang, M. Schweighauser, A. G. Murzin, R. Vidal, H. J. Garringer, B. Ghetti, S. H. Scheres, and M. Goedert, *Tau filaments from multiple cases of sporadic and inherited alzheimer's disease adopt a common fold*, *Acta neuropathologica* **136** (2018), no. 5 699–708.

[183] S. H. Scheres, W. Zhang, B. Falcon, and M. Goedert, *Cryo-em structures of tau filaments*, *Current Opinion in Structural Biology* **64** (2020) 17–25.

[184] A. J. Dregni, V. S. Mandala, H. Wu, M. R. Elkins, H. K. Wang, I. Hung, W. F. DeGrado, and M. Hong, *In vitro 0n4r tau fibrils contain a monomorphic β-sheet core enclosed by dynamically heterogeneous fuzzy coat segments*, *Proceedings of the National Academy of Sciences* **116** (2019), no. 33 16357–16366.

[185] A. Potapov, W.-M. Yau, R. Ghirlando, K. R. Thurber, and R. Tycko, *Successive stages of amyloid-β self-assembly characterized by solid-state nuclear magnetic resonance with dynamic nuclear polarization*, *Journal of the American Chemical Society* **137** (2015), no. 25 8294–8307.

[186] C.-T. Han, J. Song, T. Chan, C. Pruett, and S. Han, *Electrostatic environment of proteorhodopsin affects the pka of its buried primary proton acceptor*, *Biophysical journal* **118** (2020), no. 8 1838–1849.

[187] B. D. Armstrong, D. T. Edwards, R. J. Wylde, S. A. Walker, and S. Han, *A 200 ghz dynamic nuclear polarization spectrometer*, *Physical Chemistry Chemical Physics* **12** (2010), no. 22 5920–5926.

[188] K. R. Thurber, A. Potapov, W.-M. Yau, and R. Tycko, *Solid state nuclear magnetic resonance with magic-angle spinning and dynamic nuclear polarization below 25 k*, *J. Magn. Reson.* **226** (2013) 100–106.

[189] K. Thurber and R. Tycko, *Low-temperature dynamic nuclear polarization with helium-cooled samples and nitrogen-driven magic-angle spinning*, *J. Magn. Reson.* **264** (2016) 99–106.

[190] "Pd miditrap g-10." `https://cdn.cytivalifesciences.com/dmm3bwsv3/AssetStream.aspx?mediaformatid=10061&destinationid=10016&assetid=13372`. Accessed: 2021-08-11.